NASS
NAN YANG ACADEMY OF SCIENCES

SUSTAINABLE MARINE STRUCTURES

Volume 5·Issue 2·September 2023 ISSN 2661-3158(Online)

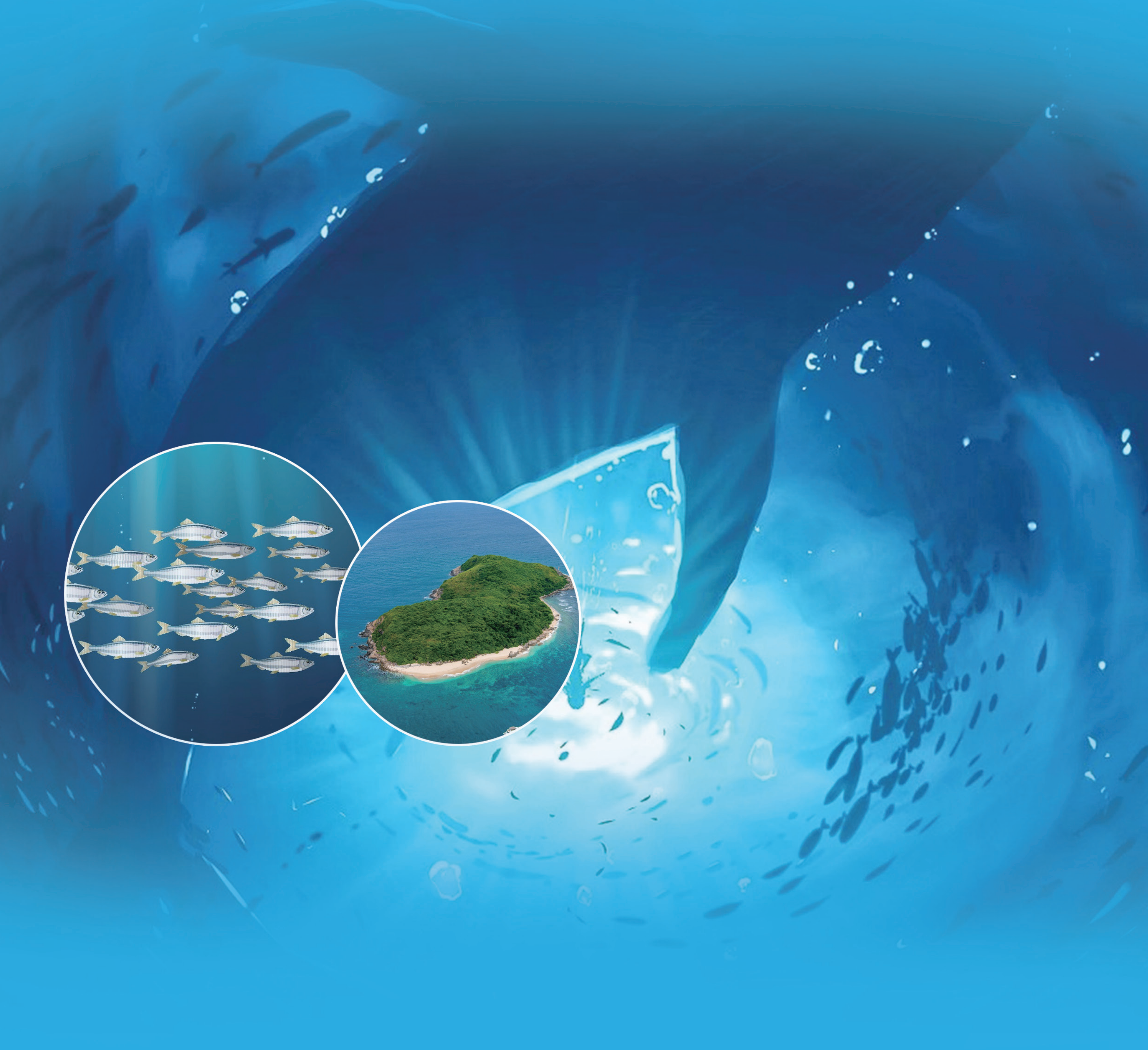

NASS
NAN YANG ACADEMY OF SCIENCES

Editorial Board

Editor-in-Chief

Associate Editors

Editorial Board Member

ISSN: 2661-3158 (Online)
Volume 5 Issue 2 September 2023

SUSTAINABLE MARINE STRUCTURES

NASS
NAN YANG ACADEMY OF SCIENCES

NASS
NAN YANG ACADEMY OF SCIENCES

Volume 5 | Issue 2 | September 2023 | Page 1-54
Sustainable Marine Structures

Contents

Editorial

Articles

Sustainable Marine Structures
https://journals.nasspublishing.com/index.php/sms

ARTICLE

Enhancing Friction Stir Welding in Fishing Boat Construction through Deep Learning-Based Optimization

Erfan Maleki[1] **Okan Unal**[2,3] **Seyed Mahmoud Seyedi Sahebari**[4] **Kazem Reza Kashyzadeh**[5*] **Nima Amiri**[6]

1. Mechanical Engineering Department, Politecnico di Milano, Milan, 20156, Italy
2. Mechanical Engineering Department, Karabuk University, Karabuk, 78050, Turkey
3. Modern Surface Engineering Laboratory, Karabuk University, Karabuk, 78050, Turkey
4. Department of Mechanical and Manufacturing Engineering, Ontario Tech University, L1G 0C5ON, Oshawa, Canada
5. Department of Transport, Academy of Engineering, RUDN University, 6 Miklukho-Maklaya Street, Moscow, 117198, Russian Federation
6. Paul M. Rady Department of Mechanical Engineering, University of Colorado, Boulder, CO, 80309, United States

ARTICLE INFO

Article history
Received: 17 June 2023
Revised: 10 August 2023
Accepted: 18 August 2023
Published Online: 19 August 2023

Keywords:
Simulation and modelling
Welding
Friction stir welding
Deep neural network
Optimization

ABSTRACT

In the present study, the authors have attempted to present a novel approach for the prediction, analysis, and optimization of the Friction Stir Welding (FSW) process based on the Deep Neural Network (DNN) model. To obtain the DNN structure with high accuracy, the most focus has been on the number of hidden layers and the activation functions. The DNN was developed by a small database containing results of tensile and hardness tests of welded 7075-T6 aluminum alloy. This material and the production method were selected based on the application in the construction of fishing boat flooring, because on the one hand, it faces the corrosion caused by proximity to sea water and on the other hand, due to direct contact with human food, i.e., fish etc., antibacterial issues should be considered. All the major parameters of the FSW process, including axial force, rotational speed, and traverse speed as well as tool diameter and tool hardness, were considered to investigate their correspondence effects on the tensile strength and hardness of welded zone. The most important achievement of this research showed that by using SAE for pre-training of neural networks, higher accuracy can be obtained in predicting responses. Finally, the optimal values for various welding parameters were reported as rotational speed: 1600 rpm, traverse speed: 65 mm/min, axial force: 8 KN, shoulder and pin diameters: 15.5 and 5.75 mm, and tool hardness: 50 HRC.

---

*Corresponding Author:
Kazem Reza Kashyzadeh,
Department of Transport, Academy of Engineering, RUDN University, 6 Miklukho-Maklaya Street, Moscow, 117198, Russian Federation;
Email: kazem.kashyzadeh@gmail.com

DOI: http://dx.doi.org/10.36956/sms.v5i2.875

1. Introduction

One of the oldest methods of non-separable connections, which is widely used in various industries, is welding. In fact, large structures cannot be produced in one piece, such as the body of ships, airplanes, trains, subways, and ground vehicles [1, 2]. Therefore, it is necessary to connect different parts to each other and create an assembly. Hence, depending on the application of the connection, different types of welding are used in various industries, each of which has advantages and disadvantages compared to the others [3]. For example, the biggest challenge for all types of welding methods is the creation of tensile residual stress in the welding area [4] or microstructure change in the Heat-Affected Zone (HAZ), both of which lead to a decrease in joint strength [5,6]. In other words, these two areas are prone to damage and cracks. However, some additional disadvantages arise when an intermediate material is used for welding. Therefore, in large industries, it is usually tried to use welding methods that do not require an electrode or additional material, such as Resistance Spot Welding (RSW) in the automotive industry [7]. Moreover, the FSW process which was first presented by The Welding Institute (TWI) in 1991 [8], has emerged as an effective alternative to traditional Metal Inert Gas (MIG) welding for use in marine applications, particularly as the industry moves towards increased use of aluminum alloys. Based on the TWI report in 2007, 171 large organizations and companies received licenses to manufacture shipbuilding from aluminum extrusion by FSW process, especially, Al7075 is used to manufacture aluminum panels for deep freezing of fishing boats. In this regard, one of the biggest challenges and concerns in the manufacturing is to optimize the strength of welded joints via the welding process. The powerful combination of reduced weight from aluminum and increased strength of FSW welds can yield spectacular benefits for marine designs. Generally, FSW is well suited for marine applications because of the nature of the welds [9]. During the last decades, the selection of the favorable parameters of this process to obtain the optimal properties of the welded parts is remained challenging and widely considered by many researchers. In this regard, the goal is to increase the quality and improve the strength of the connection, and for this purpose, various techniques have been used. The number of publications in this field is very large and a comprehensive study is required for a detailed review, which is beyond the scope of the present research. However, some of the efforts made to optimize aluminum parts welded in this way are collected in Table 1.

As presented in Table 1, scientists paid the most attention to data mining methods such as Taguchi Method (TM), Linear Regression Method (LRM), Analysis of Variance (ANOVA), and Response Surface Method (RSM) to optimize different parameters of FSW process. In addition, the main goal was to improve the tensile strength and hardness of the connection. In recent years, attention has been paid to machine learning methods such as Artificial Intelligence (AI) for modeling and optimizing friction stir welding of aluminum alloys. Nevertheless, the present article includes the most comprehensive laboratory results and six input parameters. Also, the deep machine learning method was used to provide a new approach in optimizing the friction stir welding process of aluminum parts. Recently, the advantages and accuracy of using Deep Neural Network (DNN) technique compared to Artificial Neural Network (ANN) have been evident and proven in various fields of engineering [28,29]. Padhy et al. have published a comprehensive review on the FSW technology and the effects of process parameters on the material characterization and metallurgical properties like microstructure [30]. In addition, Gangwar and Ramulu have focused on the titanium alloys joints by FSW [31]. Also, to improve the quality of this type of welded joint, the effects of two parameters of the tool and the thickness of the raw material sheets have been evaluated. After that, microstructure, material properties (i.e., hardness), mechanical properties (i.e., tensile, fatigue, and fracture toughness), residual stress field, and temperature distribution have been studied. Mohanty et al. have utilized RSM to examine the effects of tool shoulder and probe profile geometries simultaneously on the FSW of aluminum sheets [32]. In this research, three parameters of tool type, tool probe diameter, and shoulder flat surface, each of them at three different levels, were considered as input to the RSM analysis. Also, connection strength, weld cross section area, and grain size in both welded area and HAZ were considered as output. The results showed that straight cylindrical FSW tool with the minimum level of probe diameter provided better strength of welded joint. Ahmed et al. have optimized FSW process parameters to achieve the maximum tensile strength and hardness of welded 5451Al sheets by performing Taguchi sensitivity analysis [33]. They stated that the pin profile of the tool is the most effective factor in both outputs with more than 60% effectiveness. Moreover, research on the connection of thick aluminum plates through FSW has also been carried out [34]. Before this, in most articles, the connection of thin sheets up to 5 or 6 mm has been considered. In this regard, Kumar et al. have proposed a trapezoidal pin of tool to reach a free-defect connection of 12 mm thick aluminum sheets. constructions, which are ultimately directly or indirectly related to the economic field and cost. For example, in the construction of a fishing boat, it is possible to refer to the initial costs including the preparation of the raw material i.e., aluminum alloy, the construction design including the dimensions and thicknesses of the sheets for the construction of the ship, and finally the construction method and the type of connection of the sheets to each other. On the other hand, considering the working conditions in the vicinity of sea water and the corrosion as a result, and on the other hand, in direct connection with fish and antibacterial issues, it is necessary to choose the type of alloy and heat treatment correctly. Finally, in order to reduce production time and ultimately reduce the cost of free-defect production, in order to minimize repairs, it is necessary to optimize the production process. Apart from these cases, just the free-defect construction is not enough, and it must have enough strength so that it does not have problems after some time of use [35]. For this purpose, in addition to examining the tensile strength, it is better to study the hardness and microstructure in the welded area. Therefore, the results of such research can satisfy part of the demands stated above.

Table 1. A summary of the research conducted to optimize the friction stir welding of aluminum parts.

Reference	Year	Material	Method	Parameters	Objective
[10]	2015	AA6082-T6	Taguchi	Joint geometries: butt, lap, and T-shaped	Ultimate tensile strength
[11]	2010	AA1050	Grey relation analysis and Taguchi	Rotating speed, welding speed, and shoulder diameter	Tensile strength and elongation
[12]	2015	AA8011	Taguchi-Based Grey Relational Analysis	Tool shoulder diameter, rotational speed, welding speed, and axial load	Tensile strength and microhardness
[13]	2016	Cast AA7075/SiCp Composite	Response surface methodology, regression model, and Fuzzy grey relational analysis approach	Spindle speed, travelling speed, downward force, and percentage of SiC added to AA7075	Ultimate tensile strength and percentage elongation
[14]	2019	AA6082/SiC/10P composite	Taguchi approach and analysis of variance (ANOVA)	Tool rotation speed, welding speed, and tool tilt angle	Ultimate tensile strength
[15]	2018	Dissimilar alloys (AA6082/AA5083)	Taguchi method, Grey relational method, weight method, and analysis of variance (ANOVA)	Tool rotation speed, welding speed, tool pin profile, and shoulder diameter	Ultimate tensile strength and elongation
[16]	2008	RDE-40 aluminium alloy	Taguchi technique and analysis of variance (ANOVA)	Rotational speed, traverse speed, and axial force	Tensile strength
[17]	2010	AA7075-T6	Response surface methodology and analysis of variance (ANOVA)	Tool rotational speed, welding speed, axial force, tool shoulder diameter, pin diameter, and tool hardness	Tensile strength
[18]	2017	Al5052-H32 alloy	Response surface methodology	Tool profile, rotational speed, welding speed, and tool tilt angle	Tensile strength and elongation
[19]	2012	Dissimilar alloy: AA6061-T6 and AA7075-T6	Response surface methodology	Rotational speed, welding speed, and axial force	Ultimate tensile strength, yield strength, and displacement
[20]	2009	Cast aluminum alloy A319	Taguchi method and analysis of variance (ANOVA)	Tool rotation speed, welding speed, and axial force	Tensile strength
[21]	2021	Dissimilar aluminum alloys 6061 and 5083	Response surface methodology	Tool pin profile, tool rotation speed, feed rate, and tool tilt angle	Ultimate tensile strength, yield strength, and microhardness
[22]	2021	Dissimilar AA7075-T651 and AA6061	Taguchi technique and analysis of variance (ANOVA)	Tool offset, pin profile of tool, and tilt angle of tool	Tensile strength
[23]	2022	Armor-grade aluminum alloys AA5083	Response surface methodology, regression, and analysis of variance (ANOVA)	Shoulder diameter, shoulder flatness, pin profile, and welding speed	Ultimate and yield tensile strength and elongation

Table 1 continued

Reference	Year	Material	Method	Parameters	Objective
[24]	2021	Dissimilar aluminum alloys of AA 7075-O and AA 5052-O grade	Taguchi approach and analysis of variance (ANOVA)	Tool pin profile, tool rotational speed, feed rate, and tool offset	Tensile strength and microhardness
[25]	2018	Dissimilar AA5083-O and AA6063-T6 aluminum alloys	Artificial intelligence and genetic algorithm	Tool rotational speed, welding speed, shoulder diameter, and pin diameter	Tensile strength, microhardness, and grain size
[26]	2021	Dissimilar AA3103 and AA7075 aluminum alloys	Taguchi method	Tool rotation speed, feed rate, and tool pin profile	Hardness, tensile strength, and impact strength
[27]	2018	Armor-marine grade AA7039	Desirability approach: RSM & ANOVA	Rotational speed, feed rate, and tilt angle	Ultimate tensile strength and tensile elongation

In the FSW, a tool moves along the joint line of two plates (similar or dissimilar) that simultaneously rotates and therefore it creates frictional heat that mechanically intermixes the metals and forges the hot and softened metal by the applied axial force. Figure 1 depicts the schematic of the FSW process and its effective parameters such as axial force, rotational and traverse speeds as well as tool geometry and hardness. As mentioned, in the FSW both mechanical and thermal processes are involved which show their effects in the welding zone and its surrounding regions and divide it into four major parts of Weld Nugget (WN), Thermo-Mechanically Affected Zone (TMAZ), Heat Affected Zone (HAZ), and Base Material (BM) that can be described as fully recrystallized region, area that plastically deformed without recrystallization, thermal affected, and region of original properties, respectively [36]. Because of the variety of physical phenomena in the FSW process, its analysis and optimization have become very complicated. Therefore, scholars have tried to solve the problems in this field by considering different alternative approaches of experiments like modeling and optimization methods [37]. In this regard, chu et al. have performed mechanical and microstructural optimization in the FSW joint of Al-Li alloy [38]. They used RSM and Box-Behnken experimental design to maximize static strength (i.e., tensile and shear stresses). Moreover, Electron Backscattering Diffraction (EBSD) and Differential Scanning Calorimetry (DSC) observations have been utilized to optimize hardness and reach the ultrafine grains. Sreenivasan et al. have optimized FSW process parameters for joining composite materials (i.e., AA7075 - SiC) [39]. They considered different parameters, including friction pressure, spindle speed, burn-off length, and upset pressure, in three levels, as the input variables in the optimization algorithms. Also, they tried to optimize hardness and Ultimate Tensile Strength (UTS). To achieve this goal, they employed two methods of linear regression and genetic algorithm. In a similar study, FSW process parameters have been optimized to obtain the maximum joint strength and the highest elongation [40]. Also, Heidarzadeh et al. have employed ANOVA and RSM analysis to present mathematical relationships between the strength, elongation, and hardness of the connection in terms of FSW process parameters, including rotation speed, traverse speed, and axial force. They stated that the hardness reduces by raising the rotation speed and axial force and decreasing the traverse speed at the same time. Moreover, rotation speed and axial force are the most important factors that affect the strength and elongation values, respectively. After that, Heidarzadeh continued his research in this field with a focus on material properties and imaging observations, including EBSD and TEM [41]. He et al. have published a review report on the numerical simulation of FSW process [42]. They discussed different techniques for process simulation and presented the results obtained from them. However, methods based on artificial intelligence such as neural networks are remarkably applied in different aspects of science and engineering [43-46] as well as their application for modeling of FSW process [47-49]. In general, a neural network has three major layers of input, hidden, and output [50,51]. A literature review conducted in this research shows that shallow Neural Network (SNN), as the primary generation of artificial neural networks, has been mostly used in the simulation of FSW. In fact, SNNs have 1 or 2 hidden layers which are generally trained by Back-Propagation (BP) algorithm [46]. These networks besides their beneficial applications have some limitations. The most important limitation of SNNs is that a large number of data sets are required for their development. Recently, by considering the improvements achieved in the training of neural networks by deep learning presented by Hinton et al. [52]; it is feasible to develop deep neural network with higher efficiency by employing small data set [53]. As an innovation, the current paper aims to show the capability of the DNN for prediction, analysis, and optimization of the FSW process for the first time by using small data set. In the following, the authors have attempted to assess strength and hardness in the welded zone in terms of different process parameters as well as pin and shoulder features (i.e., hardness and diameter).

2. Experimental Data

The data used in this research were extracted from the paper published by Rajakumar et al. [54]. In order to conduct experiments, they prepared rolled sheets of 7075-T6 aluminum alloy with a thickness of 5 mm and dimensions of 150 × 300 mm. The ultimate and yield tensile strengths of the sheets are 485 and 410 MPa, respectively. Table 2 also presents the chemical composition of this material. Next, friction stir welding operation perpendicular to the rolling was performed as a single pulse and with non-consumable tools. The details of this process are shown in Figure 2.

In the next step, tensile test samples were fabricated according to the ASTM standard. They prepared two types of smooth and notched samples. All tests were performed at room temperature and at a speed of 0.5 mm/min. However, in the present study, only the laboratory results for smooth samples were used. Moreover, Vickers microhardness in the welded zone was measured by applying a force of 50 gr.

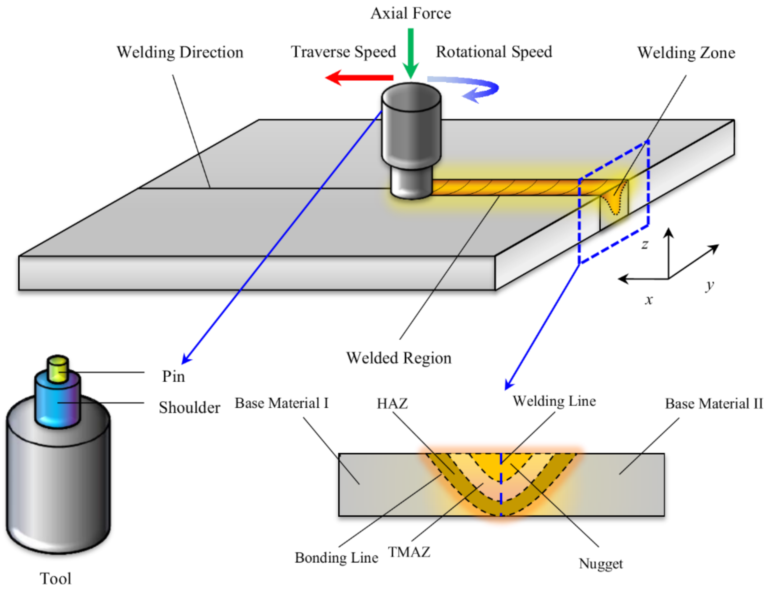

Figure 1. Schematic illustration of the FSW process and parameters affecting welded joint quality.

Table 2. Chemical composition of prepared sheets.

Element	**Mg**	**Mn**	**Zn**	**Fe**	**Cu**	**Si**	**Al**
Value (%)	2.10	0.12	5.10	0.35	1.2	0.58	90.55

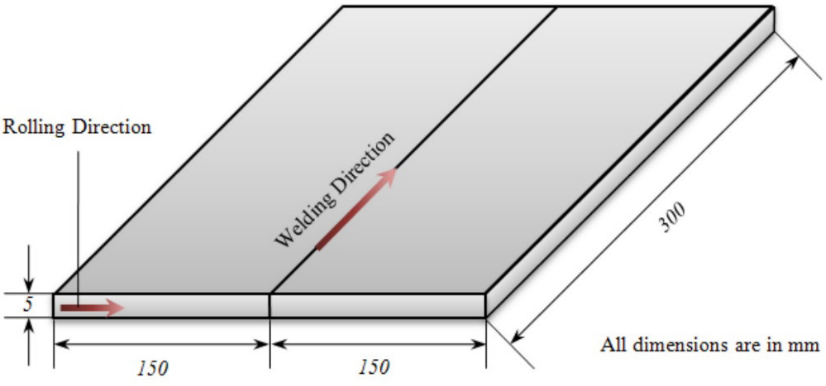

Figure 2. Dimensional details of sheets, sheets rolling and welding process directions.

3. DNN Developing

A DNN with four hidden layers was developed to model the FSW process by using experimental data described in the previous section. This experimental dataset was selected because it includes high amounts of effective parameters of FSW process. Nevertheless, the data used for this simulation is given in the Appendix (Table A1). Also, the first author has used these data previously for providing a model based on the common SNN with BP method [48]. Hence, the innovation of the present work with the previous one is to present a novel modified neural network based on deep learning. Parameters of axial force, rotational and traverse speeds as well as shoulder and pin diameters, and tool hardness were considered to investigate their related influences on the strength and used for the training and testing steps, respectively. In addition, in order to develop DNN, as the dataset is small, a Stacked Auto-Encoder (SAE) was used for pre-training of DNN. SAE is a specific hidden layer SNN that has the same input and output layers and also has the same number of neurons in each layer of it with respect to the main DNN architecture. Used DNN along with linking to SAE is presented in Figure 3. Also, the accuracy of predicted results was determined via correlation coefficient (R2). The obtained accuracies for the developed DNN with and without SAE for both training and testing steps based on equation (1) are reported in Table 3.

$$R = \frac{\sum_{i=1}^{n}(f_{EXP,i}-\bar{F}_{EXP})(f_{DNN,i}-\bar{F}_{DNN})}{\sqrt{\sum_{i=1}^{n}\left((f_{EXP,i}-\bar{F}_{EXP})^2(f_{DNN,i}-\bar{F}_{DNN})^2\right)}} \tag{1}$$

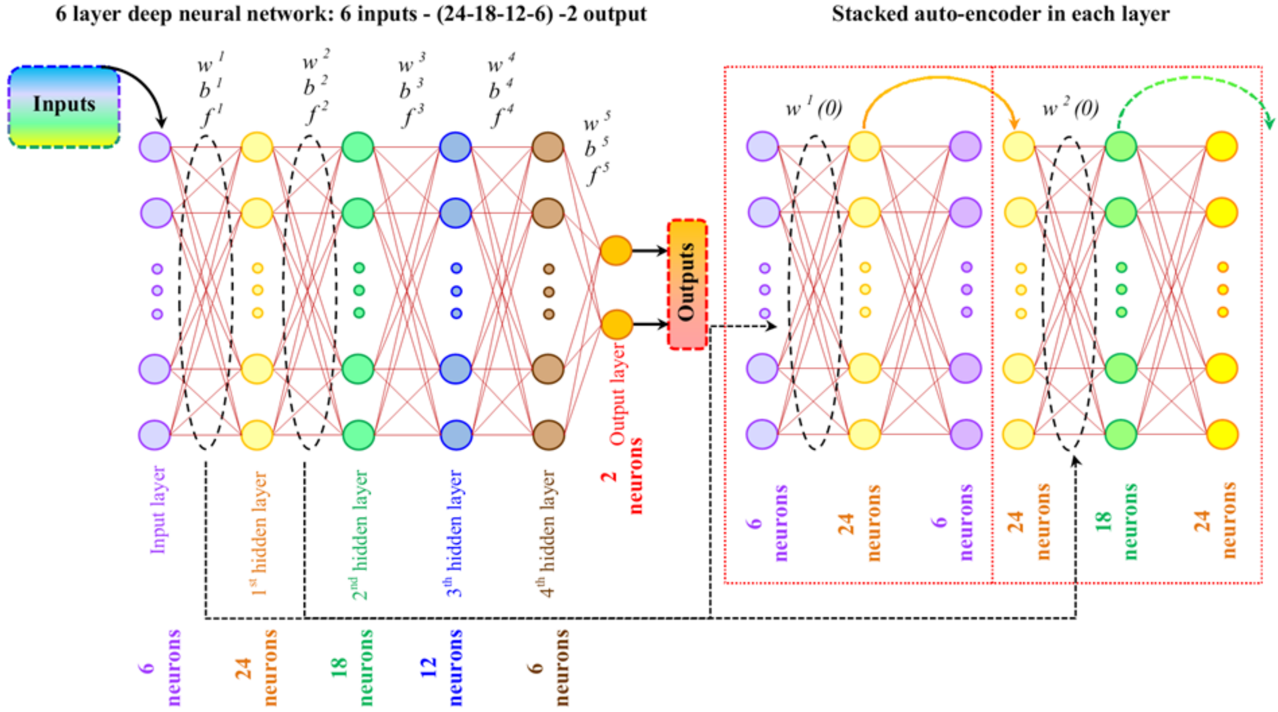

Figure 3. Used DNN along with linking to SAE.

Table 3. Obtained values of accuracies for developed DNN.

Developed DNN	Accuracy
Without SAE-train	0.982
Without SAE-test	0.974
With SAE-train	0.996
With SAE-test	0.993

4. Results and Discussions

Based on the results of the determination of accuracies that show the DNN was developed well, parametric analysis was performed. In Figure 4 and Figure 5, the effects of welding process parameters and tool features on the welded zone strength and hardness are continuously revealed respectively in a general condition and interval of each parameter for the applied analyses are shown at the bottom of each contour. The region that has ≤ 95% of the considered experimental value was specified in each 2D contour by a black line. It can be seen that, in the same graph whole prediction, analysis, and optimization can be carried out with accuracy close to 100% ($R^2 \approx 1$). From Figure 4, as the rotation speed increases, the strength of the welded zone always increases, which is consistent with the results of Ahmed et al. in the study of 2022 [33]. Also, with the increase of the axial force, the strength improves, but its changes are not significant compared to the rotational speed parameter and it depends on the values of other parameters. Ref No. 33 also deals with the optimization of process parameters. The authors showed that the tensile strength of FSW joint considering the feed rate of 18 mm/min is much higher than the tensile strength of FSW joint with feed rates of 16 and 20 mm/min. In other words, the tensile strength of the connection increases with the increase of the feed rate in the range of 16 to 18 mm/min, and it decreases with the increase of the feed rate in the range of 18 to 20 mm/min. Therefore, this interpretation is exactly in accordance with the results presented in Figure 4. Moreover, the contour presented in Figure 4b indicates that if the rotational speed is less than 1000 rpm, changes in axial force do not affect the strength. However, all the results presented in this section are considering the welding conditions in this study and different results may be obtained in other conditions. Therefore, more studies are needed to generalize the results to other conditions, which is on the agenda of this research group for its future studies. Furthermore, by focusing on the hardness in the welded zone as a response, it is seen that the hardness increases with increasing rotational speed. But in interaction with other parameters, i.e., axial force and transverse speed, there is an intermediate area where the highest hardness is obtained within this specific area and the lowest hardness is obtained outside this area. For example, it is clear from Figure 4f that setting the rotational speed in the range of 1500 to 1700 rpm and also the axial force between 7 and 9 KN can result in the highest hardness in the welded zone.

As shown in Figure 5, no specific trends can be found between the system responses (i.e., strength and hardness in the welded zone) and tool characteristics, including pin and shoulder diameters and their hardness. In other words, the interaction between various parameters of this section must be checked with more precision and laboratory data and it is very difficult and perhaps unlikely to be able to independently declare the effect of one of these parameters on the output, because depending on the conditions of other parameters, there is a possibility of changing the state of the response. It is clearly evident in the contours with yellow color theme (i.e., Figure 5d, e, and f) that there are different circular and elliptical layers, therefore, there is a specific area in each contour that should be tried to select the characteristics of the tool in such a way that the responses be placed within these areas.

In summary, according to all the achievements presented above, in order to obtain the optimal parameters, all the contours should be placed on each other at the same time and the common space between the areas marked by black lines should be selected. In this way, optimal values of rotational speed, traverse speed, axial force, shoulder diameter, pin diameter, and tool hardness are specified as 1600 rpm, 65 mm/min, 8 KN, 15.5 mm, 5.75 mm, and 50 HRC, respectively.

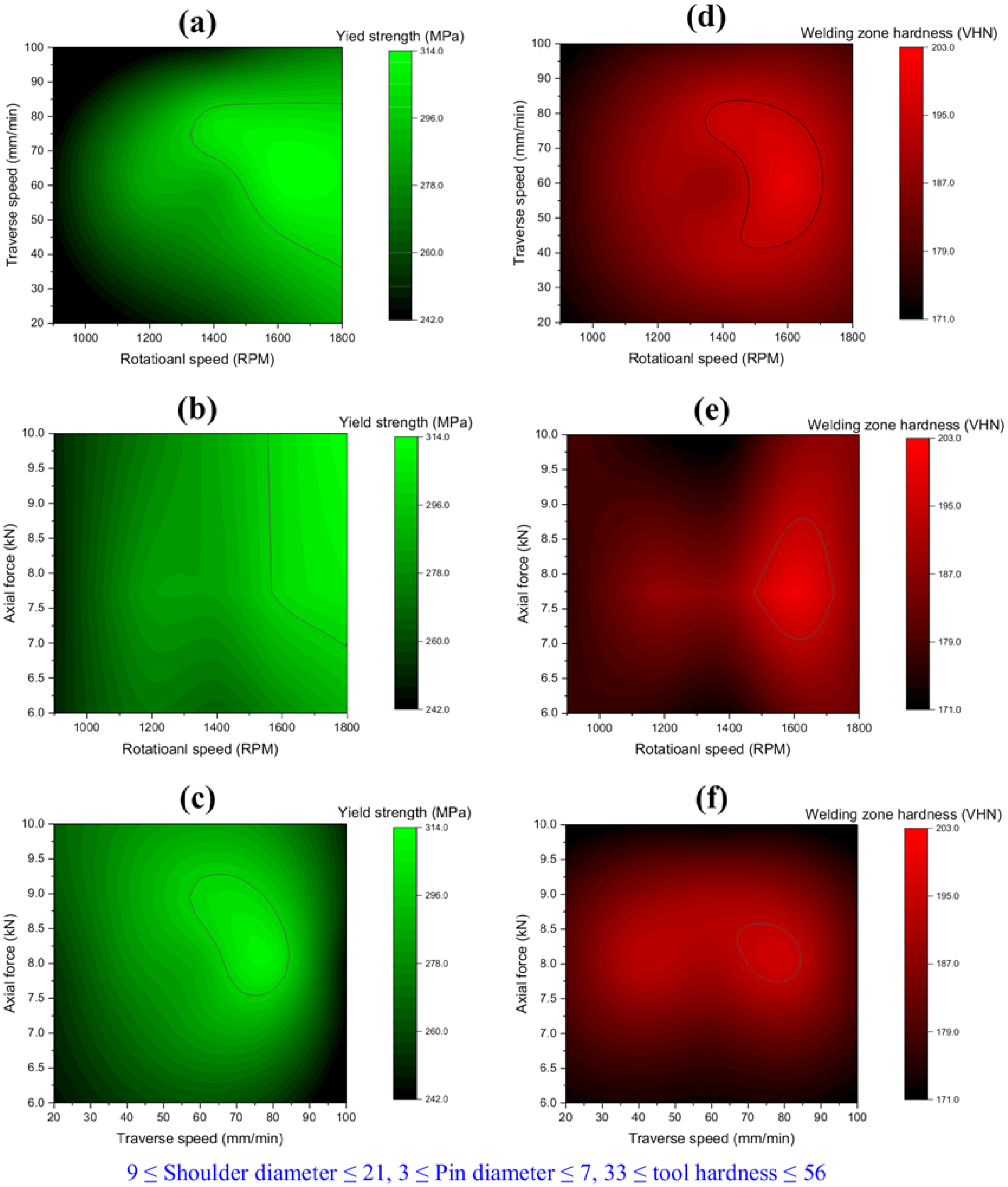

Figure 4. Parametric analysis of the effects of axial force, rotational and traverse speeds on strength (**a-c**) and hardness (**d-f**) of welded zone.

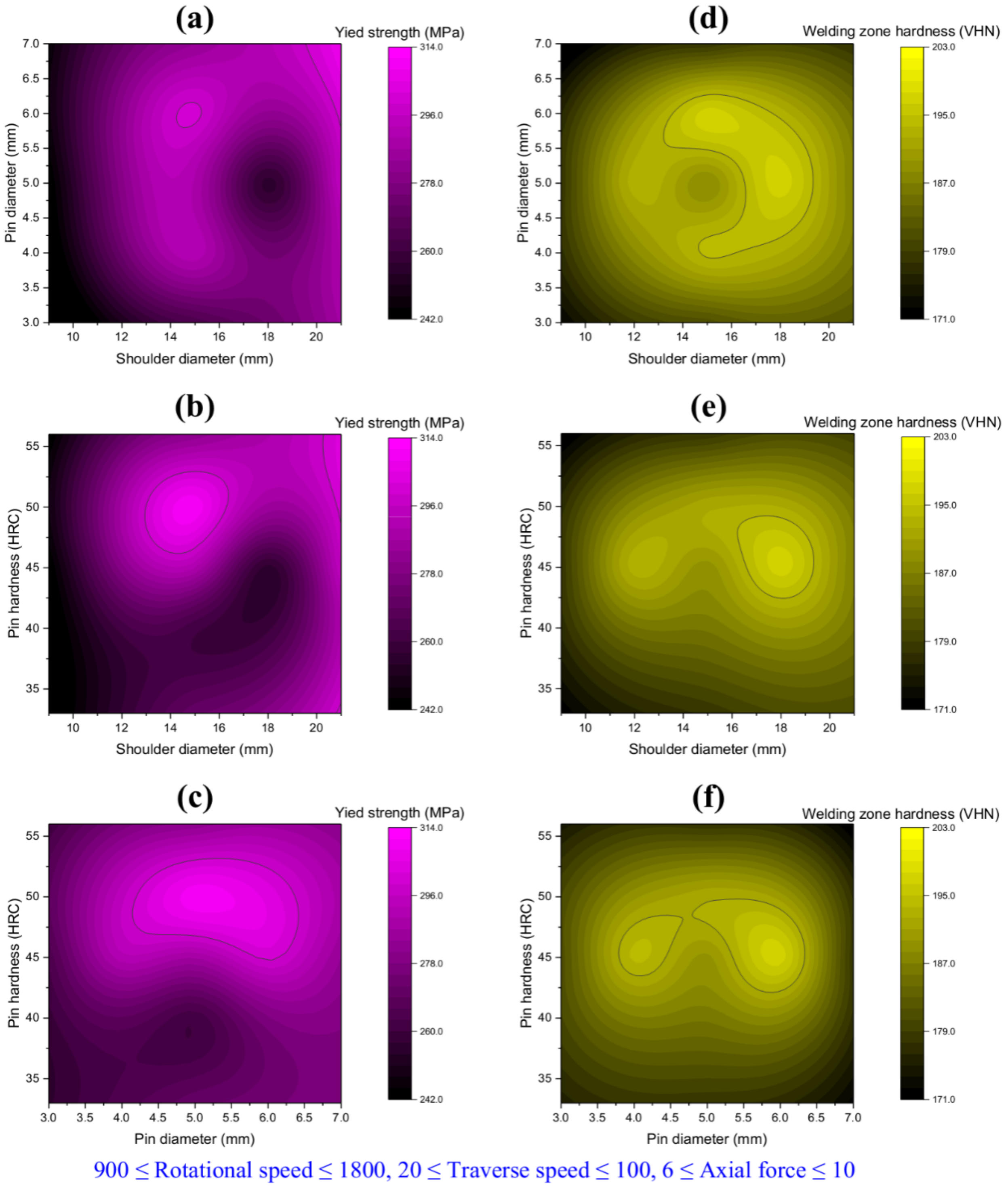

Figure 5. Parametric analysis of the effects of shoulder diameter, pin diameter, and tool hardness on strength (**a-c**) and hardness (**d-f**) of welded zone.

5. Conclusions

The application of DNN to model the FSW process was investigated in this study. The obtained results revealed that by using SAE for pre-training of neural networks higher accuracy can be obtained. In addition, it can be concluded that by applying DNN on small dataset with discrete values, continuous values for whole considered intervals can be predicted for parametric analysis of FSW. Moreover, these 2D contours with the accuracy of close to 100% can be easily used for further analysis and optimization. However, one of the challenges in this research was that the small dataset was used to estimate the tensile strength, but more studies are needed to optimize the hardness, and no specific trend was found for hardness changes in the welded area according to the investigated parameters. Therefore, in future research, the authors seek to perform more tests using design of experiment (DOE) techniques such as Taguchi method and considering more input parameters. In addition, the authors agree with the opinion of many reports that the main causes of failures of mechanical parts are the fatigue phenomenon [55]. Therefore, in the future research series, this research team seeks to model, analyse, and optimize the friction stir welding process of aluminium sheets with the aim of improving the fatigue life of the joint. For this, they will use various techniques including data mining, artificial intelligence, deep learning, etc. to make a comprehensive study. Also, the accuracy of the methods will be compared with each other and the advantages and disadvantages of each of them will be discussed.

Author Contributions

Conceptualization, E.M., O.U., and K.R.K.; methodology, E.M., O.U., S.M.S.S., and K.R.K.; software, E.M., O.U., and S.M.S.S.; validation, E.M., and O.U.; formal analysis, E.M., O.U., and K.R.K.; investigation, E.M., O.U., S.M.S.S., K.R.K., and N.A.; resources, E.M., O.U., and K.R.K.; data curation, E.M., and O.U.; writing—original draft preparation, E.M., O.U., S.M.S.S., and K.R.K.; writing—review and editing, K.R.K.; visualization, E.M., O.U., and K.R.K.; supervision, E.M., O.U., and K.R.K.; project administration, E.M., and K.R.K.; funding acquisition, E.M., O.U., and K.R.K., All authors have read and agreed to the published version of the manuscript.

Funding

This research received no external funding.

Acknowledgement

This paper has been supported by the RUDN University Strategic Academic Leadership Program.

Data Availability

The data that support the findings of this study are available from the corresponding author upon reasonable request.

Conflict of Interest

The authors declare no conflict of interest.

References

[1] Gite, R.A., Loharkar, P.K., Shimpi, R., 2019. Friction stir welding parameters and application: A review. Materials Today: Proceedings. 19, 361-365. DOI: https://doi.org/10.1016/j.matpr.2019.07.613

[2] Reza Kashyzadeh, K., Ghorbani, S., 2023. High-cycle fatigue behavior and chemical composition empirical relationship of low carbon three-sheet spot-welded joint: An application in automotive industry. Journal of Design Against Fatigue. 2(1), 1-8.

[3] Amiri, N., Farrahi, G.H., Kashyzadeh, K.R., et al., 2020. Applications of ultrasonic testing and machine learning methods to predict the static & fatigue behavior of spot-welded joints. Journal of Manufacturing Processes. 52, 26-34.

[4] Reza Kashyzadeh, K., Farrahi, G., Ahmadi, A., et al., 2023. Fatigue life analysis in the residual stress field due to resistance spot welding process considering different sheet thicknesses and dissimilar electrode geometries. Proceedings of the Institution of Mechanical Engineers, Part L: Journal of Materials: Design and Applications. 237(1), 33-51. DOI: https://doi.org/10.1177/14644207221101069

[5] Farrahi, G.H., Ahmadi, A., Kasyzadeh, K.R., 2020. Simulation of vehicle body spot weld failures due to fatigue by considering road roughness and vehicle velocity. Simulation Modelling Practice and Theory. 105, 102168. DOI: https://doi.org/10.1016/j.simpat.2020.102168

[6] Farrahi, G.H., Ahmadi, A., Kashyzadeh, K.R., et al., 2020. A comparative study on the fatigue life of the vehicle body spot welds using different numerical techniques: Inertia relief and Modal dynamic analyses. Frattura ed Integrità Strutturale. 14(52), 67-81. DOI: https://doi.org/10.3221/IGF-ESIS.52.06

[7] Farrahi, G.H., Kashyzadeh, K.R., Minaei, M., et al., 2020. Analysis of resistance spot welding process parameters effect on the weld quality of three-steel sheets used in automotive industry: Experimental and finite element simulation. International Journal of Engineering. 33(1), 148-157.

DOI: https://doi.org/10.5829/ije.2020.33.01a.17

[8] Friction Stir Butt Welding, International Patent Application No. PCT/GB92 [Internet]. International Patent Application No. PCT/GB92. GB Patent Application No. 9125978.8. Available from: https://cir.nii.ac.jp/crid/1570291224176390272

[9] Roldo, L., Vulić, N., 2019. Friction stir welding for marine applications: mechanical behaviour and microstructural characteristics of Al-Mg-Si-Cu plates. Transactions on Maritime Science. 8(1), 75-83.
DOI: https://doi.org/10.7225/toms.v08.n01.008

[10] Silva, A.C., Braga, D.F., De Figueiredo, M.A.V., et al., 2015. Ultimate tensile strength optimization of different FSW aluminium alloy joints. The International Journal of Advanced Manufacturing Technology. 79, 805-814.
DOI: https://doi.org/10.1007/s00170-015-6871-2

[11] Aydin, H., Bayram, A., Esme, U., et al., 2010. Application of grey relation analysis (GRA) and Taguchi method for the parametric optimization of friction stir welding (FSW) process. Materials and Technology. 44(4), 205-211.

[12] Ghetiya, N.D., Patel, K.M., Kavar, A.J., 2016. Multi-objective optimization of FSW process parameters of aluminium alloy using Taguchi-based grey relational analysis. Transactions of the Indian Institute of Metals. 69, 917-923.
DOI: https://doi.org/10.1007/s12666-015-0581-1

[13] Deepandurai, K., Parameshwaran, R., 2016. Multiresponse optimization of FSW parameters for cast AA7075/SiCp composite. Materials and Manufacturing Processes. 31(10), 1333-1341.
DOI: https://doi.org/10.1080/10426914.2015.1117628

[14] Bhushan, R.K., Sharma, D., 2019. Optimization of FSW parameters for maximum UTS of AA6082/SiC/10P composites. Advanced Composites Letters. 28, 0963693519867707.
DOI: https://doi.org/10.1177/0963693519867707

[15] Jain, S., Sharma, N., Gupta, R., 2018. Dissimilar alloys (AA6082/AA5083) joining by FSW and parametric optimization using Taguchi, grey relational and weight method. Engineering Solid Mechanics. 6(1), 51-66.
DOI: http://dx.doi.org/10.5267/j.esm.2017.10.003

[16] Lakshminarayanan, A.K., Balasubramanian, V., 2008. Process parameters optimization for friction stir welding of RDE-40 aluminium alloy using Taguchi technique. Transactions of Nonferrous Metals Society of China. 18(3), 548-554.
DOI: https://doi.org/10.1016/S1003-6326(08)60096-5

[17] Rajakumar, S., Muralidharan, C., Balasubramanian, V., 2010. Optimization of the friction-stir-welding process and tool parameters to attain a maximum tensile strength of AA7075-T6 aluminium alloy. Proceedings of the Institution of Mechanical Engineers, Part B: Journal of Engineering Manufacture. 224(8), 1175-1191.
DOI: https://doi.org/10.1243/09544054JEM1802

[18] Shanavas, S., Dhas, J.E.R., 2017. Parametric optimization of friction stir welding parameters of marine grade aluminium alloy using response surface methodology. Transactions of Nonferrous Metals Society of China. 27(11), 2334-2344.
DOI: https://doi.org/10.1016/S1003-6326(17)60259-0

[19] Elatharasan, G., Kumar, V.S., 2012. Modelling and optimization of friction stir welding parameters for dissimilar aluminium alloys using RSM. Procedia Engineering. 38, 3477-3481.
DOI: https://doi.org/10.1016/j.proeng.2012.06.401

[20] Jayaraman, M., Sivasubramanian, R., Balasubramanian, V., et al., 2009. Optimization of Process Parameters for Friction Stir Welding of Cast Aluminium Alloy A319 by Taguchi Method [Internet]. Available from: http://nopr.niscpr.res.in/handle/123456789/2786

[21] Verma, S., Kumar, V., 2021. Optimization of friction stir welding parameters of dissimilar aluminium alloys 6061 and 5083 by using response surface methodology. Proceedings of the Institution of Mechanical Engineers, Part C: Journal of Mechanical Engineering Science. 235(23), 7009-7020.
DOI: https://doi.org/10.1177/09544062211005804

[22] Yuvaraj, K.P., Varthanan, P.A., Haribabu, L., et al., 2021. Optimization of FSW tool parameters for joining dissimilar AA7075-T651 and AA6061 aluminium alloys using Taguchi Technique. Materials Today: Proceedings. 45, 919-925.
DOI: https://doi.org/10.1016/j.matpr.2020.02.942

[23] Ghangas, G., Singhal, S., Dixit, S., et al., 2022. Mathematical modeling and optimization of friction stir welding process parameters for armor-grade aluminium alloy. International Journal on Interactive Design and Manufacturing (IJIDeM). 1-18.
DOI: https://doi.org/10.1007/s12008-022-01000-1

[24] Ramesha, K., Sudersanan, P.D., Santhosh, N., et al., 2021. Design and optimization of the process parameters for friction stir welding of dissimilar aluminium alloys. Engineering and Applied Science Research. 48(3), 257-267.

[25] Gupta, S.K., Pandey, K.N., Kumar, R., 2018. Artificial intelligence-based modelling and multi-objective optimization of friction stir welding of dissimilar

AA5083-O and AA6063-T6 aluminium alloys. Proceedings of the Institution of Mechanical Engineers, Part L: Journal of Materials: Design and Applications. 232(4), 333-342.
DOI: https://doi.org/10.1177/1464420715627293

[26] Raj, A., Kumar, J.P., Rego, A.M., et al., 2021. Optimization of friction stir welding parameters during joining of AA3103 and AA7075 aluminium alloys using Taguchi method. Materials Today: Proceedings. 46, 7733-7739.
DOI: https://doi.org/10.1016/j.matpr.2021.02.246

[27] Verma, S., Gupta, M., Misra, J.P., 2018. Optimization of process parameters in friction stir welding of armor-marine grade aluminium alloy using desirability approach. Materials Research Express. 6(2), 026505.
DOI: https://doi.org/10.1088/2053-1591/aaea01

[28] Maleki, E., Unal, O., Seyedi Sahebari, S.M., et al.,2023. A novel approach for analyzing the effects of almen intensity on the residual stress and hardness of shot-peened (TiB+ TiC)/Ti–6Al–4V composite: Deep learning. Materials. 16(13), 4693.
DOI: https://doi.org/10.3390/ma16134693

[29] Maleki, E., Unal, O., Seyedi Sahebari, S.M., et al., 2022. Application of deep neural network to predict the high-cycle fatigue life of AISI 1045 steel coated by industrial coatings. Journal of Marine Science and Engineering. 10(2), 128.
DOI: https://doi.org/10.3390/jmse10020128

[30] Padhy, G.K., Wu, C.S., Gao, S, 2018. Friction stir based welding and processing technologies-processes, parameters, microstructures and applications: A review. Journal of Materials Science & Technology. 34(1), 1-38.
DOI: https://doi.org/10.1016/j.jmst.2017.11.029

[31] Gangwar, K., Ramulu, M., 2018. Friction stir welding of titanium alloys: A review. Materials & Design. 141, 230-255.
DOI: https://doi.org/10.1016/j.matdes.2017.12.033

[32] Mohanty, H.K., Mahapatra, M.M., Kumar, P., et al., 2012. Modeling the effects of tool shoulder and probe profile geometries on friction stirred aluminum welds using response surface methodology. Journal of Marine Science and Application. 11, 493-503.
DOI: https://doi.org/10.1007/s11804-012-1160-z

[33] Ahmed, S., Rahman, R.A.U., Awan, A., et al., 2020. Optimization of process parameters in friction stir welding of aluminum 5451 in marine applications. Journal of Marine Science and Engineering. 10(10), 1539.
DOI: https://doi.org/10.3390/jmse10101539

[34] Kumar, D.A., Biswas, P., Tikader, S., et al., 2013. A study on friction stir welding of 12mm thick aluminum alloy plates. Journal of Marine Science and Application. 12, 493-499.
DOI: https://doi.org/10.1007/s11804-013-1221-y

[35] Ganjabi, M.A., Farrahi, G., Reza Kashyzadeh, K., et al., 2023. Effects of various strength defects of spot weld on the connection strength under both static and cyclic loading conditions: empirical and numerical investigation. The International Journal of Advanced Manufacturing Technology. 127, 5665-5678.
DOI: https://doi.org/10.1007/s00170-023-11923-y

[36] Boukraa, M., Lebaal, N., Mataoui, A., et al., 2018. Friction stir welding process improvement through coupling an optimization procedure and three-dimensional transient heat transfer numerical analysis. Journal of Manufacturing Processes. 34, 566-578.
DOI: https://doi.org/10.1016/j.jmapro.2018.07.002

[37] Heidarzadeh, A., Chabok, A., Pei, Y., 2019. Friction stir welding of Monel alloy at different heat input conditions: Microstructural mechanisms and tensile behavior. Materials Letters. 245, 94-97.
DOI: https://doi.org/10.1016/j.matlet.2019.02.108

[38] Chu, Q., Li, W.Y., Yang, X.W., et al., 2018. Microstructure and mechanical optimization of probeless friction stir spot welded joint of an Al-Li alloy. Journal of Materials Science & Technology. 34(10), 1739-1746.
DOI: https://doi.org/10.1016/j.jmst.2018.03.009

[39] Sreenivasan, K.S., Kumar, S.S., Katiravan, J., 2019. Genetic algorithm based optimization of friction welding process parameters on AA7075-SiC composite. Engineering Science and Technology, an International Journal. 22(4), 1136-1148.
DOI: https://doi.org/10.1016/j.jestch.2019.02.010

[40] Heidarzadeh, A., Barenji, R.V., Khalili, V., et al., 2019. Optimizing the friction stir welding of the α/β brass plates to obtain the highest strength and elongation. Vacuum. 159, 152-160.
DOI: https://doi.org/10.1016/j.vacuum.2018.10.036

[41] Heidarzadeh, A., 2019. Tensile behavior, microstructure, and substructure of the friction stir welded 70/30 brass joints: RSM, EBSD, and TEM study. Archives of Civil and Mechanical Engineering. 19(1), 137-146.
DOI: https://doi.org/10.1016/j.acme.2018.09.009

[42] He, X., Gu, F., Ball, A., 2014. A review of numerical analysis of friction stir welding. Progress in Materials Science. 65, 1-66.
DOI: https://doi.org/10.1016/j.pmatsci.2014.03.003

[43] Maleki, E., Bagherifard, S., Razavi, S.M.J., et al., 2022. On the efficiency of machine learning for fa-

tigue assessment of post-processed additively manufactured AlSi10Mg. International Journal of Fatigue. 160, 106841.
DOI: https://doi.org/10.1016/j.ijfatigue.2022.106841

[44] Maleki, E., Unal, O., Kashyzadeh, K.R., 2019. Surface layer nanocrystallization of carbon steels subjected to severe shot peening: Analysis and optimization. Materials Characterization. 157, 109877.
DOI: https://doi.org/10.1016/j.matchar.2019.109877

[45] Maleki, E., Unal, O., Kashyzadeh, K.R., 2018. Fatigue behavior prediction and analysis of shot peened mild carbon steels. International Journal of Fatigue. 116, 48-67.
DOI: https://doi.org/10.1016/j.ijfatigue.2018.06.004

[46] Reza Kashyzadeh, K., Amiri, N., Ghorbani, S., et al., 2022. Prediction of concrete compressive strength using a back-propagation neural network optimized by a genetic algorithm and response surface analysis considering the appearance of aggregates and curing conditions. Buildings. 12(4), 438.
DOI: https://doi.org/10.3390/buildings12040438

[47] Dewan, M.W., Huggett, D.J., Liao, T.W., et al., 2016. Prediction of tensile strength of friction stir weld joints with adaptive neuro-fuzzy inference system (ANFIS) and neural network. Materials & Design. 92, 288-299.
DOI: https://doi.org/10.1016/j.matdes.2015.12.005

[48] Maleki, E., 2015. Artificial neural networks application for modeling of friction stir welding effects on mechanical properties of 7075-T6 aluminum alloy. IOP Conference Series: Materials Science and Engineering. 103(1), 012034.
DOI: https://doi.org/10.1088/1757-899X/103/1/012034

[49] Shojaeefard, M.H., Behnagh, R.A., Akbari, M., et al., 2013. Modelling and Pareto optimization of mechanical properties of friction stir welded AA7075/AA5083 butt joints using neural network and particle swarm algorithm. Materials & Design. 44, 190-198.
DOI: https://doi.org/10.1016/j.matdes.2012.07.025

[50] Maleki, E., Bagherifard, S., Guagliano, M., 2022. Application of artificial intelligence to optimize the process parameters effects on tensile properties of Ti-6Al-4V fabricated by laser powder-bed fusion. International Journal of Mechanics and Materials in Design. 18(1), 199-222.
DOI: https://doi.org/10.1007/s10999-021-09570-w

[51] Kashyzadeh, K.R., Ghorbani, S., 2023. New neural network-based algorithm for predicting fatigue life of aluminum alloys in terms of machining parameters. Engineering Failure Analysis. 146, 107128.
DOI: https://doi.org/10.1016/j.engfailanal.2023.107128

[52] Hinton, G.E., Osindero, S., Teh, Y.W., 2006. A fast learning algorithm for deep belief nets. Neural Computation. 18(7), 1527-1554.
DOI: https://doi.org/10.1162/neco.2006.18.7.1527

[53] Feng, S., Zhou, H., Dong, H., 2019. Using deep neural network with small dataset to predict material defects. Materials & Design. 162, 300-310.
DOI: https://doi.org/10.1016/j.matdes.2018.11.060

[54] Rajakumar, S., Muralidharan, C., Balasubramanian, V., 2011. Influence of friction stir welding process and tool parameters on strength properties of AA7075-T6 aluminium alloy joints. Materials & Design. 32(2), 535-549.
DOI: https://doi.org/10.1016/j.matdes.2010.08.025

[55] Arghavan, A., Reza Kashyzadeh, K., Asfarjani, A.A., 2011. Investigating effect of industrial coatings on fatigue damage. Applied Mechanics and Materials. 87, 230-237.
DOI: https://doi.org/10.4028/www.scientific.net/AMM.87.230

Appendix A

The data used in this research, including various welding conditions and laboratory results of tensile and microhardness tests, are given in Table A1.

Table A1. The data used in the current study, including welding conditions and testing results.

Case No.	**FSW Process Parameters**			**Tool Features**			**Responses in Welded Zone**	
	Rotational speed (rpm)	Transverse speed (mm/min)	Axial force (KN)	Shoulder diameter (mm)	Pin diameter (mm)	Tool hardness (HRc)	Strength (MPa)	Hardness (VHN)
1	1400	60	8	15	5	45	314	203
2	1800	60	8	15	5	45	310	185
3	1400	40	8	15	5	45	279	194
4	1400	60	8	15	5	45	310	198
5	1400	80	8	15	5	45	308	197
6	1400	60	7	15	5	45	282	180
7	1400	60	8	15	5	45	314	199

Table A1 continued

Case No.	**FSW Process Parameters**			**Tool Features**			**Responses in Welded Zone**	
	Rotational speed (rpm)	Transverse speed (mm/min)	Axial force (KN)	Shoulder diameter (mm)	Pin diameter (mm)	Tool hardness (HRc)	Strength (MPa)	Hardness (VHN)
8	1400	60	8	12	5	45	280	193
9	1400	60	8	15	5	45	310	198
10	1400	60	8	18	5	45	256	197
11	1400	60	8	15	4	45	292	194
12	1400	60	8	15	5	45	310	198
13	1400	60	8	15	6	45	300	197
14	1400	60	8	15	5	40	261	186
15	1400	60	8	15	5	45	313	198
16	900	60	8	15	5	45	245	175
17	1200	60	8	15	5	45	290	191
18	1400	20	8	15	5	45	255	180
19	1400	100	8	15	5	45	245	179
20	1400	60	6	15	5	45	263	173
21	1400	60	10	15	5	45	285	171
22	1400	60	8	9	5	45	242	178
23	1400	60	8	21	5	45	296	187
24	1400	60	8	15	3	45	264	181
25	1400	60	8	15	7	45	284	178
26	1400	60	8	15	5	33	271	178
27	1400	60	8	15	5	56	282	178
28	1400	60	9	15	5	45	301	190
29	1400	60	8	15	5	50	310	192
30	1600	60	8	15	5	45	314	202

Source: Maleki, E., 2015 [48].

Sustainable Marine Structures
https://journals.nasspublishing.com/index.php/sms

ARTICLE

Assist in GHG Abatement of Offshore Ships: Design and Economic Analysis of an Integrated Utilization Model of Hydrogen-powered Ship and Offshore Wind Power

Xinyu Liu[1] **Guogang Yang**[1*] **Baixun Sun**[1] **Hao Wang**[1] **Yue Li**[2] **Renjie Wang**[2]

1. Marine Engineering College, Dalian Maritime University, Dalian, Liaoning, 116026, China
2. Laboratory of Transport Pollution Control and Monitoring Technology, Beijing, 100084, China

ARTICLE INFO

Article history
Received: 17 June 2023
Revised: 9 August 2023
Accepted: 14 August 2023
Published Online: 23 August 2023

Keywords:
GHG abatement
Hydrogen-powered ships
Hydrogen production from offshore wind power
PEMFC ships
Integrated utilization model
Economic analysis

ABSTRACT

As a hopeful solution to help the shipping sector achieve the greenhouse gas (GHG) abatement goal of the IMO by 2050, the application of hydrogen-powered ships has attracted more and more attention. To solve the problem of hydrogen supplement for offshore polymer electrolyte membrane fuel cell (PEMFC) ships, this paper presents a scenario design for the integrated application of coastal hydrogen-powered ships and offshore wind power, and analyzes its techno-economic feasibility. This model concept considers the problems in offshore hydrogen transportation and offshore wind power development together. It provides a feasible integrated scheme and operation mode for the combination of offshore wind power and hydrogen energy storage. A transformation scheme is also provided for the marine ranch ships, and these PEMFC-powered ships are combined with the hydrogen production of offshore wind farms. The analysis results show that the integrated utilization model is economically feasible and with a significant effect on decarbonization. It also shows great potential for further expansion to other coastal areas.

1. Introduction

To achieve carbon neutrality in the future, carbon emissions need to be controlled from the energy consumption side and energy production side respectively. On the side of energy consumption, the main consideration are industrial power and transport carbon reduction. There is already a good measure to reduce carbon in land transport, namely electrification [1], when traditional battery energy storage cannot meet the demand alone, polymer electrolyte membrane fuel cells (PEMFCs) power can be coupled with it to achieve a longer endurance and faster energy replenishment speed. Before being applied to civil ships, the more mature power application of fuel cells (FCs) in ships

---

*Corresponding Author:
Guogang Yang,
Marine Engineering College, Dalian Maritime University, Dalian, Liaoning, 116026, China;
Email: yanggg@dlmu.edu.cn

DOI: http://dx.doi.org/10.36956/sms.v5i2.877

is PEMFC in the HDW submarines working as air independent propulsion (AIP) [2]. This type of submarine has been in service since the 1990s. In the civil market, Golden Gate Zero Emission Marine, an American company, built the first hydrogen fuel cell ship in 2018. It's called Water Go Round, with a maximum speed of 22 knots and 84 passengers. The low density of hydrogen and the PEMFC's proneness of remarkable degradation restrict the application of PEMFC in surface ships. When it is used on ships, the hydrogen-fueled PEMFC is usually hybridized with a battery energy storage system [3]. PEMFC and lithium-ion batteries both have the problem of remarkable degradation which raises the need for an energy management strategy [4]. According to the research of Chiara Dall' Armi et al., with an appropriate energy management strategy, the overall lifetime of the plant can be increased more than twice [5]. With the ageing of components, the decrease in PEMFC efficiency leads to an increase in hydrogen consumption [6]. This cause the need for additional space for the hydrogen storage system to ensure the normal operation of the ship after a period of service. The lifetime and hydrogen storage problems faced by PEMFC ships will be gradually solved in the process of PEMFC transportation industry development. In contrast, the scheme proposed in this paper focuses more on the hydrogen refuelling of PEMFC ships. For carbon reduction in offshore transportation, offshore fishing boats and small sightseeing boats are suitable to use PEMFC to achieve zero carbon emission, with appropriate control and optimization strategies, and energy storage systems [7]. However, it is difficult to refuel hydrogen when it is sailing on the sea, and frequent landing for hydrogen charging would bring a lot of inconvenience to its normal operation. It is also important to note that, if blue hydrogen is used, its life-cycle greenhouse gas emission intensity is still higher than that of LNG and diesel [8,9], because of the large amount of CO_2 emissions during the hydrogen generation process of the SMR and the electricity consumed in the hydrogen compression process [10]. Green hydrogen must be used if hydrogen-powered maritime transport is to achieve a full life-cycle of zero carbon [11], but it accounts for only 1% of the domestic hydrogen production in China. This problem brings our focus to a wide range of renewable sources of energy, also located offshore.

wind energy is favored by many countries in the world because of its short construction cycle, low environmental requirements, rich reserves and high utilization ratio. Offshore wind power also has advantages such as non land occupation and being close to the load center area with high power demand [12]. The power of wind power depends on the natural wind and is affected by many natural factors. Its fluctuation and irregularity make it difficult to be fully integrated into the grid even if it is coordinated with other power sources for peak shaving [13]. Under such circumstances, this extra part of wind power is forced to be abandoned [14]. Storing and distributing hardto- use wind power can effectively improve the utilization rate of wind power, but traditional electromagnetic energy storage methods cannot meet the demand for wind energy storage [15], and it's difficult to use those traditional storage systems in the marine environment. Under these circumstances, hydrogen energy storage systems appear as an alternative to conventional storage technologies [16]. The green hydrogen produced by wind power can be used for PEMFC-powered transportation to achieve zero carbon emissions for the whole life cycle and help increase the efficiency of renewable energy use and their share in the energy mix [17,18]. With the wind-hydrogen energy storage system, massive wind energy curtailment can be converted into commercial profits [19,20]. It can even build a dedicated wind farm for hydrogen production, some researchers have demonstrated the feasibility of this model [21]. But compared to conventional liquid fuels, hydrogen has a low volumetric energy density, which brings problems to its storage and transport. This problem is also reflected in hydrogen production from wind power fields in previous industrial projects [22-24]. The NORTH2 project in the Netherlands uses large offshore hydrogen plants to deliver wind power [25]. AquaPrimus is the first sub-project of the German AQUAVENTUS project, and it plans to 2028 a hydrogen plant on the base of a wind turbine to deliver green hydrogen to the region through specially laid pipelines. Poshydon of the Netherlands, the world's first offshore wind-hydrogen project, will use a natural gas pipeline to mix hydrogen and natural gas into its national gas pipeline network [26,27].

Most of the existing plans for offshore hydrogen production worldwide are designed to take into account the demand for hydrogen on land, and the annual output often reaches 10,000 tons or even 100,000 tons, so they can only consider the way of sending wind power to shore or offshore platform to make hydrogen by pipeline to shore, not considering the possibility of hydrogen storage and consumption offshore. There have also been examples of combining hydrogen generation from wind power with characteristic transportation demand, but these attempts are also applicable to the land transportation field [28,29], in order to supply hydrogen produced by wind power for PEMFC vehicles [30]. Using green fuels like these green hydrogen to replace traditional fossil fuels is an effective way for the maritime sector to reduce carbon emissions [31]. If each of the scattered offshore hydrogen platforms in the offshore hydrogen project is used to supply a group of coastal PEMFC ships with relatively fixed but not massive hydrogen, then there is no need to consider the transport of hydrogen. Marine ranch is well suited for this, with a fixed number of ships and a fixed working trajectory. Therefore, offshore hydrogen production platforms and offshore hydrogen refuelling stations can be considered at locations close to both marine ranch and wind farms, allowing PEMFC-powered ships to refuel hydrogen on their daily route. The energy consumption of the marine ranch ships is relatively fixed every day, and the offshore hydrogen production platform can be produced on demand according to the surrounding conditions, which can reduce the cost of the hydrogen storage process and unnecessary energy loss, and avoid the hydrogen storage and consumption problems that offshore hydrogen station faced before. The main challenge of applying green hydrogen to ships is the storage of H_2 on ships [31], however, in this mode, PEMFC ships can timely replenish hydrogen near the work area, which to some extent alleviates the problem of hydrogen storage. In the future, it can also cooperate with the composite hydrogen storage technology with higher capacity, lower weight, and improved safety [32] to further solve the problem of hydrogen storage on ships. Based on it, this paper presents a scenario design for the integrated application of coastal PEMFC ships and offshore hydrogen stations by wind power. It aims to solve the hydrogen refuelling problem of offshore PEMFC ships and provide a feasible integrated scheme and operation mode for the combination of offshore wind power and hydrogen energy storage. The analysis of the daily operation of offshore hydrogen stations and marine ranch PEMFC ships shows that this model is economically feasible. It also shows great potential for further expansion to other coastal areas.

2. Model Description

This model uses a grid-connected way of hydrogen production from wind power, because it can obtain power from the power grid to maintain the normal operation of the alkaline electrolytic cell when the output power of wind turbines cannot meet the requirements. If the system only relies on wind power without coordinating the power grid, it may cause damage to the electrolytic cell when the fluctuation is large. The offshore hydrogen production and refuelling station can be built on the original offshore platform of the wind farm. It uses alkaline electrolytic cells to produce hydrogen. Although using proton exchange membrane water electrolysis (PEMWE) can obtain lower energy consumption and higher hydrogen purity, it brings higher costs and requires more frequent maintenance which makes it less suitable for this scenario than alkaline electrolytic cells.

In this scenario design, the quantity, types and performance parameter data of the ships in designated marine ranch were taken into consideration to specify the corresponding transformation scheme, and shows the theoretical hydrogen consumption data. The output of offshore hydrogen stations is set based on the daily hydrogen demand of these ships, and the redundancy is reserved to cope with different conditions. The wind power output allocated for offshore hydrogen stations is set based on the power consumption of developed alkaline electrolytic cells, hydrogen purification/compression devices and other equipment. The power consumption of the whole hydrogen production process is set as 5.156 kWh/Nm^3. In the actual operation, the dispatching control system needs to adjust the power according to the available idle wind power data to meet the requirements of the power grid and all hydrogen production equipment at the same time. However, the main starting point of this model is to provide the nearby hydrogen supply for the application of PEMFC on offshore vessels. Therefore, this paper sets the power supply and hydrogen output of offshore wind stations as a constant mean. The calculation part of this paper is focused on the cost recovery period, net profit and emission reduction. In the calculation process, it uses the ideal state with additional redundancy upper limit to approximately replace the fluctuations caused by various practical factors. The energy flow path of this scenario designed is shown in Figure 1.

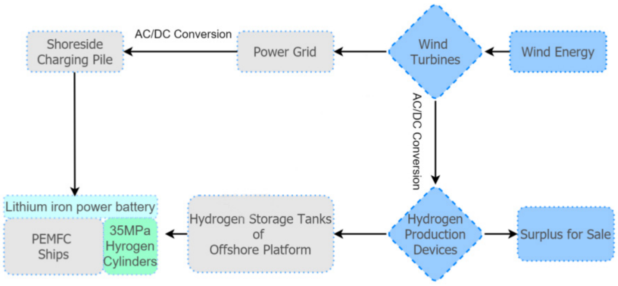

Figure 1. The flow path of energy in this scenario.

A wind farm project in the Yellow Sea in northeast China, covering an area of about 48 square kilometers, is the background of the initial scenario design for the demonstration of PEMFC ships and offshore hydrogen stations. The center of the site is located about 19.1 km from the coast. There are 60 wind turbines with a total installed capacity of 300 MW.

In this initial scenario of integrated utilization, offshore wind farm investors will invest in a 1,000 kg per day offshore hydrogen production and refuelling station on an offshore platform about 15 kilometers offshore, and the H_2 is sold to hydrogen-powered breeding boats and sightseeing boats of a nearby marine ranch. Investors of the marine ranch invest in hybrid PEMFC boats with hydrogen fuel cells and power batteries that use hydrogen from offshore wind farms to replace conventional diesel fuel. On the one hand, it can save some fuel costs under the current subsidy policy, on the other hand, it can avoid the emission of diesel engines, and improve the efficiency of energy conversion, so as to achieve the effect of energy saving and emission reduction.

The investors of the marine ranch have invested about 1.44 million $ to build an offshore leisure platform in the marine ranch, which will integrate offshore fishing and offshore sightseeing, and make it a comprehensive platform that takes into account both tourism and aquaculture operations. As shown in Figure 2, the ranch boats and tourist boats use the power provided by the battery system to drive to the offshore hydrogen station of the wind farm for refuelling in the morning and then the boats can go to the working area, sightseeing boats are responsible for transporting tourists to and from tourist attractions and the shore. All of the ships return to offshore hydrogen stations before running out of fuel, return to shore at the end of the day and recharge at night through shore-based charging posts.

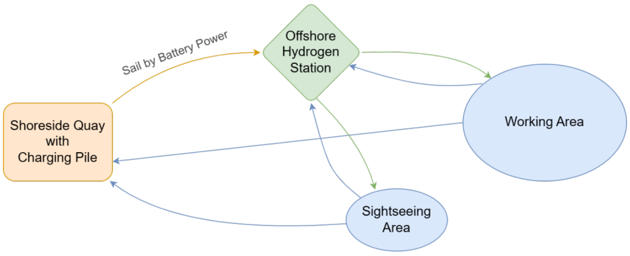

Figure 2. Daily route of marine ranch ships in this scenario.

3. Results

3.1 Composition and Analysis of Investment Cost

Initial Investment Estimate of Offshore Hydrogen Plant

The hydrogen station needs about 58000 kWh to produce 1000 kg of hydrogen per day. To meet this production capacity, the hydrogen station needs to be equipped with a 2.5 MW electrolytic hydrogen production system. (The energy conversion efficiency of the entire system is recorded as 55%). The cost of hydrogen production in offshore wind farms is mainly composed of the cost of the offshore converter station, the hydrogen production system, the hydrogen compressor, the hydrogen cylinders, the hydrogen charging system and the installation costs, as shown in Table 1. The hydrogen production system consists of a seawater desalination unit and an electrolytic water hydrogen production unit, the hydrogen charging system includes the charge machine, the hydrogen pipeline system, the dispersing system, the displacement purging system, the instrument air system, the safety monitoring system and other pipeline materials for connection. The hydrogen compressor requires two diaphragm compressors with a rated exhaust pressure of 45 MPa and a hydrogen compression rate of 500 kg per day. The hydrogen cylinder adopts a 45 MPa hydrogen cylinders group, and the hydrogen charging system needs four 35 MPa charging machines. The installation cost is estimated according to 10% of the total cost, and the initial investment of the offshore hydrogenation station is about 3.469 million $, expressed in C_{CF}.

Table 1. Cost estimates for offshore hydrogen stations.

Equipment	Unit Prise (million $)	Total Cost (million $)
Offshore converter station	0.287/MW	0.718
Hydrogen production system	0.287/MW	0.718
Hydrogen compressor	0.431	0.862
Cylinders and refueling systems	0.825	0.825
Installation costs	0.346	0.346
Total cost		3.469

Initial Investment Estimates for Marine Ranch

After conducting research on marine ranches that integrate aquaculture and tourism, such as the Genghai No.1, the small breeding boats and sightseeing boats that are commonly used are selected as the expected renovation targets. The basic parameters of 30 working boats and 15 sightseeing boats for the marine ranch are shown in Table 2.

Table 2. Basic parameters of marine ranch boats.

Parameter	Breeding Boat	Sightseeing Boat
Speed (knots)	9	10
Length (m)	10	13.5
Ship width (m)	2.85	3.5
Draft (rice)	0.59	0.73
Engine power (kW)	16	60
Daily working hours (h)	10	10

As shown in Table 3, the fuel cell system power of the breeding boat is 20 kW, which considers both power generation and bucking-wave performance. With a power cell capacity of 40 kWh, it can run at 9 knots while operating at 80% performance output. The fuel cell system power of the sightseeing boat is 75 kW, with a power cell capacity of 150 kWh. The design principle is that it can be used as a separate energy source for ships to operate at rated power for more than 2 h, and can supplement the power needed for bucking-wave navigation, and be used as backup power for electric valves and other equipment. A 35 MPa gas cylinder has an H2 storage density of 20-22 g/L and a hydrogen storage capacity of about 3 kg. The endurance is calculated according to the working condition of these ships at rated power, and it requires that ships operate at rated power and run for more than 5 hours.

Table 3. PEMFC ship modification plan for marine ranch.

	Breeding Boat	**Sightseeing Boat**
Power of fuel cell system (kW)	20	75
Power cell capacity (kWh)	40	150
Rated power (kW)	16	60
Bottle pressure (MPa)	35	35
Volume of carbon fiber bottle (L)	140	140
Number of carbon fiber bottles	2	8
Hydrogen storage (kg)	6	24
Sailing duration (h)	5.6	6
Number of vessels	30	15

As shown in Table 4, the modification costs of hydrogen- powered boats include the cost of fuel cell power generation system, hydrogen storage system, power cell system, accessory cost and other costs. Accessories mainly include electric propulsion systems, power grids and power control systems. Other costs consist of labor costs and hull modification costs. The cost of a fuel cell system is about 718 \$/kW, the cost of a power cell is about 215.5 \$/kWh, the hydrogen storage capacity of 35 MPa hydrogen cylinder is about 3 kg, and the cost of a single cylinder is about 2155\$, the initial investment for the marine ranch boats transformation is about 3.32 million \$.

Table 4. Cost estimation of marine ranch PEMFC ship modification.

Part of the Cost	**Cost of Breeding Boat (\$)**	**Cost of Sightseeing Boat (\$)**
Fuel cell system	14,368	53,880
Power battery system	8,620	32,328
Hydrogen storage system	4,310	17,241
Cost of accessories	7,184	28,736
Other costs	2,874	14,368
Cost of upgrading a single ship	37,356	146,553

It costs 58200\$ to build thirty 7 kW charging posts at 144\$ and fifteen 120 kW charging posts at 3592\$, as shown in Table 5, the initial investment cost of the marine ranch investor is about 4.815 million \$, expressed in CCR including 3.32 million \$ to retrofit a hydrogen-powered ship, 58200\$ for charging posts and 1.437 million \$ for a marine sightseeing-entertainment platform.

Table 5. Cost estimation of shore charging posts.

	Unit price (\$)	Total cost (\$)
7 kW charging post	144	4,320
120 kW charging post	3,592	53,880
Total cost of charging posts		58,200

3.2 Cost Recovery Period Analysis

Cost Recovery Period Analysis of Offshore Wind Farm Investors

According to the above data, the initial investment cost of offshore hydrogen station (C_{CF}) is 3.469 million \$.

About 1,000 kg of hydrogen produced per day are sold to the marine ranch at 2.87\$ per kilogram. Calculated by 300 days per year (matching the business hours of the marine ranch), the annual income can reach 0.862 million \$. An annual investment of 0.534 million \$ will be required,

including annual maintenance costs (34483\$ at 1 percent of the cost of the equipment) and electricity consumption costs (0.5 million \$ for 58,000 kWh electricity per day at 0.0287\$ per kWh). Therefore, the annual net income can reach 0.328 million \$, expressed in C_{IF}. According to Initial investment/annual net income = years of cost recovery, described by equation (1).

$$T_F=C_{CF}/C_{IF} \tag{1}$$

The years of cost recovery for wind farms without subsidies can be calculated. In Dalian, a one-off subsidy of up to 0.862 million \$ (expressed in C_{SF}) will be given to new hydrogen refueling stations put into use after 2023, not exceeding 30 percent of the investment. According to Initial investment subtract subsidies/annual net income = years of cost recovery with subsidies, described by equation (2).

$$T_{SF}=(C_{CF}-C_{SF})/C_{IF} \tag{2}$$

The years of cost recovery for wind farms with subsidies can be calculated, as shown in Table 6.

Wind farm investors can earn a profit of 0.328 million \$ a year from the sale of hydrogen. Without taking into account subsidies, investors can recover the cost of their initial investment in 10.59 years, if the government subsidies for the construction of hydrogen stations (onshore) are taken into account, the investment cost recovery period will be shortened to 7.96 years, and the government subsidies can bring the cost recovery period forward to about 2.63 years, if the government in the follow-up to the construction of offshore hydrogen station subsidies.

Table 6. Cost recovery years for offshore wind farm investors.

Component	Amount (million $)
Initial investment	3.467
Annual income	0.862
Annual expenses	0.534
Annual net income	0.328
Cost recovery period	10.59
Cost recovery period (subsidy)	7.96

Analysis of Cost Recovery Period of the Marine Ranch Investor

Based on the above data, it can be calculated that the cost of rebuilding the ship is 3.319 million $, the cost of shore charging posts is 58200$, the cost of building an offshore integrated entertainment platform is 1.437 million $, and the initial investment of marine ranch is 4.81 million $, expressed in C_{CR}. It also needs to invest 0.287 million $ a year in the operation and maintenance of the hydrogen-powered ships, taking the fuel cost savings compared with traditional diesel ships and the entrance fees of the offshore integrated platform as income. Then the annual net income of marine ranch investors' hydrogen investment can reach 0.552 million $, expressed in C_{IR}. Taking into account Dalian's subsidies at 0.498 million $ (expressed in C_{SR}), for 15% of the total 2023 cost of hydrogen- powered ships purchased and put into operation in 2023, according to Initial investment/annual net income = years of cost recovery, described by Equations (3) and (4).

$$TR = C_{CR}/C_{IR} \tag{3}$$

$$TSR = (C_{CR} - C_{SR})/C_{IR} \tag{4}$$

We can calculate the years of cost recovery with and without subsidies for marine ranch investors, as shown in Table 7.

Table 7. Marine ranch investors' cost recovery years.

Component	Amount (million $)
Initial investment	4.81
Annual income	0.839
Annual expenses	0.287
Annual net income	0.552
Cost recovery period	8.73
Cost recovery period (subsidy)	7.82

The total diesel consumption of 30 marine ranch breeding boats with the same performance parameters is about 1320 liters per day, and that of 15 sightseeing boats with the same performance parameters is about 2460 liters per day, which is a total of 3780 liters, the price of diesel is calculated at 1.12$ per liter and the annual working days are calculated at 300 days. The annual fuel cost of marine ranch ships is about 1.266 million $, and the annual fuel cost of the hydrogen-powered ships is 0.862 million $, which can save 0.404 million $ per year. The price of the ticket for the marine entertainment platform is set at 12.79$ per person, calculated on the basis of 40,000 tourists per year, with an annual income of 0.511 million $.

The annual net income of marine ranch can reach 0.552 million $. Without taking into account subsidies, marine ranch investors can recover the cost of their initial investment after 8.73 years, if the government subsidy for the hydrogen station is taken into account, this marine ranch can complete the cost recovery of the initial investment after 7.82 years. The government subsidy can bring the cost recovery period forward by about one year.

3.3 Cost Recovery Period Analysis Considering Other Influencing Factors

In the last part of the cost-recovery cycle, we only assumed that the offshore hydrogen station is matched with the operation of the marine ranch and only produces hydrogen 300 days a year. But if the plant is operating year-round, selling excess hydrogen to other users for revenue, the cost-recovery cycle could be further shortened to 6.54 years, as shown in Figure 3. The sightseeing revenue of the marine ranch before was assumed to be constant every year, but this new model of tourism has the potential for continuous development and expansion. If tourism profits increase by 5% every year, the cost-recovery cycle could be shortened to about seven years, and total profits over the first 20 years would be about 65 percent higher. (This growth model becomes less credible as the period grows). In this scenario designed, the offshore hydrogen station is currently matched with the operating time of the marine ranch. However, if it operates year-round and sells excess hydrogen to other users, it will gain higher profits, as shown in Figure 4.

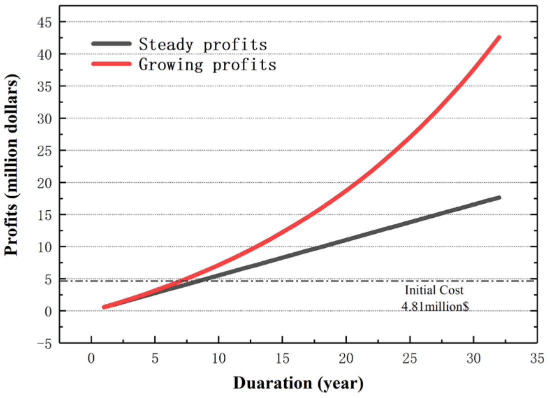

Figure 3. Total net income from marine ranch sightseeing

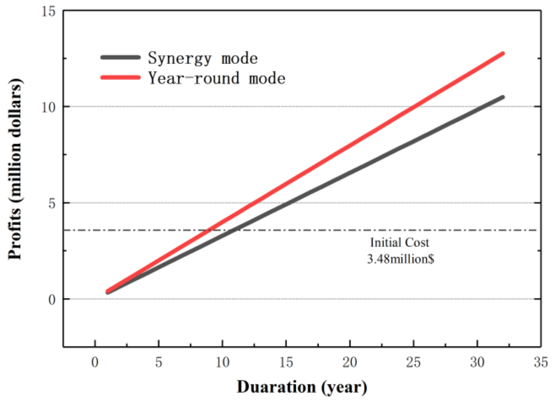

Figure 4. Total net revenue of offshore hydrogen stations.

In this scenario, factors such as changes in hydrogen price, changes in the technological maturity of PEMFC system, and the level of equipment maintenance and management will all have impacts on the cost recovery period. Therefore, further sensitivity analysis is needed. The impact of changes in the above factors on the results is shown in Figures 5, 6, 7, and 8.

In fact, the growth level of marine ranch tourism income will be affected by multiple factors and present uncertainty. The change in hydrogen price is the most intuitive factor affecting the operating profit of PEMFC ship users. When the average price of hydrogen gas is different, the change curve of the cost recovery period for investors of PEMFC ships is shown in Figure 5, and its impact on the cost recovery period of the hydrogen station is shown in Figure 6. (The upper price limit of 20 RMB for H2 sold by hydrogen station is stipulated by preferential policies). From them, it can be seen that hydrogen prices within the range of 2.65 $/kWh to 2.88 $/ kWh are more suitable for both parties, which can control the cost recovery period of both parties within 10 years. In addition, the current policy subsidies have a more significant helping effect on the offshore hydrogen station.

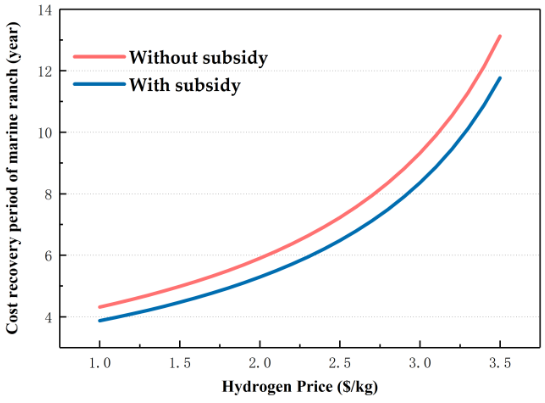

Figure 5. The cost recovery period of marine ranch is affected by H_2 price.

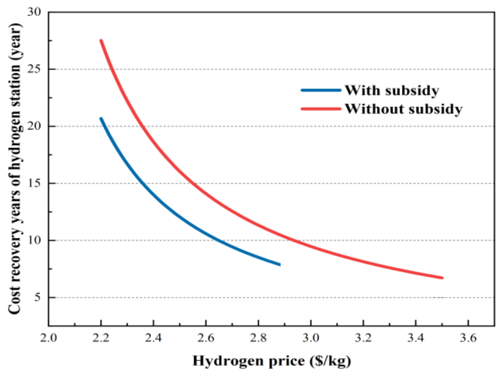

Figure 6. The cost recovery period of the H_2 station is affected by the H_2 price.

The initial construction cost of offshore hydrogen refuelling stations will decrease with the development of the technological maturity of electrolytic hydrogen production. In this scenario, when the expected cost recovery period remains unchanged, the hydrogen price of the hydrogen station is mainly affected by the initial construction cost of the hydrogen refuelling station. When the cost recovery period of a hydrogen station is 8 years (subsidies were taken into consideration), the trend of hydrogen price is shown in Figure 7.

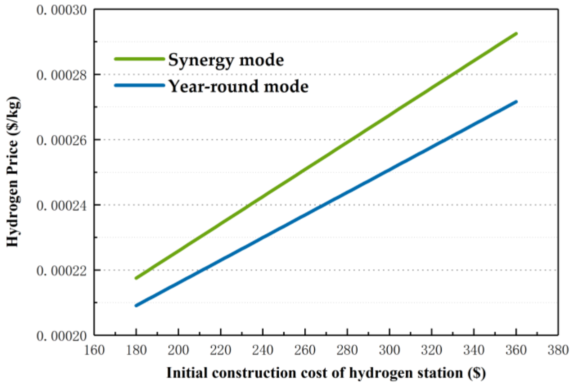

Figure 7. Hydrogen price trend of the offshore hydrogen station.

In the future, with the development of this industry, it is foreseeable that the price of hydrogen and hydrogen stations will decrease, which can effectively improve the application economy of PEMFC ships.

Changes in equipment maintenance expenses can also have an impact on the results. Due to differences in maintenance and management capabilities, when the maintenance cost of equipment fluctuates within 0.4 to 2.2 times the original value, its impact on the cost recovery period is shown in Figure 8. It can be seen that the fluctuation of maintenance expenses has a very limited impact on the offshore hydrogen station, but it is a very important issue for marine ranch investors.

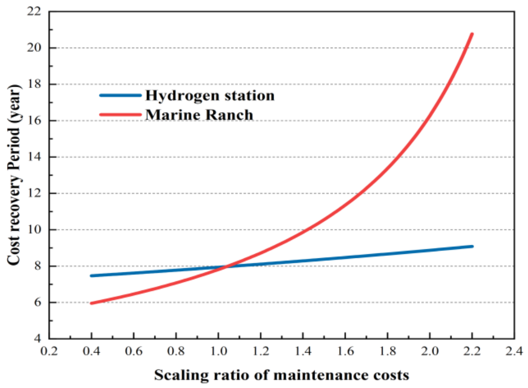

Figure 8. The impact of changes in maintenance expenses on the cost recovery period.

3.4 Promotion Scenario of the Integrated Utilization Operation Mode

In the scenario design of the integrated utilization operation mode of the hydrogen-powered ship, the size of the offshore hydrogen production and refuelling unit is relatively small, the industrial technology of each component is relatively mature, and the retrofit scheme of the hydrogen-powered ship is relatively perfect, it is suitable for further promotion as elements of a larger scale distributed design in the development and construction planning of offshore wind power and hydrogen-powered ships. In the further scenario design, four adjacent wind farm sites offshore of Liaoning province can be selected, and a hydrogen production and refuelling station with a daily hydrogen production of 1 t can be built on the platforms in their respective areas close to the offshore fishing operation area, it serves as a source of hydrogen for nearby hydrogen fuel cell powered farming breeding boats and sightseeing ships, and, as the total hydrogen supply in the area increases, it can provide enough hydrogen for more hydrogen-powered ships. Larger fishing ships such as hydrogen-powered trawlers and shrimp trawlers could also be considered. Because such ships require larger power-cell capacity, the investors would need to install 120 kW charging posts. The parameters and cost are shown in Tables 8 and 9.

Based on the above data, it can be calculated that the initial investment cost is 29.667 million $ and the annual investment is 2.283 million $, which includes annual maintenance costs (0.287 million $ per year, estimated at 1 percent of the equipment cost) and electricity consumption costs (0.0287 $/kWh, 231,500 kWh per day, 1.996 million $ per year), On the other hand, the 100 diesel vessels with the same parameters will consume about 13,025 liters of diesel per day. Based on their working duration of 300 days per year, the annual fuel cost for these ships will be about 4.362 million $. From this, we can calculate the change curve for the cost of PEMFC ships and dieselpowered ships as shown in Figure 9.

Table 8. PEMFC ship modification plan for marine ranch.

Component	Fishing Trawler	Shrimp Trawler
Speed (knots)	10	10
Length (m)	39	35
Power of fuel cell system (kW)	300	200
Power cell capacity (kWh)	600	450
Rated power (kW)	240	160
Bottle pressure (MPa)	35	35
Volume of hydrogen cylinder (L)	320	320
Number of hydrogen cylinder (L)	14	10
Hydrogen weight (kg)	91	65
Sailing duration (h)	5.7	6.1

Table 9. Cost of marine ranch PEMFC ship modification.

Costs Component (million $)	Fishing Trawler	Shrimp Trawler
Fuel cell system	0.216	0.143
Power battery system	0.129	0.097
Hydrogen storage system	0.050	0.036
Cost of accessories	0.287	0.216
Other costs	0.029	0.021
Cost of upgrading a single ship	0.711	0.513

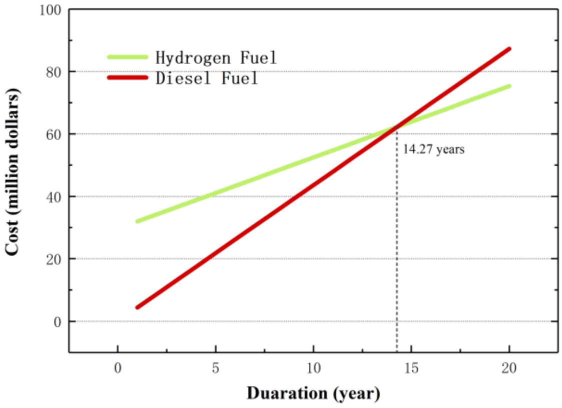

Figure 9. Cost of PEMFC ships and diesel ships.

As can be seen from this chart, the total cost of using hydrogen from offshore wind power as fuel is mainly concentrated on the initial cost, and the initial cost is very high. However, in terms of operating and maintenance costs, using hydrogen from offshore wind power as fuel has a big advantage over traditional diesel fuel. The total cost after the 15th year already has an advantage over traditional diesel fuel, and the longer it takes, the greater the advantage is.

A liter less diesel is equivalent to a 2.63 kg reduction in CO_2 emissions. This expansion would reduce CO_2 emissions by around 10,000 tonnes and sulphur dioxide emissions by 3358.4 kg per year (calculated as 0.005% sulfur content of diesel fuel).

4. Discussion

In this promotion scenario, additional passing hydrogen- powered ships could be added to it to increase demand for hydrogen, especially during the fishing off-season. This will not only make full use of the output capacity of offshore hydrogen stations to shorten the payback period for offshore wind power investors, but also create conditions for the use of more hydrogen-powered ships, and reduce fuel costs for ship owners. Furthermore, with good offshore wind power infrastructure, there are many offshore wind farms located within 100 km of each other in China, especially in the eastern and southern parts, if these wind farm investors build a chain of offshore hydrogen production and refuelling stations at reasonable intervals, they will be able to provide seamless hydrogen supply for the ships sailing along the coast, to promote the full use of renewable energy and hybrid PEMFC ships industry development. Furthermore, it should be noted that this proposed model requires nearby offshore wind farms in the sea area and the conditions to allow ships to berth and refuel. In addition, if the infrastructure construction of other alternative fuels along the coast is also relatively complete, the competitiveness of the proposed model will also be weakened.

5. Conclusions

In this paper, a demonstration scenario for the integrated utilization of offshore PEMFC ships and offshore wind power is presented, and the technical and economic analysis of this operation mode is made. It was also compared with traditional fuel ships. The following conclusions are drawn.

In this integrated application scenario, an offshore wind investor would ideally be able to recoup their investment costs in just 6.54 years and earn 0.399 million $ thereafter. Marine ranch investors can recover their costs in six to eight years, depending on the development of the sightseeing market and government subsidies for PEMFC-powered transportation.

Factors such as H2 prices, policy subsidies, and maintenance expenses all have varying degrees of impact on the results. The price of hydrogen is the most significant factor. Among other factors, the impact of policy subsidies is more evident for the offshore hydrogen station, while for investors of the marine ranch, maintenance expense is a more significant issue.

The promotion scenario can reduce CO2 emissions by around 10,000 tons per year, and SO2 emissions by 3,358.4 kg per year, and the overall cost of using hydrogen as a fuel is lower than conventional diesel fuel starting in the 15th year. However, the initial investment cost of fuel cell ships is high, and its economic benefits need to rely on policy incentives to further improve.

Author Contributions

Conceptualization, G.Y.; Methodology, G.Y. and H.W.; Software, X.L.; Validation, X.L. and B.S.; Formal analysis, X.L. and B.S.; Resources, G.Y. and H.W.; Writing—original draft preparation, X.L.; Writing—reviewing and editing, G.Y., H.W. and X.L.; Supervision, G.Y. and H.W.; Project administration, G.Y.; Funding acquisition, G.Y.

Funding

This study was supported by the Laboratory of Transport Pollution Control and Monitoring Technology (No. Z2209-030).

Acknowledgement

The authors wish to express their sincere appreciation to all participants contributing to this study. They also thank the reviewers for their constructive comments on the concept.

Conflict of Interest

The authors declare no conflicts of interest.

References

[1] Ball, M., Weeda, M., 2015. The hydrogen economy— vision or reality? International Journal of Hydrogen Energy. 40(25), 7903-7919.

[2] Han, J., Charpentier, J.F., Tang, T. (editors), 2012. State of the art of fuel cells for ship applications. 2012 IEEE International Symposium on Industrial Electronics; 2012 May 28-Mar 1; Hangzhou, China. New Yokr: IEEE. p. 1456-1461.

[3] Agyekum, E.B., Ampah, J.D., Wilberforce, T., et al., 2022. Research progress, trends, and current state of development on PEMFC-New insights from a bibliometric analysis and characteristics of two decades of research output. Membranes. 12(11), 1103.

[4] Yang, D., Tan, Y., Li, B., et al., 2022. A review of the transition region of membrane electrode assembly of proton exchange membrane fuel cells: Design, degradation, and mitigation. Membranes. 12(3), 306.

[5] Dall'Armi, C., Pivetta, D., Taccani, R., 2021. Health-conscious optimization of long-term operation for hybrid PEMFC ship propulsion systems. Energies. 14(13), 3813.

[6] Sazali, N., Wan Salleh, W.N., Jamaludin, A.S., et al., 2020. New perspectives on fuel cell technology: A brief review. Membranes. 10(5), 99.

[7] Reusser, C.A., Pérez Osses, J.R., 2021. Challenges for zero-emissions ship. Journal of Marine Science and Engineering. 9(10), 1042.

[8] Hwang, S.S., Gil, S.J., Lee, G.N., et al., 2020. Life cycle assessment of alternative ship fuels for coastal ferry operating in Republic of Korea. Journal of Marine Science and Engineering. 8(9), 660.

[9] Romano, M.C., Antonini, C., Bardow, A., et al., 2022. Comment on "How green is blue hydrogen?" Energy Science & Engineering. 10(7), 1944-1954.

[10] Lee, G.N., Kim, J.M., Jung, K.H., et al., 2022. Environmental life-cycle assessment of eco-friendly alternative ship fuels (MGO, LNG, and hydrogen) for 170 GT nearshore ferry. Journal of Marine Science and Engineering. 10(6), 755.

[11] Yu, M., Wang, K., Vredenburg, H., 2021. Insights into low-carbon hydrogen production methods: Green, blue and aqua hydrogen. International Journal of Hydrogen Energy. 46(41), 21261-21273.

[12] Chi, Y., Liang, W., Zhang, Z., et al., 2016. An overview on key technologies regarding power transmission and grid integration of large scale offshore wind power. Proceedings of the CSEE. 36(14), 3758-3771.

[13] Zhang, G., Wan, X., 2014. A wind-hydrogen energy storage system model for massive wind energy curtailment. International Journal of Hydrogen Energy. 39(3), 1243-1252.

[14] Wiser, R., Bolinger, M., Heath, G., et al., 2016. Long-term implications of sustained wind power growth in the United States: Potential benefits and secondary impacts. Applied Energy. 179, 146-158.

[15] Fang, R., 2019. Life cycle cost assessment of wind power-hydrogen coupled integrated energy system. International Journal of Hydrogen Energy. 44(56), 29399-29408.

[16] Fernández-Guillamón, A., Das, K., Cutululis, N.A., et al., 2019. Offshore wind power integration into future power systems: Overview and trends. Journal of Marine Science and Engineering. 7(11), 399.

[17] Li, Z., Guo, P., Han, R., et al., 2019. Current status and development trend of wind power generation-based hydrogen production technology. Energy Exploration & Exploitation. 37(1), 5-25.

[18] Qi, J., Zhang, W., Cao, R., 2018. Solar-to-hydrogen energy conversion based on water splitting. Advanced Energy Materials. 8(5), 1701620.

[19] Zhang, G., Wan, X., 2014. A wind-hydrogen energy storage system model for massive wind energy curtailment. International Journal of Hydrogen Energy. 39(3), 1243-1252.

[20] Deng, Z., Jiang, Y., 2020. Optimal sizing of wind-hydrogen system considering hydrogen demand and trading modes. International Journal of Hydrogen Energy. 45(20), 11527-11537.

[21] Leahy, P., McKeogh, E., Murphy, J., et al., 2021. Development of a viability assessment model for hydrogen production from dedicated offshore wind farms. international Journal of Hydrogen Energy. 46(48), 24620-24631.

[22] Calderón, M., Calderón, A.J., Ramiro, A., et al., 2013. Some comments to the paper Energy, exergy and sustainability analyses of hybrid renewable energy based hydrogen and electricity production and storage systems: Modeling and case study. Applied Thermal Engineering. 58(1-2), 261-263.

[23] Aiche-Hamane, L., Belhamel, M., Benyoucef, B., et al., 2009. Feasibility study of hydrogen production from wind power in the region of Ghardaia. International Journal of Hydrogen Energy. 34(11), 4947- 4952.

[24] Luo, Z., Wang, X., Wen, H., et al., 2022. Hydrogen production from offshore wind power in South China. International Journal of Hydrogen Energy. 47(58), 24558-24568.

[25] Li, X., Yuan, L., 2022. Development status and suggestions of hydrogen production technology by offshore wind power. Power Generation Technology. 43(2), 198-206.

[26] Wu, Y., Liu, F., Wu, J., et al., 2022. Barrier identification and analysis framework to the development of offshore wind-to-hydrogen projects. Energy. 239, 122077.

[27] Global Offshore Wind Report 2021 [Internet]. Global Wind Energy Council; 2021. Available from: https://gwec.net/wp-content/uploads/2021/09/GWEC-Global-Offshore-Wind-Report-2021.pdf

[28] Wang, Z., Wang, D., Zhao, F., et al., 2022. Hydrogen refueling stations and carbon emission reduction of coastal expressways: A deployment model and multi-scenario analysis. Journal of Marine Science and Engineering. 10(7), 992.

[29] Siyal, S.H., Mentis, D., Howells, M., 2015. Econom-

ic analysis of standalone wind-powered hydrogen refueling stations for road transport at selected sites in Sweden. International Journal of Hydrogen Energy. 40(32), 9855-9865.

[30] Martin, K.B., Grasman, S.E., 2009. An assessment of wind-hydrogen systems for light duty vehicles. International Journal of Hydrogen Energy. 34(16), 6581- 6588.

[31] Shi, J., Zhu, Y., Feng, Y., et al., 2023. A prompt decarbonization pathway for shipping: Green hydrogen, ammonia, and methanol production and utilization in marine engines. Atmosphere. 14(3), 584.

[32] Nachtane, M., Tarfaoui, M., Abichou, M.A., et al., 2023. An overview of the recent advances in composite materials and artificial intelligence for hydrogen storage vessels design. Journal of Composites Science. 7(3), 119.

Sustainable Marine Structures
https://journals.nasspublishing.com/index.php/sms

ARTICLE

Design Basis Considerations for the Design of Floating Offshore Wind Turbines

Ove Tobias Gudmestad[1,2*] **Anja Schnepf**[2,3]

1. Department of Marine Science, Western Norway University of Applied Science, Haugesund, 5528, Norway
2. Department of Mechanical and Structural Engineering and Material Science, University of Stavanger, Stavanger, 4021, Norway
3. CoreMarine AS, Stavanger, 4014, Norway

ARTICLE INFO

Article history
Received: 30 July 2023
Revised: 25 August 2023
Accepted: 5 September 2023
Published Online: 16 September 2023

Keywords:
Safety level
Wave conditions
Current conditions
Soil conditions
Transformer stations
Insurance
Costs for wind turbine projects

ABSTRACT

The wind farm owner/operator must prepare a Design Basis to facilitate the design of floating offshore wind turbines. The Design Basis is crucial to ensure that the individual elements of the wind farm are designed according to the relevant standards and the actual site conditions. In case of under-design, systematic failures can occur across the wind turbines, which can result in progressive damage to the turbines of the wind farm. This paper focuses on the safety and overall economics, including limiting potential excessive costs of heavy maintenance caused by damage due to under-design. Thus, this paper highlights critical aspects of particular importance to be implemented in the Design Basis document. Meeting all required constraints for developing offshore wind farms in deep water may result in higher costs than initially anticipated. Nonetheless, a realistic cost estimation for all phases of the project, engineering, construction, transport, and installation on site, remains essential for all engineering projects, including those involving renewable energy.

1. Introduction

Every facility development project undergoes an engineering phase and needs a Design Basis to be executed. The Design Basis document sets the framework for the project, as it contains the essential requirements and information regarding important parameters for the design, fabrication, installation, and operation phases of the facilities.

The Design Basis lists the selection of standards in every project. DNV [1] provides a comprehensible review of applicable standards, noting that the IEC 61400 series of standards [2] represents the de facto international standards for offshore wind turbines. Furthermore, standards specifically needed for the project must be listed. These requirements also include the selection of safety levels for

---

*Corresponding Author:
Ove Tobias Gudmestad,
Department of Marine Science, Western Norway University of Applied Science, Haugesund, 5528, Norway; Department of Mechanical and Structural Engineering and Material Science, University of Stavanger, Stavanger, 4021, Norway;
Email: otgudmestad@gmail.com

DOI: http://dx.doi.org/10.36956/sms.v5i2.913

the design related to safety for personnel during all phases of the project, the physical environment, and the robustness of the facilities to damage and collapse.

Furthermore, the Design Basis provides information regarding the design environmental loading in line with the selected safety level. For instance, it covers the wind, current, and wave conditions related to the selected annual exceedance probability. Additionally, the conditions of the sea floor on which the facilities are to be placed are essential information. Failing to properly assess it before commencing detailed engineering can lead to substantial cost overruns or huge damages during operations. Likewise, carefully selecting materials for the facilities is critical, as improper use of materials can quickly lead to wear and tear, corrosion, and subsequent damage. It has also recently become essential to specify all emissions from all types of facilities during their entire lifetime to gain governmental approval for the start-up of operations. The use of equipment or processes that produce toxic waste or could lead to large pollution if emitted into water or air shall be limited.

Critical design parameters for offshore wind turbines must *not be underestimated* to obtain a successful project. As the operator has to install several wind turbines in a wind farm to obtain acceptable profit from the project, a systematic failure could lead to the collapse of several wind turbines in a wind farm in a chain reaction. Selecting a Design Basis that represents an under-design could thus involve many (or all) turbines, potentially leading to irreparable damage to the wind farm.

2. The Design Basis for Floating Offshore Wind Turbines

Considerable efforts have been made to develop safe and efficient floating offshore wind turbines suitable for water depths exceeding the economic limit of fixed monopile or jacket-supported wind turbines [3,4]. Technologies applicable to such wind turbines have been developed; for example, Yang et al. [5] presented a thorough summary of commissioned floating offshore wind projects and their mooring systems, showing the versatility of the currently applied concepts. International standards [2] have been developed to ensure wind turbines are designed according to sound engineering principles.

The success of an actual wind turbine depends on its design being suitable for the *actual site conditions*. Therefore, a proper design basis must be developed by the owner and operator of all wind turbines in the entire wind farm and for the substation carrying transformers (if required).

The Design Basis for floating offshore wind turbines must cover all elements required for the fabrication, installation, and operation phases of the facilities. In recent years, the authorities have also required the Design Basis for projects to include a plan for abandonment and removal of the facilities after their intended use.

Even though authorities and operators may promote wind farm projects, a realistic attitude to costs must be the basis for decisions. The Design Basis is a document that sets the technical requirements, and the reality regarding the design conditions might disappoint the most optimistic developers. The oil and gas company Equinor announced in 2022 [6] that a wind farm is planned in the central North Sea to provide electrification of the Troll field; see Figure 1. The electricity generated was to replace the gas turbines mounted on the production platforms. One year later, Equinor announced [7] that technology was not sufficiently mature, and costs were higher than initially calculated. Therefore, the company decided to put the wind farm project at Troll on hold.

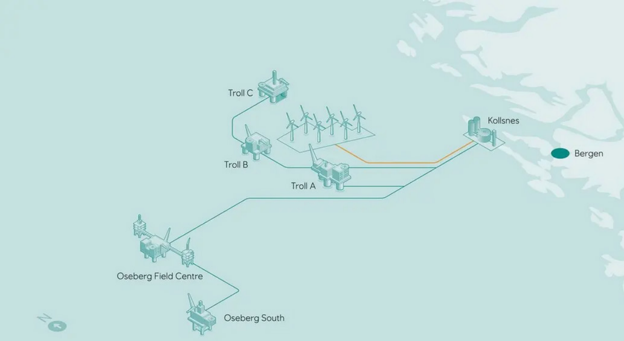

Figure 1. The planned Troll wind farm project that is put on hold, Equinor’s website.

Source: Equinor Put Trollvind on Hold[7].

3. Discussion of Critical Parameters of the Design Basis

3.1 Safety Levels for the Design of Floating Offshore Wind Turbine Farms

The national authorities give the safety levels for the design of offshore wind turbines and offshore substations (transformer stations), generally building on international standards. It might be noted [8] that “for marine structures in the *offshore wind* engineering business, lower safety levels than in the oil and gas industry are specified by international standards. The set of design requirements provided by the International Electrotechnical Commission (IEC); IEC 61400 [2] ensures, however, that wind turbines are appropriately engineered against damage from hazards within the planned lifetime". One can, however, question whether the annual probability of exceedance of the environmental loading should be set to 10^{-2}, like for the oil and gas industry [9], since floating offshore wind turbines represent large investments and extreme environmental effects at present seem to occur more frequently due to ongoing climate changes. On the other hand, some authors claim that the offshore wind industry might better not adapt to the oil and gas standards, see Griffith et al. [10]. Further work is recommended to clarify the issue of how to obtain an adequate safety level in the offshore wind industry.

"It should be noted, however, that wind farms will require transformer stations, which from time to time must be manned. These substations have a considerable volume of toxic transformer oil for cooling the transformers and represent large investments. The safety level selected for the design of these substations will depend on the consequences of failure to, or loss of the stations [8]." Related to this, the actual safety level is determined by the selection of the annual probability exceedance of the environmental data and the selection of partial coefficients.

3.2 Information about the Soil Conditions at the Offshore Site

The soil conditions at the offshore site determine the design of the anchor system. For instance, in certain areas in the Norwegian Trench, the soil conditions are relatively homogeneous and consist of soft clays. In this case, an anchor system based on suction piles connected to the mooring lines can be considered. Collecting information about the soil conditions where anchors are to be placed is necessary in areas with local soil variations. In onshore projects, disputes regarding actual soil conditions often cause project cost overruns, and there should be no excuse to skip details regarding the soil conditions in the Design Basis for offshore floating wind turbines.

3.3 Data Regarding the Physical Environment

The physical environment leads to loads on built facilities. Offshore, the wind, wave, and current conditions represent large loads, and wind turbines placed offshore must be designed to resist the associated load effects. Other loads caused by snow and ice (atmospheric ice on the turbine blades and sea spray ice on the floater) must also be considered where relevant. The NORSOK N-003 standard [11] summarizes offshore actions and action effects, stating that the wind turbines must be designed to resist the loads expected for the specified annual probability of exceedance. The Design Basis must reflect the measured environmental data; however, data collection takes a long time, and available databases must be used. With the ongoing climate change, extreme weather is expected to occur more frequently than in the past. Data from databases going back in time should be considered. This should be done to consider especially extreme events adequately. Sufficient measurements of environmental conditions might be absent in areas without oil and gas developments, for example, close to the Norwegian coast. When there is a lack of sufficient measured data for environmental conditions, alternative methods should be sought to obtain physical environmental data that approximates the actual situation to reduce design risks. This may include using measurements from similar areas, simulation techniques, or other suitable methods. Additionally, it must be clear how these methods are used and referenced to effectively obtain the environmental conditions of the operating area.

Wave Conditions at the Offshore Site

The wave conditions in the North Sea and many locations worldwide are well known, and considerable databases exist. Using data about meteorological low-pressure situations and measured wave information, it should also be possible by the method of "wave hindcasting" to prepare statistics about wave conditions at most sites where offshore floating wind turbines are considered. For the Norwegian shelf, the recommendations given by NORSOK N-003 [11] for an annual probability of exceedance of 10^{-2} can be used; see Figures 2 and 3. However, the standards for offshore wind turbine design [1,2] require a design to resist environmental loading for an annual probability of exceedance of 2×10^{-2}. This means a 50-year return design wave is used for offshore wind projects rather than a 100-year return design wave that would have been applied in the oil and gas industry.

Currents at the Offshore Site

It is essential to identify the design of near-surface-current at the site where offshore wind turbines are going to be installed, as these turbines have relatively large near-surface volumes to secure sufficient buoyancy and volume for ballast (to act against tall turbines in order to secure initial stability). The forces on the anchor system might be tremendous in case of strong currents in combination with relevant wave-particle motions.

For wind turbines placed near the Norwegian coast, say within 60 to 100 km from the coast, it should be noted that The Norwegian Coastal Current (NCC) can be extremely strong. During intense northerly storms, a storm surge is created in the Southern North Sea, Skagerrak, Kattegat, and even the Baltic Sea. When the storm settles, water flows back north and can considerably enhance the NCC. Figure 4 shows coastal current whirls (eddies) on 13 April 1981 [12]. The near-surface whirls (eddies) are created as the northern flow of water becomes unstable; see also Figure 5 [13].

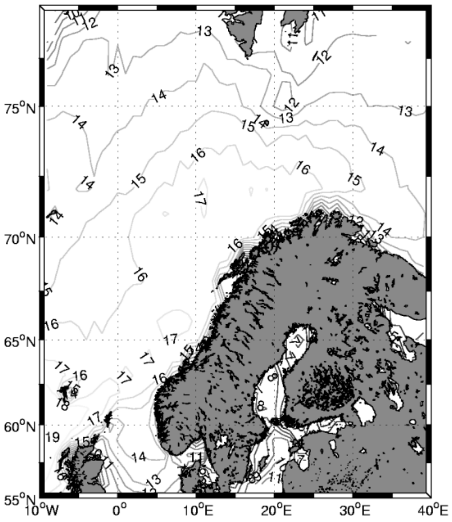

Figure 2. Significant wave height contours based on NORA10 1958-2011, corresponding to an annual exceedance probability of 10^{-2}, NORSOK.

Source: NORSOK Standard N-003 Actions and Actions Effects [11].

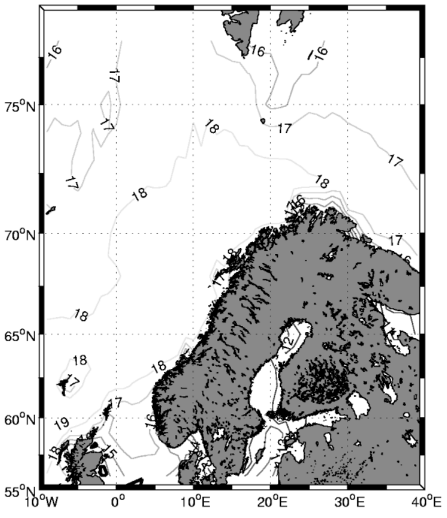

Figure 3. Spectral peak period associated with 10^{-2} annual probability significant wave height H_s: $T_p = a\cdot(1.0+H_s)^{(0.33+0.0029\cdot HS)}$, $a = 5.8$ at N55° linear increasing to 6.6 at N78°, NORSOK.

Source: NORSOK Standard N-003 Actions and Actions Effects [11].

The Troll oil and gas field is located 65 km west of Bergen in the Northern North Sea at 60°38’44”N 3°43’35”E/60.645556°N 3.726389°E and is influenced by whirls (eddies) which expand westwards from the NCC. The water depth exceeds 300 m across the field. During the drilling of wells in the spring of 1981, there was one specific situation when very strong eddy currents occurred. The drilling rig was about to drift off location, and there were concerns that the anchor system would not hold. Supply vessels had to be linked to the rig to keep the rig in position. That was successfully done; however, an extensive research project was initiated after the event to identify the cause of the strong currents and realistic extreme values. Much of this research work was carried out at Sintef, Trondheim, under the leadership of McClimans [14,15]. The surface currents were studied in the laboratory and by numerical models to support a field measurement program. “Large bursts of coastal water with surface currents over 3 knots were observed far offshore. Laboratory studies of the dynamics of coastal currents off the west coast of Norway revealed large mesoscale eddies at an annual probability of exceedance of 10^{-2} [15].” Other locations along the Norwegian coast have also been considered by Saetre [16]. For the Troll location, the design of the current value (with an annual exceedance probability of 10^{-2}) is given in Figure 6.

One could question whether estimating this high value of the design current is correct based on one specific event and very few measurements. The argument is, however, that this value has been estimated from actual extreme data, and it is relevant to select a design basis with reference to actual events. The standard for selecting actions and action effects for oil and gas installations on the Norwegian shelf [11] requires measurements at the site to use lower values for the current; see Figure 7. For the design of offshore wind turbines, careful selection of design current values must be carried out to ensure that the mooring system can keep the wind turbines on location. It should be noted that the extreme value of the current may not be combined with the maximum waves, as extreme currents occur after a storm event, following the backflow of water after the storm surge.

Furthermore, the design value of the current will influence the design of the electric cables between the individual wind turbines [17,18] and the transformer station [19], where the electricity generated by the wind turbines is transformed from alternating current (AC) to direct current (DC) to limit energy loss during transport to shore. Functioning cables are crucial for the profit of a wind farm, and the risk of damage must be minimized. That is important to consider in the design, as repair works on cables can often only be carried out in small weather windows, meaning the wind turbines might be disconnected from the electricity grid over several months [20].

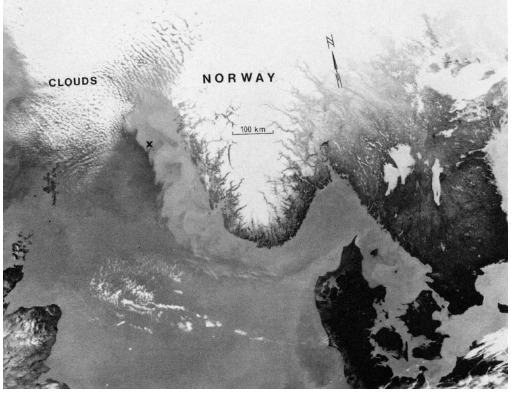

Figure 4. Satellite thermal image of coastal whirls (eddies) on 13 April 1981, McClimans and Lønseth.

Source: McClimans, T.A., Lønseth, L. [12].

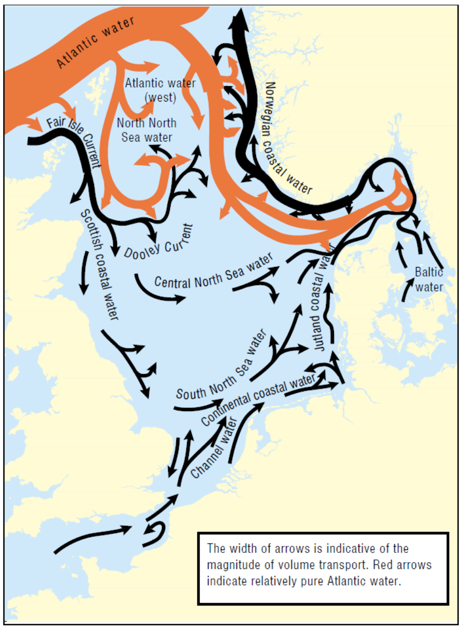

The width of arrows is indicative of the magnitude of volume transport. Red arrows indicate relatively pure Atlantic water.

Figure 5. The general current circulation system of the North Sea, OSPAR.

Source: Quality Status Report 2000 Region II Greater North Sea [13].

Wind Conditions at the Offshore Site

In the actual marine environment, wind loads mainly come from the cyclic loads of the turbine. The economic viability of different wind fields needs to be demonstrated. The unbalanced wind load on the upper part of the tower poses a challenge to the control of the nacelle. Furthermore, there is a fire and mechanical failure risk, which requires additional analysis and description.

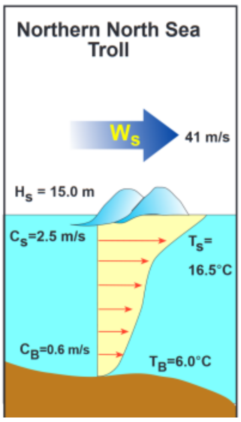

Figure 6. Design current suggested for the Troll field; C_S = surface current, C_B = bottom current, T represents the max. temperatures in the water column; note that the water depth is 300 m, Saetre.

Source: Saetre, H.J. [16].

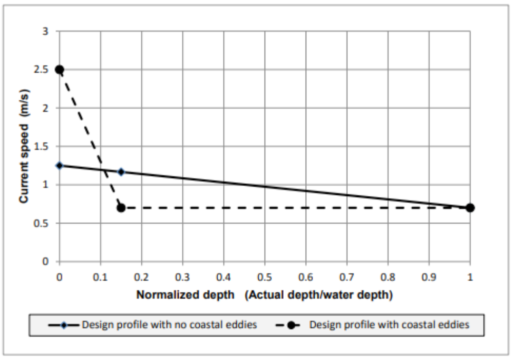

Figure 7. Preliminary total current profiles for cases when no current data is available, NORSOK.

Source: NORSOK Standard N-003 Actions and Actions Effects [11].

Ice Conditions at the Offshore Site

The presence of ice and ice sheets represents special consideration for certain areas. The floating wind turbine structures can fail under compression from the ice [21]. In some areas (e.g., in the Baltic Sea and Bohai Bay), the bottom fixed wind turbines are designed to resist these loads, and the reference is usually ISO 19906 [22]. For floating wind turbines, the potential presence of ice can represent a "no-go" whereby no floating wind turbines should be installed in the area. Ice management can be considered in the case of light ice conditions. It should be noted that vessels in ice are designed to turn up against the ice drift; this might not be possible for floating wind turbines.

Conditions of the Physical Environment at the Fabrication Site

When the fabrication site has been selected for the wind turbines, it is of utmost importance that the environmental conditions at the fabrication site are known to ensure that the design for fabrication considers the soil conditions as well as the wind, wave, current, and bathymetry at the site. While it is expected that most of the needed data is easily available, strong winds occurring during the fabrication period may cause damage and even lead to fatalities. Furthermore, the wind turbines may be moored near the fabrication dock before the float-out to the offshore site. The mooring system during fabrication must be designed for the actual conditions. The selection of safety level includes the selection of the return period for wind and wave conditions at the fabrication site and is critical. With changing climatic conditions, extreme weather is occurring more frequently, and safety during fabrication must be considered appropriately.

It should be noted that all countries will endeavour to fabricate wind turbines at local fabrication sites [23]. This can be seen as the biggest risk in the supply chain [24]. Concepts requiring wide fabrication yards will be excluded from most shipyards. The bathymetry at the construction site and along the tow-out channel to the offshore site will largely influence the concept selection. Restrictions will favor concepts that do not need a deep draft. Due to this, the deep-draft Hywind will not be given priority when operators are selecting a wind turbine concept that can be partly fabricated in drydocks and be finalized inshore in shallow waters, ready to be towed to the site with tower, nacelle, and turbine blades installed.

3.4 Use of Toxic Fluids in Wind Farm Transformers

A wind farm consisting of many individual wind turbines will generate large quantities of electricity. In order to efficiently transport the electric current to the users, the (AC) generated must be transferred to the (DC). Separate transformer stations must be installed. The wind turbines are connected to a transformer station by electric cables hanging between the wind turbines. The cables are made buoyant using buoyancy elements or routed along the seafloor. These cables will severely restrict fishing activities in the area; note that the mooring system will also do so. The transformer stations contain a significant volume of oil, up to 50 m^3 [25], for cooling the transformer. As transformer oil is generally very toxic, the pollution from the collapse of a transformer station is non-negligible. The design basis for the transformer stations must consider this fact [19]. A requirement that the mooring system shall be redundant is relevant. It is also suggested that efforts must focus on using less toxic transformer fluid or developing transformers that can better handle the heat generated through the electricity transformation from AC to DC [26].

4. Need for Adequate Insurance Cover

As wind farm operators are not necessarily organizations with large funds and may struggle to repair their assets, there is a need for proper insurance to protect the public from having to take over a malfunctioning offshore wind farm project. For onshore wind farms, the numerous failures can generally be classified as individual failures rather than systematic failures. However, there is a tendency for the gear systems to be weak, and the blades of offshore wind turbines deteriorate faster than expected [27].

For offshore wind turbines, a failure in the grouting system between the foundation and the tower has been of much concern and has caused much repair work [28]. The floating wind turbines are individually more expensive than fixed wind turbines, and a systematic error or under-design for a complete wind farm may lead to bankruptcy of the farm. Such an error can easily be caused by the collision of a drifting ship with a floating wind turbine resulting in progressive drifts throughout the entire farm [29]. For a discussion of using shared or four mooring lines to provide redundancy see Hall et al. [30].

It is, therefore, suggested that the authorities require offshore floating wind farm projects to have proper insurance to handle situations with major damage to wind turbines in the wind farm. Such a requirement will lead to the need for external verification by a warranty surveying company in all project phases to ensure that the facilities are built, installed, and operated according to specifications, the established Design Basis, and sound engineering and operational principles, like in the offshore oil and gas industry. For a full review of North Sea environmental conditions see Quante et al. [31]. The costs of insurance coverage throughout the lifetime of the floating offshore wind parks will be noticeable. However, if a company cannot afford safety, the company might have to face the costs of accidents. In civil society, insurance is required when the potential economic loss exceeds the funds of the owner. All cars must, for example, have third-party damage insurance coverage referring to their license plates, as the costs of collisions with potential personnel injury can be exceptionally high, outside the range where individuals can pay the compensation set by the juridical system.

5. Safety for Personnel Involved in the Fabrication, Installation, and Operation of Floating Offshore Wind Turbines

In addition to the structure itself, personnel safety and risks involved in the construction process are critical factors to consider for the overall operational cost of floating wind turbines. Ensuring personnel safety should be reflected throughout the entire construction and operation processes. The safety risk during the construction period should follow industry standards that are set in the offshore construction industry.

The safety of everyone involved in the operations of floating offshore wind turbines, including access for maintenance and repair, must be ensured [32,33]. The theme is highly relevant as the activities involve transfer from the ship to the wind turbine, a transfer between two moving objects often in conditions where the personnel transport vessel has considerable movements in waves [34]. A complete Design Basis will have to ensure that personnel safety is incorporated in the design of all wind farm facilities.

6. Construction Management and Installation Risk

Efficient construction management is key to the success of all construction projects. The process for a well-planned project emphasizes a detailed FEED (Front End Engineering Design) document, rigorous cost control, relevant standards and clear contracts, and company attendance at the construction site. Following the COVID-19 pandemic, some construction material has come in high demand that cannot be supplied as quickly as before, causing project delays and cost overrun. In the long term, construction and operational experience are expected to contribute significantly to reducing the levelized cost of energy (LCOE) of floating offshore wind farms [24].

Insurance companies and warranty surveyors must be involved to ensure acceptable risks during towing and installation. The consequence of carefully planned and executed installation activities might be "waiting on the weather" to carry out the marine operations. The probability of waiting for adequate weather will influence the towing and installation costs, and the marine operations must be carefully designed and planned to avoid excessive cost escalations during towing and installation.

7. Discussion and Conclusions

A discussion on the necessity to prepare a proper Design Basis for floating offshore wind turbines has been presented. The focus has been on selecting relevant standards and values of the environmental data to be used for the design. Unless safe values are selected, there is a high probability that wind turbines can be damaged during extreme weather events. Furthermore, it is emphasized that soil data for mooring system design must be available.

The findings imply that developing offshore wind farms in deep waters might increase costs. At the same time, the probabilities of damages or failures can be reduced.

The principal findings of the paper can be summarized as follows:

- The selection of data for environmental loading should be reviewed with a discussion of whether data with an annual probability of exceedance of 10^{-2} should be used, as for the oil and gas industry. The argument is that the costs of floating offshore wind turbines are very high, and under-design might involve the failure of many or all turbines in a wind farm.
- The current at the site is a major unknown, and efforts must be made to identify the value of the design current. The statistical database for selecting extreme current values may not be sufficient, and separate data collection or laboratory modeling may be necessary. The problem is, however, that extreme design currents occur very infrequently. It might be necessary to consult data archives to identify realistic values. Selecting the combination of extremely strong currents and large waves can also be necessary to design the mooring and electrical cable systems.
- The central electricity transformer station of a wind farm represents a non-negligible environmental pollution risk. Efforts should be made to reduce this risk, either by designing the transformer station to a high safety standard to reduce the probability of pollution or to reduce the volume of toxic transformer oil to minimize the consequences of an oil spill. Offshore wind farms should be prepared for oil spill clean-up operations.
- The repair costs of damaged wind turbines in a wind farm might exceed the financial capabilities of the owner of the facilities. It is suggested that insurance coverage should be mandatory to ensure that the authorities do not have to take over the responsibility to repair or remove the damaged turbines.
- The wind turbine operators shall be prepared to bear the costs of abandoning the wind farm and removing all facilities at the location.
- Given the above findings and conclusions, research efforts are recommended concerning the following:
- A review of the selection of safety levels for offshore floating wind turbines and all equipment installed in a wind farm should be conducted. That will also include robust mooring design and selection of mooring line redundancy requirements.
- Data evaluation projects related to identifying real-

istic values for the current are recommended for all areas opened by authorities for the development of floating offshore wind farms.

- A project should be carried out to ensure the safety of all involved in the operations of floating offshore wind turbines, including access for maintenance and repair.

Author Contributions

The first author prepared the first draft of the paper. The second author contributed with discussions of the topics and a thorough document review.

Funding

The first author was supported in parts by funds provided by "The Program for Maritim Competence (MARKOM II)", (https://www.markomii.no/om-markom-ii/), project 10031; funds made available to Western Norway University of Applied Science, Haugesund, Norway. The second author received funding from CoreMarine AS and The Research Council of Norway, project 320902, while studying for a Ph.D. at the University of Stavanger.

Acknowledgement

The first author appreciates discussions with colleagues from Multiconsult, Tromsø, Norway, prior to the preparation of the paper.

Conflict of Interest

The authors declare no conflict of interest.

References

[1] Overview of Offshore Wind Standards and Certification Requirements in Selected Countries [Internet]. Available from: https://www.norskindustri.no/siteassets/dokumenter/rapporter-og-brosjyrer/leveransemodeller-havvind/dnv-gl-report_overview-of-offshore-wind-standard-and-certification-requirements_final_11.12.2020_not-signed.pdf

[2] IEC 61400-1: 2019 Wind Energy Generating Systems—Part 1: Design Requirements [Internet]. Available from: https://webstore.iec.ch/publication/26423

[3] Skaare, B. (editor), 2017. Development of the Hywind concept. ASME 2017 36th International Conference on Ocean, Offshore and Arctic Engineering; 2017 Jun 25-30; Trondheim, Norway. DOI: https://doi.org/10.1115/OMAE2017-62710

[4] Thiagarajan, K.P., Dagher, H.J., 2014. A review of floating platform concepts for offshore wind energy generation. Journal of Offshore Mechanics and Arctic Engineering. 136(2), 020903.

[5] Yang, R., Zheng, X., Chen, J., et al., 2022. Current status and future trends for mooring systems of floating offshore wind turbines. Sustainable Marine Structures. 4(2). DOI: http://dx.doi.org/10.36956/sms.v4i2.617

[6] Equinor and Partners Consider 1 GW Offshore Wind Farm off the Coast of Western Norway [Internet] [cited 2023 Jul 26]. Available from: https://www.equinor.com/news/20220617-considering-1gw-offshore-wind-farm-off-western-norway

[7] Equinor Put Trollvind on Hold [Internet] [cited 2023 Jul 26]. Available from: https://www.equinor.com/news/20230522-trollvind-on-hold

[8] Gudmestad, O.T., 2023. Selection of safety level for marine structures. Procedia Structural Integrity. 48, 113-118.

[9] ISO 19900:2019 Petroleum and Natural Gas Industries—General Requirements for Offshore Structures [Internet]. Available from: https://www.iso.org/standard/69761.html

[10] Griffiths, T., Draper, S., Cheng, L., et al., 2023. The offshore renewables industry may be better served by new bespoke design guidelines than by automatic adoption of recommended practices developed for oil and gas infrastructure: A recommendation illustrated by subsea cable design. Frontiers in Marine Science. 10, 1030665. DOI: https://doi.org/10.3389/fmars.2023.1030665

[11] NORSOK Standard N-003 Actions and Actions Effects [Internet]. Available from: https://silo.tips/download/norsok-standard-n-003

[12] McClimans, T.A., Lønseth, L., 1985. Oscillations of frontal currents. Continental Shelf Research. 4(6), 699-707. DOI: https://doi.org/10.1016/0278-4343(85)90037-8

[13] Quality Status Report 2000 Region II Greater North Sea [Internet] [cited 2023 Jul 26]. Available from: https://qsr2010.ospar.org/media/assessments/QSR_2000_Region_II.pdf

[14] McClimans, T.A., Nilsen, J.H., 1982. Whirls in the Norwegian coastal current. Coastal oceanography. Springer Science + Business Media, LLC.: Berlin. pp. 311-320.

[15] Carstens, T., McClimans, T.A., Nilsen, J.H., 1984. Satellite imagery of boundary currents. Elsevier Oceanography Series. 38, 235-256. DOI: https://doi.org/10.1016/S0422-9894(08)70614-7

[16] Saetre, H.J. (editor), 1998. Acquisition of critical metocean data on the Norwegian deepwater frontier. Offshore Technology Conference; 1999 May 3-6;

Houston, Texas.
DOI: https://doi.org/10.4043/10746-MS

[17] Schnepf, A., Devulder, A., Johnson, Ø., et al., 2023. Numerical investigations on suspended power cable configurations for floating offshore wind turbines in deep water powering an FPSO. Journal of Offshore Mechanics and Arctic Engineering. 145(3), 030904.
DOI: https://doi.org/10.1115/1.4057006

[18] Schnepf, A., Giljarhus, K.E.T., Johnsen, Ø., et al. (editors), 2023. Dynamic power cable configuration design for floating offshore wind turbines using gradient-based optimization. Proceedings of the ASME 2023 42nd International Conference on Ocean, Offshore and Arctic Engineering OMAE2023. 2023 Jun 11-16; Melbourne, Australia.
DOI: https://doi.org/10.31224/3219

[19] DNV-ST-0145 Offshore Substations [Internet]. Available from: https://www.dnv.com/energy/standards-guidelines/dnv-st-0145-offshore-substations.html

[20] Ishii M., Ueda E., Utsunomiya T., et al., 2018. Floating offshore wind power generation system of the coast of Fukushima. Demonstration research project. Main summary report. Available from: https://www.enecho.meti.go.jp/category/saving_and_new/new/information/180824a/pdf/report_2018.pdf.

[21] Barooni, M., Ashuri, T., Velioglu Sogut, D., et al., 2022. Floating offshore wind turbines: Current status and future prospects. Energies. 16(1), 2.
DOI: https://doi.org/10.3390/en16010002

[22] ISO 19906:2019 Petroleum and Natural Gas Industries—Arctic Offshore Structures [Internet]. Available from: https://www.iso.org/standard/65477.html

[23] Re, P., Passoni, G., Gudmestad, O.T., 2019. Mooring systems analysis of floating wind turbines in Italian seas. IOP Conference Series: Materials Science and Engineering. 700(1), 012002.
DOI: https://doi.org/10.1088/1757-899X/700/1/012002

[24] Floating Wind: Turning Ambition into Action [Internet]. DNV; 2023. Available from: https://www.dnv.com/focus-areas/floating-offshorewind/floating-wind-turning-ambition-into-action.html

[25] The Ultimate FAQs Guide to 100 MVA Transformer [Internet] [cited 2023 Jul 26]. Available from: https://www.daelimtransformer.com/100-mva-transformer.html

[26] ABB Lowers Environmental Impact of High-voltage Transformers [Internet] [cited 2023 Jul 26]. Available from: https://new.abb.com/news/detail/49379/abb-lowers-environmental-impact-of-high-voltage-transformers

[27] Kavakli, M., Gudmestad, O.T., 2023. Analysis and assessment of onshore and offshore wind turbines failures. International Journal of Energy Production and Management. 8(1), 45-59.

[28] Lotsberg, I., 2013. Structural mechanics for design of grouted connections in monopile wind turbine structures. Marine Structures. 32, 113-135.

[29] Hirokawa, E., Suzuki, H., Hirabayashi, S., et al. (editors), 2015. Estimation of risk of progressive drifts in a wind farm caused by collision of drift ship. ASME 2015 34th International Conference on Ocean, Offshore and Arctic Engineering; 2015 May 31-Jun 5; St. John's, Newfoundland, Canada.
DOI: https://doi.org/10.1115/OMAE2015-41473

[30] Hall, M., Lozon, E., Housner, S., et al., 2022. Design and analysis of a ten-turbine floating wind farm with shared mooring lines. Journal of Physics: Conference Series. 2362(1), 012016.
DOI: https://doi.org/10.1088/1742-6596/2362/1/012016

[31] Quante, M., Colijn, F., Bakker, J.P., et al.. 2016. North sea region climate change assessment. Introduction to the assessment—Characteristics of the region. Springer: Berlin. pp. 1-52.

[32] Craig, B., 2022. Offshore Wind Turbines: Managing the Safety Risks [Internet] [cited 2023 Jul 26]. Available from: https://www.britsafe.org/publications/safety-management-magazine/safety-management-magazine/2022/offshore-wind-turbines-managing-the-safety-risks/

[33] Oversikt over hvordan helse- arbeidsmiljø- ogSikkerhets-regelverket (HMS-regelverket) for vindkraft er innrettet på land i Norge og for havvind i Danmark og Storbritannia (UK). Anbefaling om hvordan HMS-regelverket for havvind bør utvikles. Stavanger, Norway (Norwegian) [Overview of how health, working environment and the safety regulations (HSE regulations) for wind power are arranged onshore in Norway and for offshore wind in Denmark and the United Kingdom (UK). Recommendation on how the HSE regulations for offshore wind should be developed] [Accessed 2023 Jul 26th]. Available from: https://offshorenorge.no/globalassets/dokumenter/drift/rapport----anbefaling-om-hvordan-hms-regelverket-for-havvind-bor-utvikles.pdf

[34] Gudmestad, O.T., Viddal, S., 2022. Personnel-transfer from vessel to offshore floating wind turbine. Trends in renewable energies offshore. CRC Press: Boca Raton.

NASS
NAN YANG ACADEMY OF SCIENCES

Sustainable Marine Structures
https://journals.nasspublishing.com/index.php/sms

EDITORIAL

Offshore Fish Farming: Challenges and Recent Advancements

Lin Li[*]

Department of Mechanical and Structural Engineering and Materials Science, University of Stavanger, Stavanger, 4021, Norway

ARTICLE INFO

Article history
Received: 5 September 2023
Accepted: 17 September 2023

The current marine-based aquaculture primarily utilizes nearshore waters by means of fish cages. Over the past few decades, enormous types of fish cages have evolved, and the technology converges to a few optimized designs of cages that balance capital costs and fish welfare. The prevailing technology for fish farming is the flexible gravity-type open-net cage, which comprises a floating collar made of high-density polyethylene (HDPE), flexible net enclosures for fish containment, a bottom ring, bottom weights, and interconnecting wires or ropes. These cages can have diameters exceeding 50 m and depths of over 20 m. A modern commercial-scale farm can consist of up to ten or more such cages, and a complex grid mooring system is required. Such a system includes bridle lines, frame lines, anchor lines and buoys. The whole system is highly flexible and resilient against exposure to wave and current forces. However, due to biofouling, wear and tear caused by environmental forces and operation, regular maintenance is needed to keep the system in good condition. Feeding is facilitated through feeding tubes, operated either from the control room aboard a barge or remotely from shore. Such fish farms are known for their cost-effectiveness and resilience, typically situated in sheltered environments, like fjords or nearshore areas.

The sustainability of nearshore aquaculture faces several critical challenges, including threats to wild stocks from fish escape, issues with parasites, water pollution, harmful algal blooms, impacts from climate change, etc. Additionally, the limited availability of sheltered locations is also a driving factor to move the aquaculture industry toward more exposed seas, notably offshore fish farming. Currently, there is no agreed definition for offshore or exposed fish farming [1]. In general terms, it refers to fish farming conducted in remote and unsheltered locations

---

*Corresponding Author:
Lin Li,
Department of Mechanical and Structural Engineering and Materials Science, University of Stavanger, Stavanger, 4021, Norway;
Email: lin.li@uis.no

DOI: http://dx.doi.org/10.36956/sms.v5i2.949

characterized by high-energy currents and waves comparable to those of the open ocean but located relatively close to the coast [2].

The potential advantages of offshore farming are significant. They include access to ample open sea space for achieving better economies of scale, reduced exposure to pollution from human-induced sources, minimized conflict with other nearshore activities, improved water exchange within the farm, better control of fish parasites, reduction in negative environmental impacts both on water quality, the substrate and associated benthic organisms, etc. However, new challenges emerge as the industry transitions to exposed locations. These challenges, owing to their complexity, are not yet clearly defined, or extensively researched. Generally, the key challenges are associated with structural design, remote operation, and ensuring fish welfare in the face of harsh environmental conditions and the remoteness of offshore sites. These result in extra costs that need to be matched by benefits in production. Addressing these challenges demands innovation in both technology and strategies to adapt current practices to effective offshore farming.

In recent years, numerous offshore fish farm concepts have been proposed, and some have been successfully constructed and deployed. A comprehensive review of these concepts can be found [1]. From a structural design perspective, the novel offshore fish farms tend to feature more rigid and robust supporting frames and submerged cages in contrast to the prevailing flexible floating cage technology. The design aims to endure the stronger wave and current loads in an offshore environment while minimizing deformation and ensuring adequate cage volume. Two prominent offshore fish farm units, namely Ocean Farm 1 and Havfarm, are the pioneering examples among various designs, and they are already in full-scale operational phases off the Norwegian coast.

Ocean Farm 1 has been considered as the first full-scale offshore fish farm operating in exposed sea since 2017. With a diameter of 110 m and a volume of 250000 m^3, the cage can accommodate over 1 million salmon. In contrast to the flexible collar cage in sheltered waters, this offshore facility is a dodecagonal semi-submersible unit composed of a rigid frame structure with steel columns, pontoons, and braces to resist excessive environmental loads. Stiff net materials are attached to the frame structure to minimize cage deformation. The design significant wave height for such a structure is about 5 m and the design current velocity is 0.75 m/s [3].

Havfarm, on the other hand, is recognized for its vessel-like design, and the first unit has been in operation since 2020. It is a 385 m steel construction equipped with a weathervane mooring system. The entire farm comprises six separate cages along the vessel, and the volume of the whole farm is 414000 m^3, with a capacity to host 10000 tons of salmon [4]. The nets in the upper part of the cages are attached to the rigid frame structure. The farm is dimensioned to withstand a significant wave height of up to 10 m.

The development of the above advanced technologies for exposed and offshore farming has been heavily based on established practices in the offshore oil and gas sector, given many similarities between the engineering methods within these industries. While it is feasible to design and manufacture enduring offshore structures as proven by the oil and gas industry, offshore fish farm structures face additional challenges in ensuring the well-being of the fish. Offshore conditions characterized by strong currents and waves, can significantly impact the fish's behaviour, potentially leading to health and welfare concerns. These considerations impose limitations on the design and site selection of offshore farms. Consequently, offshore farms are currently situated in locations that are either partially sheltered or relatively close to land, rather than fully exposed open sea areas.

Offshore fish farm development is still in its early stages. The cost of establishing offshore farms significantly surpasses that of nearshore fish farms. The elevated cost is primarily driven by the necessity for more robust and expensive structures which also have much higher maintenance costs, as they are subjected to accelerated wear and tear from harsh weather conditions. As an example, Ocean Farm 1 faced a deficit of over 100 million NOK in 2022, largely attributed to major maintenance and upgrading costs. As a result of these challenges, the full-scale development of offshore fish farms remains limited to a few countries such as Norway and China. To facilitate industry growth, well-structured financing is thus imperative. The feasibility of offshore fish farming may be achieved by embracing the development of multi-functional and autonomous infrastructure from the oil and offshore industry. Co-locating offshore renewable energy systems with offshore fish farms has the potential benefits of integration and shared services while reducing operational time and costs. Meanwhile, research and development of the technology require more cross-disciplinary collaboration to take care of engineering and biological challenges, as well as social and environmental aspects.

Conflict of Interest

There is no conflict of interest.

References

[1] Chu, Y.I., Wang, C.M., Park, J.C., et al., 2020. Review of cage and containment tank designs for offshore fish farming. Aquaculture. 519, 734928.

[2] Morro, B., Davidson, K., Adams, T.P., et al., 2022. Offshore aquaculture of finfish: Big expectations at sea. Reviews in Aquaculture. 14(2), 791-815.

[3] Jin, J., Su, B., Dou, R., et al., 2021. Numerical modelling of hydrodynamic responses of Ocean Farm 1 in waves and current and validation against model test measurements. Marine Structures. 78, 103017.

[4] Mobron, E., Torgersen, T., Zhu, S., et al., 2022. Design of Havfarm 1. WCFS2020, proceedings of the second world conference on floating solutions, Rotterdam. Springer: Singapore. pp. 99-111.

Sustainable Marine Structures
https://journals.nasspublishing.com/index.php/sms

ARTICLE

Dynamic Assessment of OWT under Coupled Seismic and Sea-wave Motions

Maryam Massah Fard[1*] **Ayfer Erken**[2] **Atilla Ansal**[1]

1. Department of Civil Engineering, Ozyegin University, Istanbul, 34794, Turkey
2. Department of Civil Engineering, Dogus University, Istanbul, 34775, Turkey

ARTICLE INFO

Article history
Received: 3 July 2023
Revised: 30 August 2023
Accepted: 25 September 2023
Published Online: 29 September 2023

Keywords:
Offshore wind turbines
Seismic motion
Sea-wave loads
Pore water pressure generation

ABSTRACT

The effect of soil-monopile-structure interaction is of great importance in the design of offshore wind turbines (OWTs). Although sea waves play the most effective role in the performance of OWTs, the coupled effect of sea-wave loads and seismic motion on the performance of the OWT system in seismic-prone areas is a factor that is less investigated and should not be ignored. In this regard, a 2-D porous model based on Biot's poro-elastic theory is considered to capture the pore water pressure generation in the soil domain surrounding the OWT foundation. The coupled effect of sea waves and seismic motion through a comparative study is considered for the reference OWT system based on the monopile foundation by using the FE program, OpenSees. The results of the analyses are presented in specific locations. Upon the obtained results, the dynamic behavior of the OWT system and the possibility of liquefaction in the soil surrounding the OWT during applied loads are investigated and compared. This comparison is a good representative of the effect of the seismic motion on the performance of the OWT system and the soil medium by considering soil-monopile-structure interaction in seismic-prone areas.

1. Introduction

According to the demand of the world for green energy resources, wind energy is one of the examples that is of great interest in recent years. Wind energy is a secure type of energy and is environmentally friendly. Because of the considerable number of coastal areas in the world and the high speed of the offshore wind, the Offshore Wind Turbine (OWT) compared to the onshore one, is of great interest nowadays. According to the recent agreement by the countries to achieve net-zero emissions over the coming decades, OWT farms will be increasingly employed in seismically active regions. The reasonable performance of these structures both functionally and economically is one of the main concerns in the OWT projects. It needs to be noted that for these giant structures with a design life of 25 years, the design of the foundation which costs about 25-34% cost of the whole project is one of the most

---

*Corresponding Author:
Maryam Massah Fard,
Department of Civil Engineering, Ozyegin University, Istanbul, 34794, Turkey;
Email: m.massahfard@gmail.com

DOI: http://dx.doi.org/10.36956/sms.v5i2.884

costly parts of the whole system [1]. In this regard, the current study concerns the performance of the offshore wind turbine system during environmental loads (cyclic sea-wave and earthquakes) with a focus on the geotechnical part of the system (foundation and the surrounding soil) which has been less investigated. Monopile, which is the most common foundation for OWTs, is considered for the numerical analyses in the present study.

The present design standards and guidelines for OWTs are dependent on *p-y* curves that are defined for offshore pile foundations in the oil and gas industry. Because of larger numbers of load cycles, the larger diameter of monopiles for OWTs, and the possibility of pore water pressure generation in the soil domain, the accuracy of their application for the OWT system is now questionable among researchers. The main aim of the current study is to evaluate the possibility of liquefaction in the soil medium in the vicinity of the monopile in seismic-prone areas by considering soil-pile-structure interaction.

In the present research, the Finite Element (FE) program OpenSees (The Open System for Earthquake Engineering Simulation) is employed for numerical modeling and analysis of the OWT system [2]. The consequences such as stresses, strains, excess pore water pressure ratio, and deformations are evaluated in specified locations of the model.

Among studies in the field of OWT, some studies investigated the structural response of the OWT system (e.g., [3,4]), and only a few concentrated on the geotechnical performance of the system under seismic actions (e.g., [5-7]). Despite the numerous recent studies in the field of OWT, the number of items relevant to the investigation of the liquefaction possibility in the soil surrounding the OWT is very limited [7]. The traditional *p-y* curves method, used for the current design of the OWTs suggested by the guidelines and standards (API and DNV GL), greatly overestimates the initial stiffness for the liquefied soils. This procedure leads to an unconservative estimation of foundation tilting and the dynamic performance of the overall system [8-10]. In 2020, Kazemi Esfeh and Kaynia evaluated the possibility of liquefaction in the soil surrounding the OWT foundation during the combined action of wind and seismic loads. According to the authors, liquefaction is a phenomenon that has not been studied sufficiently for the case of the OWT foundation and the soil domain in the vicinity of the foundation. The OWTs based on monopile and caisson foundations were analyzed in this research. FLAC 3D software was employed and the soil medium was formed by using SANISAND constitutive model through nonlinear dynamic analyses. They resolved that liquefaction incident has considerable effects on the rotation of both monopile and caisson-type foundations [7].

There are no reliable guidelines or codes for the design of OWTs in seismic-prone areas, and the available codes for seismic design are mainly developed for classic structures. It is required to check and approve their practicality to offshore wind turbines [10]. Bhattacharya et al. (2021) explained the main steps and challenges in the seismic design of offshore wind turbines. They mentioned that OWTs are designed for a lifespan of 25 to 30 years. So, major seismic events are less probable but they are high-risk events. Nowadays, most standards use a 475-year return period (corresponding to a 10% probability of exceedance in 50 years) for the seismic design of OWTs. The amount of allowable tilt for OWT structures is one of the significant design factors of monopile-supported OWTs. The allowable tilt is specified as 0.5 to 0.75 degrees currently, and the effect of the P-delta moment initiates a rise in the foundation loads by the increase in tilt values. They noted that in sites with loose cohesionless soil deposits (e.g., sand), the occurrence of liquefaction is the most critical condition for the seismic design of a monopile foundation. The liquefaction phenomenon may lead to an excessive permanent tilting of the foundation [10]. Zheng et al. (2015) investigated that the joint effect of earthquake and sea-wave loads is essential to be considered for the structural response of OWT through experimental tests. They mentioned that further numerical FE analysis is required to investigate the effect of seismic and hydrodynamic loads on OWT by considering soil-structure interaction [11].

2. Numerical Modeling

2.1 Soil Medium Modeling

The constitutive model (Drucker-Prager $J2$ multi-surface plasticity model) is generally useful for representing the soil behavior for various cyclic loads [12-16]. This model is mostly determined to simulate cyclic liquefaction response in clean sand and silt numerically. Yang et al. (2003) and Elgamal et al. (2003) developed a multi-surface plasticity model at the University of California, San Diego (UCSD) for both sand and clay [16,17]. This model presents an elastic-plastic material and is implemented as Pressure Depend Multi Yield (PDMY) and Pressure Independ Multi Yield (PIMY) for both sand and clay, respectively, in the OpenSees framework [2]. Later PDMY material was modified by Yang et al. (2008) and defined as PDMY02 soil constitutive model in the OpenSees materials library [17]. After clarification of the model, laboratory and centrifuge test results were considered for calibration of soil parameters specified for the current model, and reasonable outcomes were achieved.

The plastic strain tensors (Q and P) in the specified soil constitutive model contain deviatoric and volumetric components and are presented in equation (1) [12].

$$Q = \acute{Q} + Q''\delta,\ P = \acute{P} + P''\delta \tag{1}$$

$\acute{Q}$ and $\acute{P}$ are deviatoric and Q'' and P'' are volumetric components of the plastic strain. Deviatoric plastic strain is defined based on the associative flow rule ($\acute{P} = \acute{Q}$) and $\acute{P}$ can be expressed as $\acute{Q}$ which is specified based on the yield surface. The volumetric plastic strain follows the non-associative flow rule ($P'' \neq Q''$) and P'' can be defined based on the phase transformation (PT) surface instead of the yield surface [18]. In liquefaction studies, non-associativity is of great importance. Contractive, and dilative behaviors of soil can be simulated based on this factor properly [2,16,19].

Contractive and dilative parameters are defined within the soil constitutive model and are inputted to the program as the terms c_1, c_2, c_3 (contraction) and d_1, d_2, and d_3 (dilation), respectively.

Table 1 presents the calibrated soil parameters for undrained sandy soil used in the current study [20]. For modeling the soil domain, the implemented 9-4 quad-up element (9 nodes for solid deformation and 4 corner nodes for pore water pressure determination) in the OpenSees platform is employed.

2.2 OWT System Modeling

Figure 1 presents the schematic view of the monopile-supported OWT. The still sea-water depth is 20 m, the modeled soil depth is 30 m, and the tower's length above the sea level is 90 m. The mass of the rotor and nacelle is assumed as a lumped mass for the FE model [21,22]. Table 2 gives the properties of the OWT, foundation, and sea-water depth for the reference OWT (5-MW NREL).

After the foundation and superstructure are installed

Table 1. PDMY02 calibrated soil properties for Nevada sand (D_r = 63%).

Parameter	Description	Value	Units
G_r, K_r	Reference shear and bulk modulus	72.5E3, 193.6E3	[kPa]
ρ	Saturated unit weight	2	[ton/m^3]
e	Void ratio	0.66	-
φ	Soil friction angle	34.5	[°]
$φ_{PT}$	Soil phase transformation angle	26.5	[°]
P_r	Reference effective confinement pressure	101	[kPa]
n	Pressure dependent coefficient	0.5	-
Υ_{max}	Peak shear strain	0.1	-
c_1, c_2, c_3	Contraction parameters	0.04, 2.5, 0.2	-
d_1, d_2, d_3	Dilation parameters	0.07, 3, 0	-
NYS	No. of yield surfaces generated by model	20	-
liq_1, liq_2	Account for permanent shear strain (slip strain or cyclic mobility) in sloping ground	1, 0	[kPa]

Source: Karimi, Z., Dashti, S., 2016 [20].

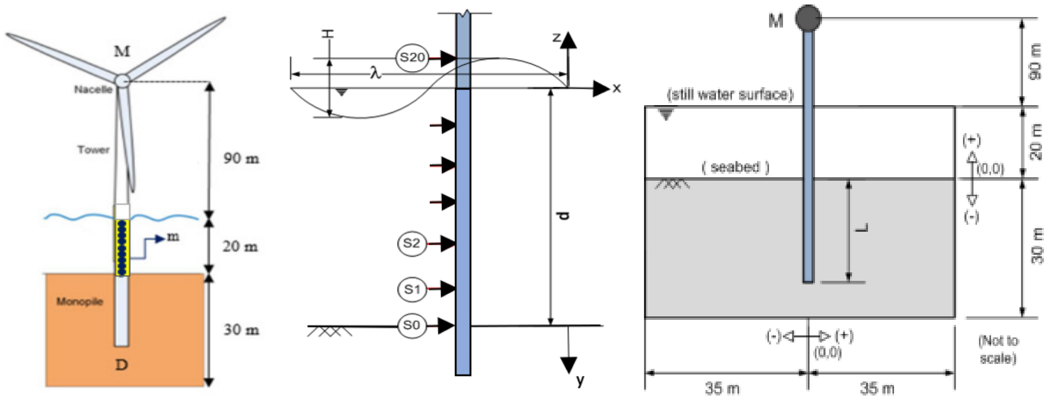

(a) (b) (c)

Figure 1. (**a**) Schematic outlook for the reference OWT, (**b**) wave force application, and (**c**) numerical modeling of the problem for FE analysis.

Source: Fard, M.M., Erken, A., Erkmen, B., et al [22].

Table 2. Offshore wind turbine parameters.

h (m)	**d (m)**	**L (m)**	**D (m)**	**ρs (ton/m^3)**
Tower's length above S.W.L	Water depth	MP embedment depth	MP diameter	Steel density
90	20	20	5	7.85
Es (GPa)	**Asec (m^2)**	**Isec (m^4)**	**IM (ton.m^2)**	**M (ton)**
Steel modulus of elasticity	MP cross-section area	MP moment of inertia	Rotational inertia	Mass of rotor+ nacelle
200	0.777	2.38	2600	350

Note: Figure 1 illustrates the parameters in Table 2 and MP is monopile.

Source: Corciulo, et al.; Fard, et al. [21,22].

in the FE domain, the effect of the soil-pile interaction is captured by utilizing modified soil elements as the interface [22]. The wall thickness (t) is considered constant along the foundation and is considered as 1% of the monopile diameter [21]. The viscous boundary conditions for the base and lateral boundaries are defined by using the Lysmer-Kuhlemeyer dashpots (1969) [22,23]. They are used to damp out outgoing waves by reproducing radiation damping and are defined through zero-length elements in the OpenSees platform [2].

2.3 Load Characteristics

The sea-wave loads are estimated using linear wave theory (small-amplitude wave or Airy theory) and calculated based on the determination of the water particle velocity and acceleration using DNVGL [9,24] according to Morison's equation as given in Equation (2) and are applied to the tower of the OWT. For this purpose, the tower elevation between the seabed and the maximum water level was divided into twenty equal-length strips as shown in Figure 1b. The hydrodynamic force acting on each strip was calculated using Morison's theory.

$$f(t) = \rho(1 + C_A)A\dot{v} + \frac{1}{2}\rho C_D D v|v| \quad (2)$$

where ρ is the mass density of the fluid, C_A is the added mass coefficient (C_A = C_M (inertia coefficient)-1) and C_D is the drag coefficient which is dependent on the Keulegan-Carpenter number and tower diameter calculated based on equations [9], A is the cross-sectional area, $\dot{v}$ is fluid particle acceleration, v is fluid particle velocity, and diameter of the cross-section is defined as D [22]. Based on the equations, C_A and C_D are considered as 0.6 and 1.0, respectively. The variations of surface elevation are considered based on linear wave theory [24].

The distributed sea-wave loads calculated for a 9-sec period and 20-m water depth, are applied to the OWT. The pile diameter and embedment depth are considered 5 m and 20 m respectively. The load applied to the seabed station as a sample for 5-m diameter tower is presented in Figure 2. For detailed information regarding the calculation of sea-wave load through Morison's theory [9,22,24] can be referred.

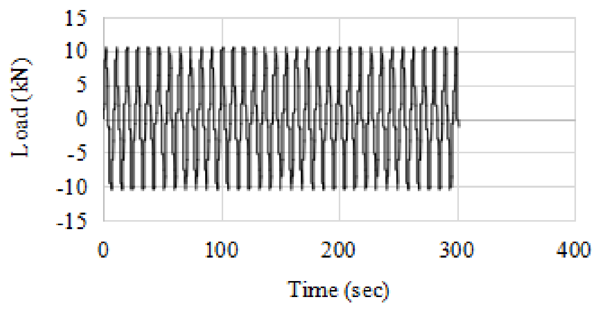

Figure 2. Sea-wave load at y = 0 (seabed (S0)).

Firstly, the sea-wave load is applied for 270 seconds (30 cycles) to the reference OWT system. After this step, the specified seismic motion, Kobe earthquake 1995, with 6.9 M_w (PGA = 0.28 g, PGV = 0.55 m/s, PGD = 0.15 m) is applied to the FE model (at the base of the model) while still, the sea-wave load remains in the system. The time history for the acceleration of the record is presented in Figure 3 (https://peer.berkeley.edu/peer-strong-ground-motion-databases) [25].

3. Finite Element Analysis and Results

In reality, the seismic acceleration and lateral loads of the OWT due to waves will be coupled together to affect the motion and pore water pressure of the soil around the monopile foundation. In the present study, for simplicity, the lateral loads from waves are simplified as a cyclic point force acting on the tower of the OWT [26]. In the present study, the sea-wave cyclic load is obtained based on the common approach used for offshore structures through Morison's theory, linear wave theory (small-amplitude wave or Airy theory) [9,24].

Dynamic excitation is applied as a displacement time history to the base of the soil domain, at the nodes which share equal degrees of freedom with the Lysmer-Kuhlemeyer (1969) dashpots by using the method of Joyner and Chen (1975) [27]. The displacement time history of the recorded ground motion by using the multi-excitation method defined in the program is applied to the system [2].

After applying the sea-wave and seismic loads and FE analysis of the system, the results for the deformation of the monopile foundation and the surrounding soil are obtained in specified locations. Later, the performance of the system during the sea-wave load and the coupled sea-wave and the seismic loads are compared and presented in graphs. In the first case, only the sea-wave load is applied to the OWT system for 302 seconds, and in the second case, the sea-wave load is exerted on the system for 270 seconds (30 cycles) (the time that the steady state situation is reached), and then the sea-wave and seismic loads are applied for 32 seconds (total 302 seconds load application). The variation in the effective vertical stress in the soil medium is a significant sign of excess pore water pressure generation, which can cause liquefaction in the soil domain.

Pile lateral displacement and rotation at the seabed surface are presented in Figure 4. The results for pile deformation develop by reaching the seabed surface, and the highest rates are achieved at the seabed surface. The monopile deformation is more affected during the sea-wave load application, and seismic motion causes a reduction in the deformation values. The values are smaller than the limits defined in DNVGL-ST-0437 [9], and the results obtained for seabed are presented.

Soil effective vertical stress and shear strain are good representatives for the evaluation of pore water pressure generation and liquefaction possibility in the soil domain. Increasing soil shear strain and decreasing effective vertical stress (to reach zero), lead to the increase in excess pore water pressure which makes liquefaction possible ($r_u = 1.0$). Figures 5 and 6 illustrate the soil response in time as, soil shear strain, effective vertical stress, and excess pore water pressure ratio. The response is presented at two specific locations around the pile foundation. The results are evaluated with a 5 m distance from the pile location to avoid interface effects on the outcomes.

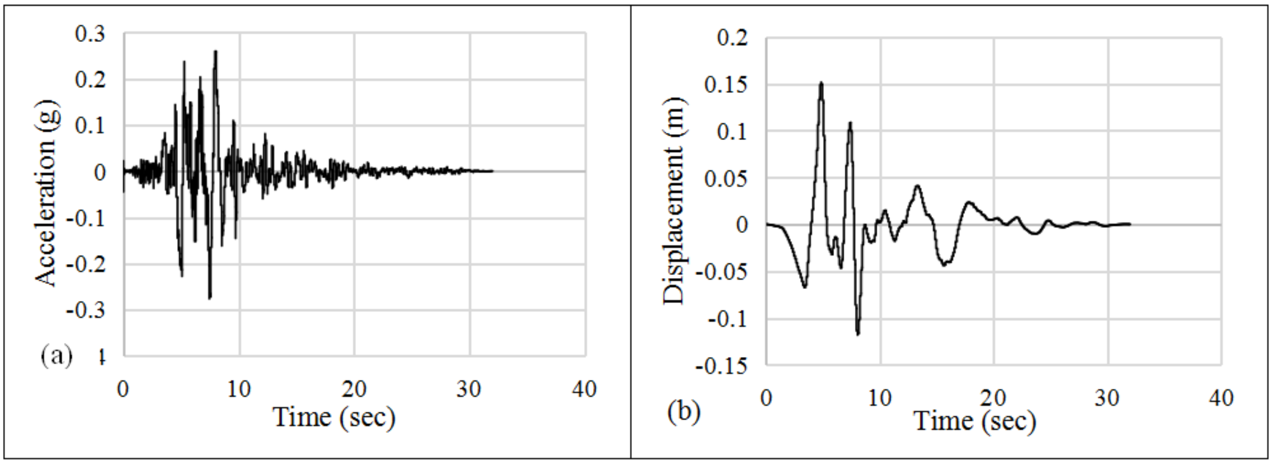

Figure 3. (**a**) Acceleration, and (**b**) displacement time histories of the recorded motion.

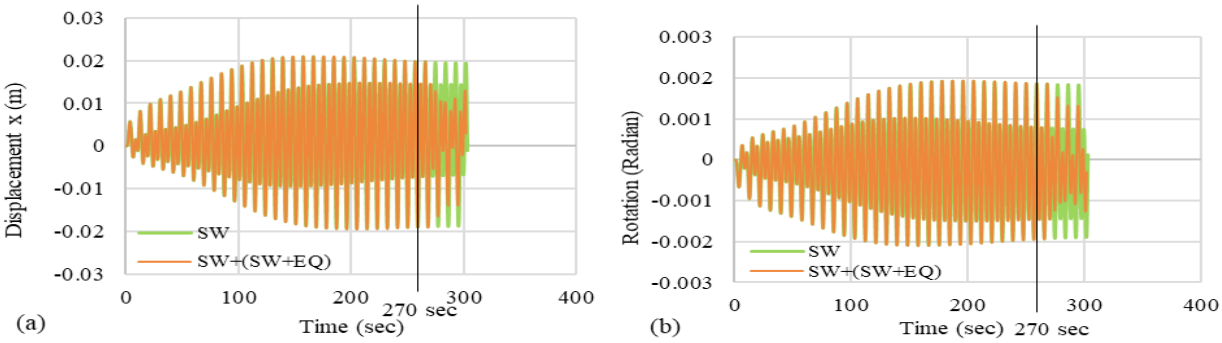

Figure 4. Response at the seabed: (**a**) pile lateral displacement, and (**b**) pile rotation.

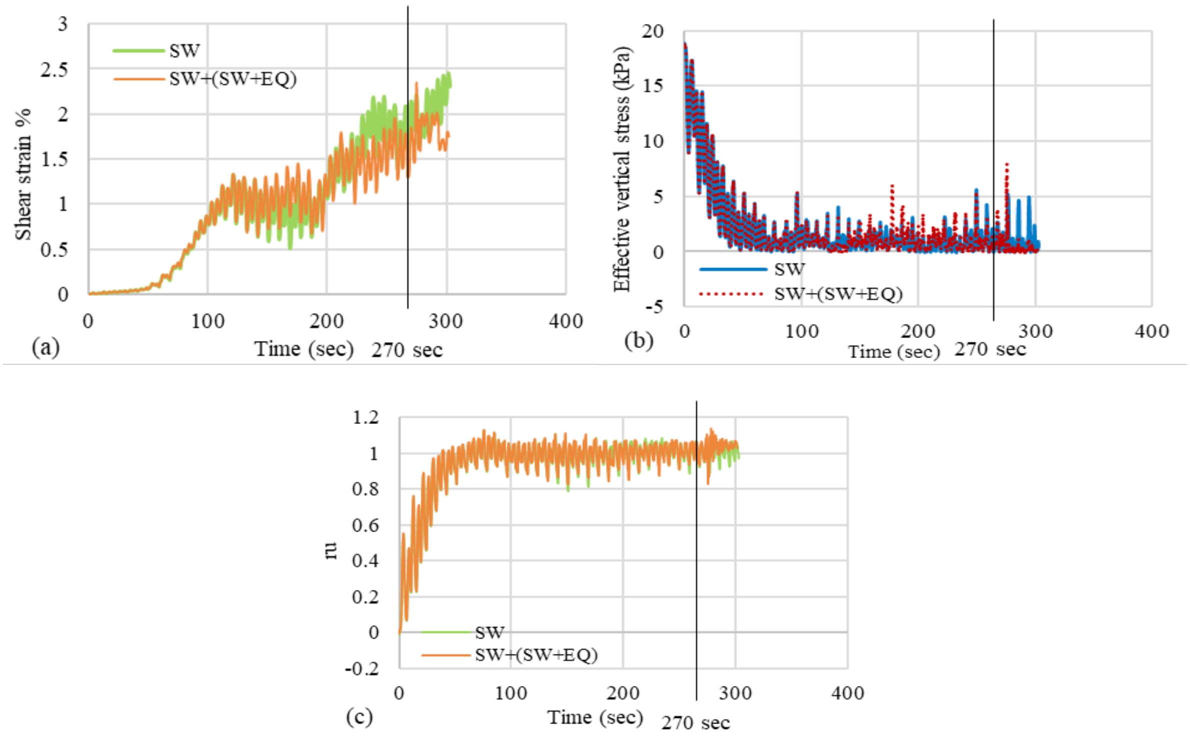

Figure 5. At y = –2 m, and x = +5 m, (**a**) soil shear strain, (**b**) soil effective vertical stress, and (**c**) soil excess pore water pressure ratio.

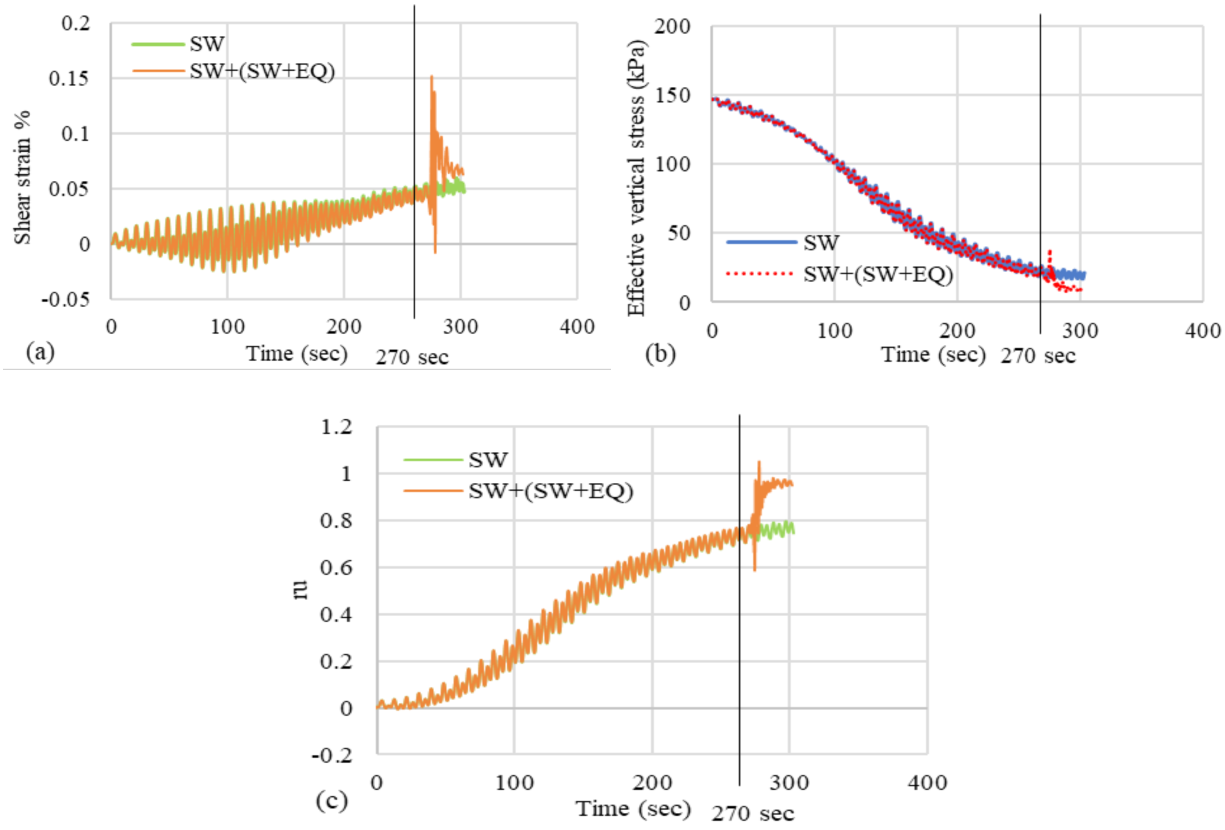

Figure 6. At y = –15 m, and x = +5 m, (**a**) soil shear strain, (**b**) soil effective vertical stress, and (**c**) soil excess pore water pressure ratio.

4. Discussion

Investigating the results during the sole effect of sea-wave and the simultaneous effect of seismic and sea-wave loads shows that the response of the system goes on smoothly during the sea-wave load application while the seismic motion has a sudden effect on the response of the OWT system. The effect of seismic motion is mainly obvious on the soil shear strain values and they increase significantly during the application of seismic motion. By increasing depth from the seabed, the time required for effective vertical stress to reach zero increases, and this delays liquefaction. At 15 m below the seabed surface, the increase in soil shear strain over time is more obvious specifically during seismic motion application to the system. There is a sudden increase in the excess pore water pressure ratio and it reaches 1.0. This shows the effect of seismic motion on possible liquefaction for deeper parts of the seabed surface. Based on the presented graphs, at –2 m below the seabed surface, in the first 40 seconds of sea-wave load application, the effective vertical stress reaches zero, which makes the excess pore water pressure ratio proceed to 1.0, and soil liquefies. The duration required for liquefaction increases to 270 seconds while the depth increases to –15 m from the seabed surface. However, the maximum rate for the excess pore water pressure ratio is 0.75 during individual sea-wave load application to the OWT system.

By comparing the results for the response of soil and monopile, it is apparent that the seismic motion is more effective on the behavior of the soil surrounding the monopile. This results in a rise in the soil response and makes deeper locations of the soil medium liquefy.

5. Conclusions

In this research, the performance of OWT is studied through the 2D fully coupled *u-p* dynamic analysis by considering soil-monopile-structure interaction. In this regard, the effects of the coupled application of sea-wave and seismic loads on the performance of the monopile and the soil surrounding the foundation are investigated. The results are obtained in some specified locations based on the earlier analyses for this research and presented in the selected figures. In this analysis, the sea-wave load is applied for 270 seconds (30 cycles, to reach a steady state) to the OWT system based on a 5-m diameter monopile with 20 m embedment depth. Later the specified earthquake motion is exerted on the system while still, the sea-wave load remains in the system.

In reality, the combination of seismic motion and cyclic sea-wave load is not rational and the load combination performed in the current study is for simplification, and a closer to reality load combination is advised. According to the presented figures, the effective vertical stress approaches zero at about –15 m from the seabed surface. This behavior confirms the loss of strength in the soil medium, which is a primary sign of the appearance of liquefaction. The rise in the soil shear strain values and the drop in the rates for the effective vertical stress during the coupled effect of the sea-wave and seismic motion makes an increase in the excess pore water pressure ratio. This response makes the excess pore water pressure ratio approaches 1.0 over time, and liquefaction happens as a result. By comparing the results obtained through the sole effect of the sea-wave load and the coupled application of sea-wave and seismic loads to the system, it is derived that the seismic motion is more effective on the response of the soil surrounding the monopile. Applying seismic motion to the OWT system leads to the possibility of liquefaction for deeper locations of the soil medium where liquefaction is not the case during the sole effect of sea-wave loads. This is an ongoing study and the obtained results confirm the significant role of the seismic motion on the dynamic response of the soil surrounding the OWT. When it comes to sandy soil and seismic regions, liquefaction is an aspect that plays a significant role. It may cause excessive tilt and permanent rotation which affects the serviceability and stability of the OWTs and this effect should not be ignored in the design of OWTs in seismic-prone areas.

Author Contributions

Conceptualization, M.M.F., A.E., A.A., Methodology, M.M.F., A.E., A.A., Software and Analysis, M.M.F., Investigation, M.M.F., Validation, M.M.F., A.E., A.A., Writing-original draft preparation, M.M.F., Writing Review and Editing, A.A., A.E., M.M.F.

Conflict of Interest

The authors declare no conflicts of interest.

References

[1] Bhattacharya, S., Nikitas, G., Jalbi, S., 2018. On the use of scaled model tests for analysis and design of offshore wind turbines. In: Krishna, A., Dey, A., Sreedeep, S. (eds) Geotechnics for natural and engineered sustainable technologies. Developments in Geotechnical Engineering. Singapore: Springer. pp. 107-129.

[2] Mazzoni, S., McKenna, F., Fenves, G.L., 2010. OpenSees [Internet]. Available from: http://opensees.

berkeley.edu/wiki/index.php/Main_Page

[3] Sadowski, A.J., Camara, A., Málaga-Chuquitaype, C., et al., 2017. Seismic analysis of a tall metal wind turbine support tower with realistic geometric imperfections. Earthquake Engineering & Structural Dynamics. 46(2), 201-219.

[4] De Risi, R., Bhattacharya, S., Goda, K., 2018. Seismic performance assessment of monopile-supported offshore wind turbines using unscaled natural earthquake records. Soil Dynamics and Earthquake Engineering. 109, 154-172.

[5] Yang, C.B., Wang, R., Zhang, J.M. (editors), 2018. Seismic analysis of monopile supported offshore wind turbine. International Conference on Geotechnical and Earthquake Engineering; 2018 Oct 20-21; Chongqing, China.

[6] Mistry, H.K., Lombardi, D., 2020. Role of SSI on seismic performance of nuclear reactors: A case study for a UK nuclear site. Nuclear Engineering and Design. 364, 110691.

[7] Esfeh, P.K., Kaynia, A.M., 2020. Earthquake response of monopiles and caissons for Offshore Wind Turbines founded in liquefiable soil. Soil Dynamics and Earthquake Engineering. 136, 106213.

[8] Recommended Practice for Planning, Designing and Constructing Fixed Offshore Platforms—Working Stress Design [Internet]. API-American Petroleum Institute; 2003. Available from: https://www.academia.edu/37079635/Recommended_Practice_for_Planning_Designing_and_Constructing_Fixed_Offshore_Platforms_Working_Stress_Design_API_RECOMMENDED_PRACTICE_2A_WSD_RP_2A_WSD_TWENTY_FIRST_EDITION_DECEMBER_2000

[9] DNVGL-ST-0437 Loads and Site Conditions for Wind Turbines [Internet]. DET NORSKE VERITAS. Available from: https://www.dnv.com/energy/standards-guidelines/dnv-st-0437-loads-and-site-conditions-for-wind-turbines.html

[10] Bhattacharya, S., De Risi, R., Lombardi, D., et al., 2021. On the seismic analysis and design of offshore wind turbines. Soil Dynamics and Earthquake Engineering. 145, 106692.

[11] Zheng, X.Y., Li, H., Rong, W., et al., 2015. Joint earthquake and wave action on the monopile wind turbine foundation: An experimental study. Marine Structures. 44, 125-141.

[12] Prevost, J.H., 1985. A simple plasticity theory for frictional cohesionless soils. International Journal of Soil Dynamics and Earthquake Engineering. 4(1), 9-17.

[13] Lacy, S., 1986. Numerical procedures for nonlinear transient analysis of two-phase soil system [Ph.D. thesis]. Princeton: Princeton University.

[14] Cubrinovski, M., Ishihara, K., 1998. State concept and modified elastoplasticity for sand modelling. Soils and Foundations. 38(4), 213-225.

[15] Elgamal, A., Yang, Z., Parra, E., et al., 2003. Modeling of cyclic mobility in saturated cohesionless soils. International Journal of Plasticity. 19(6), 883-905.

[16] Yang, Z., Elgamal, A., Parra, E., 2003. Computational model for cyclic mobility and associated shear deformation. Journal of Geotechnical and Geoenvironmental Engineering. 129(12), 1119-1127.

[17] Yang, Z., Lu, J., Elgamal, A., 2008. OpenSees Soil Models and Solid-Fluid Fully Coupled Elements [Internet]. Available from: http://www.soilquake.net/opensees/OSManual_UCSD_soil_models_2008.pdf

[18] Ishihara, K., Tatsuoka, F., Yasuda, S., 1975. Undrained deformation and liquefaction of sand under cyclic stresses. Soils and Foundations. 15(1), 29-44.

[19] Khosravifar, A., 2012. Analysis and design for inelastic structural response of extended pile shaft foundations in laterally spreading ground during earthquakes [Ph.D. thesis]. Davis: University of California.

[20] Karimi, Z., Dashti, S., 2016. Numerical and centrifuge modeling of seismic soil-foundation-structure interaction on liquefiable ground. Journal of Geotechnical and Geoenvironmental Engineering. 142(1), 04015061.

[21] Corciulo, S., Zanoli, O., Pisanò, F., 2017. Transient response of offshore wind turbines on monopiles in sand: Role of cyclic hydro-mechanical soil behaviour. Computers and Geotechnics. 83, 221-238.

[22] Fard, M.M., Erken, A., Erkmen, B., et al., 2022. Analysis of offshore wind turbine by considering soil-pile-structure interaction: Effects of foundation and sea-wave properties. Journal of Earthquake Engineering. 26(14), 7222-7244.
DOI: https://doi.org/10.1080/13632469.2021.1961936

[23] Lysmer, J., Kuhlemeyer, R.L., 1969. Finite dynamic model for infinite media. Journal of the Engineering

Mechanics Division. 95(4), 859-877.

[24] DNVGL-OS-J101 Design of Offshore Wind Turbine Structures [Internet]. DET NORSKE VERITAS. Available from: https://docplayer.net/21082564-Design-of-offshore-wind-turbine-structures.html

[25] PEER Strong Ground Motion Databases [Internet] [cited 2021 Jun 23]. Available from: https://peer.berkeley.edu/peer-strong-ground-motion-databases

[26] Geng, F., Yang, W., Nadimi, S., et al., 2023. Study for predicting the earthquake-induced liquefaction around the monopile foundation of offshore wind turbines. Ocean Engineering. 268, 113421.

[27] Joyner, W.B., Chen, A.T., 1975. Calculation of nonlinear ground response in earthquakes. Bulletin of the Seismological Society of America. 65(5), 1315-1336.

NASS
NAN YANG ACADEMY OF SCIENCES

Sustainable Marine Structures
https://journals.nasspublishing.com/index.php/sms

ARTICLE

Numerical Simulations of the Pitching Airfoil by Using Discrete Vortex Method

Peng Ren[1,2] **Ke Lin**[1,2] **Jiasong Wang**[1,2,3*]

1. Department of Engineering Mechanics, School of Naval Architecture, Ocean and Civil Engineering, Shanghai Jiao Tong University, Shanghai, 200030, China
2. Key laboratory of Hydrodynamics (Ministry of Education), Shanghai Jiao Tong University, Shanghai, 200030, China
3. SJTU-Sanya Yazhou Bay Institute of Deepsea Science and Technology, Sanya, Hainan, 572024, China

ARTICLE INFO

Article history
Received: 5 September 2023
Revised: 15 October 2023
Accepted: 25 October 2023
Published Online: 31 October 2023

Keywords:
Discrete vortex method
Pitching motion
Airfoil
Thrust

ABSTRACT

This paper presents a two-dimensional discrete vortex method that uses the vortex growing core model to simulate the unsteady force and the wake patterns of the pure pitching airfoil efficiently and accurately. To avoid the random fluctuation caused by the random walk method, a vortex growing core method is used to simulate the viscous diffusion motion. In addition, the vortices fall off randomly on the body surface. Referring to the experimental configurations of Mackowski and Williamson (2015), a good agreement is achieved through the comparisons between the present simulation results and the experimental results, including the mean force coefficients, oscillation amplitude and wake patterns. It shows that the two-dimensional discrete vortex method can be used to predict the mechanical behavior and wake patterns on the pitching airfoil motion.

1. Introduction

Birds, as well as some marine creatures, use vibrations of their wings, fins or other parts to generate thrust and lift. From the perspective of bionics, some scholars have focused on creating thrust-generating devices, just like autonomous underwater vehicles and some flapping wing micro-aerial vehicles [1-3]. This kind of device is different from the turbines which rotate around an external axis to achieve electricity generation [4-6], but to control the

---

*Corresponding Author:
Jiasong Wang,
Department of Engineering Mechanics, School of Naval Architecture, Ocean and Civil Engineering, Shanghai Jiao Tong University, Shanghai, 200030, China; Key laboratory of Hydrodynamics (Ministry of Education), Shanghai Jiao Tong University, Shanghai, 200030, China; SJTU-Sanya Yazhou Bay Institute of Deepsea Science and Technology, Sanya, Hainan, 572024, China;
Email: jswang@sjtu.edu.cn

DOI: http://dx.doi.org/10.36956/sms.v5i2.944

airfoil motion actively for realizing the bionic behavior such as propulsion, hovering, heaving and so on. In recent decades, more and more scholars focused on the thrust and lift generation mechanism of flapping wings and how this mechanism is influenced by various factors. The pure pitching motion of the airfoil simplifies the complex motion of the flapping airfoil, and the study by considering only the pitching motion is instructive for researchers to understand the evolution law of unsteady forces during the movement of the airfoil.

On the basis of Theodore's pioneer study [7] on the unsteady force of oscillating airfoil, Garrick [8] theoretically calculated the unsteady force caused by the pitching and heaving motion of the airfoil. The results showed that the pitching motion need high enough frequency to make the transition from drag to thrust, whereas the heaving motion could produce thrust at any frequency. Koochesfahani [9] visualized the wake structure of the pitching NACA 0012 and found that the wake structure can be modified by the control of the amplitude, frequency and shape of the vibration waveform. Further, Bohl and Koochesfahani [10] improved the experiment and introduced the method of estimating the mean force on the airfoil by using the measured mean and fluctuating velocity fields. Godoy-Diana et al. [11] captured the transition of the vortex streets in the wake flow of pitching airfoil from the Benard-von Karman (Bvk) wake to the reverse Bvk vortex street. The results also showed that this transition precedes the actual drag-thrust transition. Schnipper et al. [12] visualized a variety of wakes in a vertical soap film and mapped out the wake types in a phase diagram.

Similarly, some scholars used numerical simulation to discover the mystery of the pitching airfoil. Young and Lai [13] used a compressible two-dimensional Navier-Stokes solver to study the flow over a NACA 0012 airfoil which oscillated sinusoidally in the plunge. Chandravanshi et al. [14] used both a gridless Lagrange technique and a finite volume based Navier-Stokes solver to study the pure plunging motion of the airfoil. Wu et al. [15] studied the NACA 66 hydrofoil's pitching motion under the Lagrange coherent structures. In this study, he used the $k-\omega$ shear stress transport turbulence model coupled with a two-equation $\gamma - Re_\theta$ transition model for the turbulence closure was used. As a meshless numerical simulation method of Lagrange, the discrete vortex method has higher efficiency than the traditional CFD method. Therefore, some scholars also use the discrete vortex method to calculate the unsteady force and the wake structure of the pitching airfoil [16-19]. However, most of them used the method of random walk which was introduced by Chorin [20] to model the viscous diffusion and this method may cause the random fluctuation of order $Re^{-1/2}$ to the simulation result. To avoid this random fluctuation, some scholars used the growing core method [21-23] instead of the random walk method which was introduced by Park [24] in 1989. Also, some scholars specified the control layer thickness in advance according to the results of a trial and error procedure when using the discrete vortex method.

This study introduces a two-dimensional discrete vortex method to simulate the propulsive performance of the pitching airfoil. This method uses the vortex growing core method to simulate the viscous diffusion motion, instead of the random walk method. In addition, the vortices fall off randomly in this study instead of setting a fixed boundary layer thickness in advance. In order to validate the reliability of this method, the pure pitching motion of the airfoil referring to the experiment of Mackowski and Williamson [25] is simulated. For verifying the calculated results, the mean force coefficients, oscillation amplitude and wake patterns are compared.

In this paper, Section 1 introduces the background of the pitching airfoil and the research status of other scholars; Section 2 introduces the numerical implementation method for calculating the pitching airfoil; Section 3 shows the comparison between the simulation results and the experimental results; Section 4 draws a conclusion.

2. Numerical Method

2.1 Governing Equation

With the assumption of mass-force ignored, for the two-dimensional, incompressible, viscous flow, the fluid continuity equation and the Navier Stokes equation can be written as:

$$\nabla \cdot \boldsymbol{V} = 0 \tag{1}$$

$$\frac{\partial \boldsymbol{V}}{\partial t} + \boldsymbol{V} \cdot \nabla \boldsymbol{V} = -\frac{1}{\rho}\nabla p + v\nabla^2 \boldsymbol{V} \tag{2}$$

where $\boldsymbol{V}$ is the local velocity vector of the fluid, p is the pressure, ρ and v are the uniform density and the kinematic viscosity, respectively. Taken the curl of the velocity on both sides of N-S equation, it can be written as:

$$\frac{\partial \omega}{\partial t} + \boldsymbol{V} \cdot \nabla \omega = v\nabla^2 \omega \tag{3}$$

where ω is the vorticity, $\omega = \nabla \times \boldsymbol{V}$. Considering the two-dimensional fluid, the continuity equation can be rewritten by introducing the stream function φ in the form of Poisson equation:

$$\omega = -\nabla^2 \varphi \tag{4}$$

To solve the equation, Chorin [20] introduced the operator splitting method which divided the equation into two parts: the convection part and the viscous diffusion part.

$$\frac{\partial \omega}{\partial t} = -\boldsymbol{V} \cdot \nabla \omega \tag{5}$$

$$\frac{\partial \omega}{\partial t} = \nu \nabla^2 \omega \tag{6}$$

The convection equation indicates the invariance of the vorticity of the vortex elements when the vorticity field is discretized. For solving the convection equation, the Biot-Savart law can be used to obtain the summation speed of the vortex elements which concludes the velocity induced by the other vortices in the vorticity field and the incoming flow.

$$\boldsymbol{V}(\boldsymbol{r},t) = \boldsymbol{U}_\infty - \frac{1}{2\pi} \int \frac{(\boldsymbol{r}-\boldsymbol{r}_i) \times \omega(\boldsymbol{r}_i,t)}{(\boldsymbol{r}-\boldsymbol{r}_i)^2} dV \tag{7}$$

where $\boldsymbol{U}_\infty$ is the free stream incoming flow, $\boldsymbol{r}_i = (x_i, y_i)$ is the position vector of the i-th vortex element, $\omega(\boldsymbol{r}_i, t)$ is the vorticity of the i-th vortex element at $\boldsymbol{r}_i$. Since the solution of the equation exists singularity which will cause the calculated speed become infinite near the vortex element position, Chorin [20] introduced a vortex core model 'vortex-blob' which gave the vortex elements finite core radius to make the function bounded. Using this vortex core model, the equation can be rewritten discretely as [20]:

$$\boldsymbol{V}(\boldsymbol{r},t) = \boldsymbol{U}_\infty - \frac{1}{2\pi} \sum_{i=1}^{N} \Gamma_i \frac{(\boldsymbol{r}-\boldsymbol{r}_i)}{(\boldsymbol{r}-\boldsymbol{r}_i)^2 + \sigma_i^2} \tag{8}$$

where σ_i is the radius of the i-th vortex blob, Γ_i is the circulation of i-th vortex blob.

2.2 Numerical Implement of Pitching Airfoil

The stream function of the velocity induced by the i-th vortex element can be written as:

$$\varphi_i = -\frac{\Gamma_i}{4\pi} \ln(\boldsymbol{r}_i^2 + \sigma_i^2) \tag{9}$$

In the vorticity field, the total stream function of the j-th element can be written as:

$$\varphi_j = \boldsymbol{U}_\infty y_j - \sum_{i=1}^{N_s} \frac{\Gamma_i}{4\pi} \ln((\boldsymbol{r}_j-\boldsymbol{r}_i)^2 + \sigma_i^2) - \sum_{k=1}^{N_w} \frac{\Gamma_k}{4\pi} \ln((\boldsymbol{r}_j-\boldsymbol{r}_k)^2 + \sigma_k^2) \tag{10}$$

where N_s and N_w are the number of vortex elements generated in the surface and the vortex elements moving into the wake flow, respectively.

It should be noted that the no-slip condition and no-penetration condition should be satisfied near the solid body surface, which can be written as:

$$\begin{cases} \boldsymbol{u} \cdot \boldsymbol{s} = \boldsymbol{u}_b \cdot \boldsymbol{s} \\ \boldsymbol{u} \cdot \boldsymbol{n} = \boldsymbol{u}_b \cdot \boldsymbol{n} \end{cases} \tag{11}$$

where $\boldsymbol{s}$ and $\boldsymbol{n}$ are the tangent and normal vector of the solid body surface, respectively, $\boldsymbol{u}$ and $\boldsymbol{u}_b$ are the velocity of fluid near the solid body surface and the velocity of the body, respectively. Results from Qian and Vezza [26], Clarke and Tutty [27] and Wang and Yeung [28] have shown that no-slip condition and no-penetration condition are equivalent to determine the vorticity boundary condition. Therefore, satisfying either no-slip condition or no-penetration condition can uniquely determine the vorticity distribution.

As mentioned before, by solving the equation that satisfies the no-penetration condition, the vorticity distribution can be obtained on the solid body surface. This equation is calculated by differentiating the stream function of two adjacent control points on the surface, as written below.

$$\varphi_{i+1} - \varphi_i = \boldsymbol{U}_{ci} \cdot \boldsymbol{n} \Delta S_i \tag{12}$$

where φ_i is the stream function of the i-th control point on the surface, $\boldsymbol{U}_{ci}$ is the solid body surface velocity at the i-th control point, ΔS_i is the distance between i-th and $(i+1)$-th control points. As shown in Figure 1, N_s vortex elements are generated corresponding to N_s control points on the airfoil surface at each time step. For each two adjacent vortex elements, the corresponding equation to solve the vorticity of every newly generated vortex element. The form of the linear equations listed can be written as:

$$\boldsymbol{A}\Gamma = \boldsymbol{B} \tag{13}$$

where $\boldsymbol{A}$ is a $N_s \times N_s$ coefficient matrix, Γ is the vector composed of the vorticity of new vortexes, $\boldsymbol{B}$ is a vector. The elements of matrix $\boldsymbol{A}$ and vector $\boldsymbol{B}$ can be written as:

$$a_{ki} = \frac{1}{4\pi} \ln \frac{\left[(\boldsymbol{r}_{k+1}-\boldsymbol{r}_i)^2 + \sigma_{i^2}\right]}{\left[(\boldsymbol{r}_k-\boldsymbol{r}_i)^2 + \sigma_{i^2}\right]} \tag{14}$$

$$b_k = (\boldsymbol{U}_\infty - \boldsymbol{U}_{ck})(\boldsymbol{r}_{k+1} - \boldsymbol{r}_k) - \frac{1}{4\pi} \sum_{i=1}^{N_w} \Gamma_i \ln \frac{\left[(\boldsymbol{r}_{k+1}-\boldsymbol{r}_i)^2 + \sigma_{i^2}\right]}{\left[(\boldsymbol{r}_k-\boldsymbol{r}_i)^2 + \sigma_{i^2}\right]} \tag{15}$$

To ensure the conservation of the total vorticity in the field, the vorticity of the new elements and the vortex elements in the wake flow should satisfy the condition of the equation.

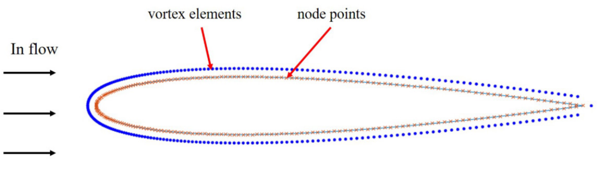

Figure 1. Scheme of the airfoil body surface and corresponding vortex elements.

$$\sum_{i=1}^{N_s} \Gamma_i = -\sum_{j=1}^{N_w} \Gamma_j \tag{16}$$

The vorticity of the newly generated vortex elements can be solved. Under the circumstance of N_s unknowns and $N_s + 1$ equations, Walther [29] used the least square method and the Gauss elimination algorithm to solve this equation set. So far, the vorticity of newly generated vortex elements can be obtained by solving the convection equation, and the induced velocity between elements can be further calculated to update the whole field.

In addition, the solution of the viscous diffusion equation is the Green function. Usually, scholars use the random walk method which was introduced by Chorin to simulate the viscous diffusion motion. In order to avoid the random fluctuation caused by this method, Park [24] introduced a vortex growing core method, in which the growing radius of the vortex can be written as:

$$\sigma^{n+1} = \sqrt{\left(\sigma^{n}\right)^{2} + 4.946 v \Delta t} \tag{17}$$

where σ^n and σ^{n+1} are the core radius at the n-th time step and the $(n+1)$-th step, respectively, Δt is the length of time step. Since then, both the convection part and the viscous diffusion part can be calculated, so that the whole vorticity field can be calculated by updating the vortex motion information.

Since at each time step, certain number of vortex elements are generated on the body surface, a total number of vortex elements will increase rapidly and then make the computational cost increase dramatically. Spalart [30] introduced a vortex element emergence method to control the total number of vortex elements in the whole field. At each time step, if two vortex elements satisfy the condition of the equation, merge these two vortex elements [30].

$$\frac{\left|\Gamma_i \Gamma_j\right|}{\left|\Gamma_i + \Gamma_j\right|} \cdot \frac{\left|\boldsymbol{r}_i - \boldsymbol{r}_j\right|^2}{(D_0 + d_i)^{3/2} (D_0 + d_j)^{3/2}} \le V_0 \tag{18}$$

where r_i and r_j are the position information of the i-th and the j-th vortex element, respectively, D_0 and V_0 are the governing parameters, d_i and d_j are the distance from the i-th and the j-th vortex element to the body surface, respectively. The vortex element information after the emergence is written as:

$$\boldsymbol{r} = \frac{\boldsymbol{r}_i \Gamma_i + \boldsymbol{r}_j \Gamma_j}{\Gamma_i + \Gamma_j} \tag{19}$$

$$\Gamma = \Gamma_i + \Gamma_j \tag{20}$$

2.3 Solution of Pitching Airfoil in Water Environment

This study uses the two-dimensional discrete vortex method introduced above to simulate the flow field and the mechanical behavior of the airfoil when the airfoil performs a pure pitch motion. The motion pattern of the airfoil shown in Figure 2 is considered, in which the airfoil oscillates around its quarter-chord point with the frequency f and the angle θ_0. The free stream flow direction is from the left to the right. At each time step, the angle of attack is controlled by a sinusoidal oscillation shown in the equation. Also, this study uses the reduced pitching frequency k which is nondimensionalized by the freestream velocity $\boldsymbol{U}_\infty$, the chord length c and the frequency f. The equation can be written as:

$$\theta = \theta_0 \sin(2\pi f t) \tag{21}$$

$$k = \frac{\pi f c}{U_\infty} \tag{22}$$

Another parameter charactering the pitching motion of the airfoil is the Strouhal number St_A. It can be defined based on the wake width A. In nature, swimmers and birds typically keep the St_A between 0.2 and 0.4 [31]. Due to the fact that the wake width A is difficult to measure, it can be replaced by the amplitude change of the airfoil's trailing edge [25].

$$St_A = \frac{fA}{U_\infty} = \frac{f \cdot 2c \cdot r_p \cdot \sin\theta_0}{U_\infty} \tag{23}$$

where r_p is the dimensionless length from the pivot point to the trailing edge (in this study, $r_p = 0.75$). Similarly, the Reynolds number which combines the free stream velocity, kinematic viscosity and the chord length is also one of the dominant parameters in the research of pitching airfoils. The Reynolds number can be defined as:

$$\mathrm{Re} = \frac{U_\infty \cdot c}{\upsilon} \tag{24}$$

In this study, the time step Δt is determined by a non-dimensional time step dt based on the free stream incoming flow velocity U_∞ and the chord length c, which can be seen in:

$$\Delta t = \frac{dt \cdot c}{U_\infty} \tag{25}$$

In this study, dt is set as 0.01 after some trial and error.

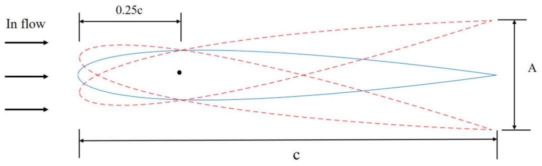

Figure 2. Geometry and kinematics of the airfoil.

The force exerted on the airfoil can be determined by the pressure distribution on the body surface. The tangential pressure gradient on the body surface can be written as [16]:

$$\frac{1}{\rho}\frac{\partial p}{\partial \boldsymbol{s}} = -\boldsymbol{s}\cdot a_c - \boldsymbol{n}\cdot\boldsymbol{r}\cdot\frac{d\omega}{dt} + \boldsymbol{s}\cdot\boldsymbol{r}\cdot\omega^2 + v\frac{\partial\Gamma}{\partial \boldsymbol{n}} \tag{26}$$

where ***s*** and ***n*** are the tangential and normal unit vector at the considering control point, respectively, ***r*** is the vector which starts from the pivot point to the considering control point, ω is the angular velocity at this control point t, p and a_c are the pressure and the acceleration on the selected control point, respectively. The first three terms of the right side in the equation represent the motion acceleration, rotational acceleration and centripetal acceleration, respectively.

By integrating circumferentially the body surface pressure, the streamwise force and the transverse force can be obtained. The form of thrust and lift coefficient can be written as equation (27) and equation (28), where the thrust coefficient C_T describes the propulsion performance of the pitching airfoil.

$$C_T = \frac{F_x}{\frac{1}{2}\rho U_\infty{}^2 c} \tag{27}$$

$$C_Y = \frac{F_y}{\frac{1}{2}\rho U_\infty{}^2 c} \tag{28}$$

3. Results and Discussion

For validating the computational accuracy of the two-dimensional discrete vortex method introduced above, this study carried out the numerical simulation of the pitching airfoil referring to the experimental configuration of Mackowski and Williamson [25]. The main parameters of the pitching airfoil are listed in Table 1. In Mackowski and Williamson's research, they studied the trends in propulsive performance with the flapping frequency, pitching angle and Reynolds number for NACA 0012. They also examined the unsteady forces on the pure pitching airfoil.

Table 1. Main parameters of the airfoil in the configuration of Mackowski and Williamson.

Airfoil Type	NACA 0012 Hydrofoil
Chord length	10 cm
Pivot location	0.25c
Reynolds number	12000, 16600
Pitching angle	2°, 4°, 8°, 16°, 32°
Reduced frequency range	0.5-12

Figure 3 shows the experimental and computational time average values of thrust coefficient C_T under the circumstance of $Re = 12000$, $\theta_0 = 2°$, with the range of reduced pitching frequency k from 0.5 to 12. When the frequency is small, the value of the thrust coefficient is about –0.03, which is close to the static drag for the airfoil at zero angle of attack [32]. The thrust coefficient monotonically increases with the increase of the frequency k, and the transition from drag ($C_T < 0$) to thrust ($C_T > 0$) occurs at $k = 10$. At $k = 12$, C_T reaches the maximum of 0.02. Comparing the black points of the experimental results with the red points of the numerical results, it can be observed that the numerical results agree reasonably well with the experimental results in the whole range. In this case, the average thrust coefficient C_T and its variation trend can be calculated well.

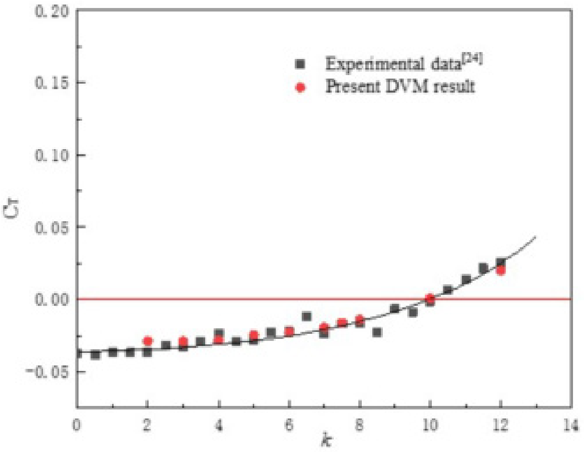

Figure 3. Experimental and computational values of thrust coefficient for the pitching NACA 0012 airfoil when Re = 12000, $\theta_0 = 2°$.

As can be seen in Figure 3, both experimental and simulation results show that the crossover point between thrust and drag occurs at the position of $k = 10$ under the condition of $Re = 12000$, $\theta_0 = 2°$. Further, Figure 4 indicates the crossover value of the reduced frequency k in the Reynolds number range from 1×10^4 to 3×10^4. Although there is a slight gap between the experimental and calculated values with the Reynolds number increasing, the overall trend shows great consistency. The crossover point decreases monotonically with the increase of the Reynolds number, which means that the higher Reynolds number makes it easier to generate thrust due to the airfoil pitching motion.

Figure 5 shows the variation trend between the mean thrust coefficient C_T and Strouhal number St_A at different pitching angles under the condition of Re = 16600. The black line is a curve fitted to the data. It can be observed that the mean thrust coefficient C_T and the Strouhal number St_A show a monotonically consistent increase when the pitching angle $\theta_0 \leq 8°$. However, this trend changes dramatically at the pitching angle of $\theta_0 = 16°$ and $\theta_0 = 32°$. It can be observed that within the increasing frequency in large-amplitude cases, the thrust coefficients present a decreasing trend instead of an increasing trend. Therefore, it is necessary to avoid the excessive pitching angle in the design of the pitching airfoil propulsion procedure.

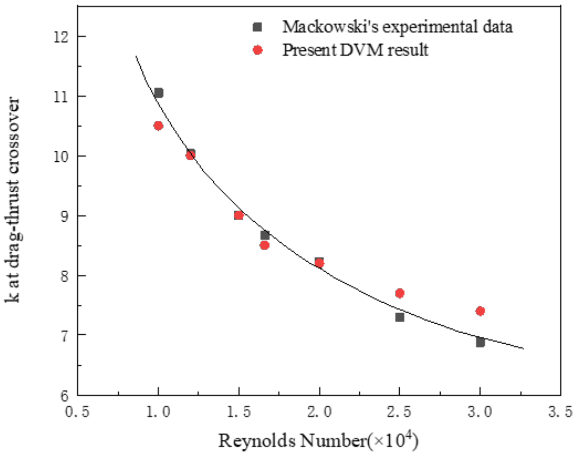

Figure 4. The crossover point of reduced frequency *k* at $\theta_0 = 2°$.

Under the condition of small pitching angles, the simulation can well predict the thrust coefficient results and its trend. However, as the angle increases, the simulation results of C_T present some gap compared with the experimental result. What's gratifying is that the simulation result can still predict the variation trend in the range of large angle amplitudes.

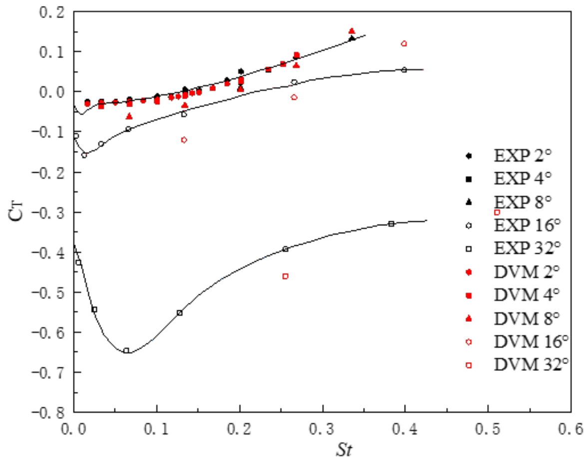

Figure 5. Mean thrust coefficient vs. Strouhal number St_A at different pitching angles when *Re* = 16600.

Figure 6 and Figure 7 present the oscillating amplitude of the unsteady thrust and lift coefficient in Mackowski and Williamson's experiment and the simulation of this paper at different pitching angles. It can be observed that the increase of the pitching angle and the frequency will lead to the increase of force coefficient, and this trend will be enhanced with the increase of pitching angles. Figure 6(b) and Figure 7(b) show the C_T/θ_0^2 and C_T/θ_0 amplitude, respectively. The scaling in C_T and C_Y work remarkably well across the whole range of pitching angles. The black lines shown are the prediction results of the linear theory introduced by Garrick [8]. It can be seen that across the whole range of pitching angles, the numerical calculation can well predict the value and variation trend of C_T and C_Y under different conditions. The oscillating amplitude of C_T/θ_0^2 andC_Y/θ_0 under all pitching angles can both be fitted into a curve, and the numerical calculation results can also reflect this feature.

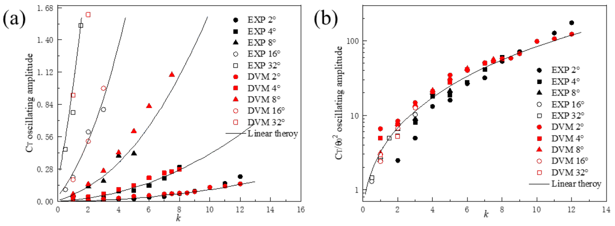

Figure 6. Amplitude of the varying component of the thrust coefficient at different pitching angles when *Re* = 16600: (**a**) C_T oscillating amplitude vs. reduced frequency *k*; (**b**) $C_T$oscillating amplitude divided by θ_0^2 vs. reduced frequency *k*.

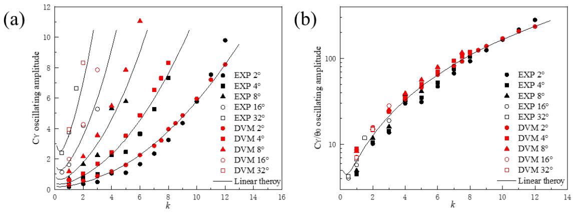

Figure 7. Amplitude of the varying component of the lift coefficient at different pitching angles when *Re* = 16600: (**a**) C_Y oscillating amplitude vs. reduced frequency *k*; (**b**) C_Y oscillating amplitude divided by θ_0 vs. reduced frequency *k*.

Figure 8 shows the spanwise vorticity results presented by Mackowski and Williamson's PIV measurements and the simulation result of this paper under the same conditions. It shows that no matter *k* = 2, *k* = 5 or *k* = 9, the simulation results present the consistent vorticity structure characteristics in the wake flow. As the reduced frequency *k* increases, the wake flow vortex mode changes from 4P + 2S to 2P and then to inverse-2S mode. Similar results can also be observed in Godoy-Diana et al. and Schnipper et al.'s research [11,12]. Figure 8 proves that the numerical calculation method introduced in this paper can not only predict the fluid force exerted on the body, but also can be used to obtain the wake structure of the pitching airfoil.

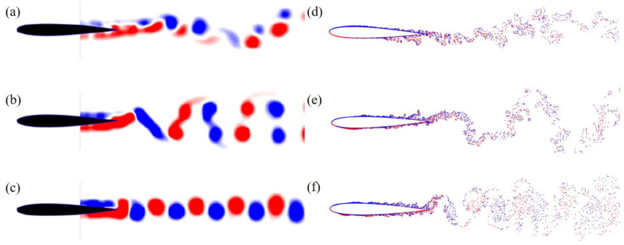

Figure 8. Spanwise vorticity presented by PIV measurements and DVM simulation with pitching angle $\theta_0 = 2°$, $Re = 16600$: (**a**) PIV measurement when $k = 2$; (**b**) PIV measurement when $k = 5$; (**c**) PIV measurement when $k = 9$; (**d**) simulation result when $k = 2$; (**e**) simulation result when $k = 5$; (**f**) simulation result when $k = 9$.

4. Conclusions

This study introduces a two-dimensional discrete vortex method to simulate the propulsive performance of the pitching airfoil. The vortices fall off randomly on the body surface instead of setting a fixed boundary layer thickness in advance. In addition, the vortex growing core method is used to simulate the viscous diffusion motion instead of the random walk method. By using this method, the pure pitching motion of the airfoil under the same configurations as Mackowski and Williamson's [25] experiment is simulated in order to verify the reliability of this method. The mechanical behavior and wake patterns with different flapping frequencies, amplitudes and Reynolds numbers are obtained and studied.

Under the condition of $Re = 12000$, $\theta_0 = 2°$, the mean value of the thrust coefficient C_T can be predicted well by the present numerical simulations. Within the increase of reduced frequency k, the x direction force acting on the airfoil will monotonically increase and complete the transition from drag to thrust. Similarly, the results of reduced frequency k when the transitions from drag to thrust occur under different Reynolds numbers also agree well with the experimental results. It can be observed that the crossover point which indicates the transitions from drag to thrust decreases monotonically with the increase of Reynolds number, indicating that it is easier to generate thrust for airfoils at higher Reynolds numbers. In the cases of different pitching angles, thrust results for small angle cases collapse reasonably well with Strouhal number. With larger pitching angles, there are some slight differences between the calculated lift coefficients and the experimental results, but it can still predict the amplitude and the variation trend of the force coefficient. Compared with PIV measurements, the simulation wake patterns visualized by the distribution of vortex elements present the consistent vorticity structure characteristics. It can be clearly observed that the transitions from the '4P + 2S' mode to the '2P' mode and eventually to the inverse '2S' mode occur gradually as the pitching frequency increases.

This study proves that the two-dimensional discrete vortex method introduced in this paper can be used to reasonably predict the propulsion performance and wake patterns on the pitching airfoil motion. As this paper mainly focuses on the validation of this method used in the pure pitching airfoil cases, further research can be also carried out to study the complex airfoil motion such as the heaving and pitching combined motion, based on the method introduced in this paper.

Author Contributions

Peng Ren: Conceptualization, Methodology, Validation, Investigation, Writing - Original Draft. Ke Lin: Investigation, Methodology, Writing-Review and Editing. Jiasong Wang: Conceptualization, Methodology, Resources, Writing-Review & Editing, Supervision, Funding acquisition.

Funding

This research was funded by Innovative Research Foundation of Ship General Performance #31422225.

Acknowledgement

The authors acknowledge the fund support from Innovative Research Foundation of Ship General Performance #31422225.

Data Availability

The data that support the findings of this study are available upon reasonable request.

Conflict of Interest

All authors disclosed no any conflict of interest.

References

[1] Jones, K.D., Bradshaw, C.J., Papadopoulos, J., et al., 2005. Bio-inspired design of flapping-wing micro air vehicles. The Aeronautical Journal. 109(1098), 385-393.

[2] Jones, K., Duggan, S., Platzer, M. (editors), 2001. Flapping-wing propulsion for a micro air vehicle. 39th Aerospace Sciences Meeting and Exhibit; 2001 Jan 8-11; Reno. p. 126.

[3] Read, D.A., Hover, F.S., Triantafyllou, M.S., 2003. Forces on oscillating foils for propulsion and maneuvering. Journal of Fluids and Structures. 17(1), 163-183.

[4] Cheng, Q., Liu, X., Ji, H.S., et al., 2017. Aerodynamic analysis of a helical vertical axis wind turbine. Energies. 10(4), 575.

[5] Lewthwaite, M.T., Amaechi, C.V., 2022. Numerical investigation of winglet aerodynamics and dimple effect of NACA 0017 airfoil for a freight aircraft. Inventions. 7(1), 31.

[6] Nguyen, M.T., Balduzzi, F., Goude, A., 2021. Effect of pitch angle on power and hydrodynamics of a vertical axis turbine. Ocean Engineering. 238, 109335.

[7] Von Karman, T., 1935. General aerodynamic theory-perfect fluids. Aerodynamic Theory. 2, 346-349.

[8] Garrick, I.E., 1936. Propulsion of a Flapping and Oscillating Airfoil [Internet]. Available from: https://ntrs.nasa.gov/api/citations/19930091642/downloads/19930091642.pdf

[9] Koochesfahani, M.M., 1989. Vortical patterns in the wake of an oscillating airfoil. AIAA Journal. 27(9), 1200-1205.

[10] Bohl, D.G., Koochesfahani, M.M., 2009. MTV measurements of the vortical field in the wake of an airfoil oscillating at high reduced frequency. Journal of Fluid Mechanics. 620, 63-88.

[11] Godoy-Diana, R., Aider, J.L., Wesfreid, J.E., 2008. Transitions in the wake of a flapping foil. Physical Review E. 77(1), 016308.

[12] Schnipper, T., Andersen, A., Bohr, T., 2009. Vortex wakes of a flapping foil. Journal of Fluid Mechanics. 633, 411-423.

[13] Young, J., Lai, J.C., 2004. Oscillation frequency and amplitude effects on the wake of a plunging airfoil. AIAA Journal. 42(10), 2042-2052.

[14] Chandravanshi, L.K., Chajjed, S., Sarkar, S. (editors), 2010. Study of wake pattern behind an oscillating airfoil. Proceeding of the 37th National & 4th International Conference on Fluid Mechanics and Fluid Power; 2010 Dec 16-18; Chennai. p. 16-18.

[15] Wu, Q., Huang, B., Wang, G., 2016. Lagrangian-based investigation of the transient flow structures around a pitching hydrofoil. Acta Mechanica Sinica. 32, 64-74.

[16] Lin, H., Vezza, M., Galbraith, R.M., 1997. Discrete vortex method for simulating unsteady flow. AIAA Journal. 35(3), 494-499.

[17] Sarkar, S., Venkatraman, K., 2006. Numerical simulation of thrust generating flow past a pitching airfoil. Computers & Fluids. 35(1), 16-42.

[18] Andersen, A., Bohr, T., Schnipper, T., et al., 2017. Wake structure and thrust generation of a flapping foil in two-dimensional flow. Journal of Fluid Mechanics. 812, R4.

[19] Priovolos, A.K., Filippas, E.S., Belibassakis, K.A., 2018. A vortex-based method for improved flexible flapping-foil thruster performance. Engineering Analysis with Boundary Elements. 95, 69-84.

[20] Chorin, A.J., 1973. Numerical study of slightly viscous flow. Journal of Fluid Mechanics. 57(4), 785-796.

[21] Yamamoto, C.T., Meneghini, J.R., Saltara, F., et al., 2004. Numerical simulations of vortex-induced vibration on flexible cylinders. Journal of Fluids and Structures. 19(4), 467-489.

[22] Meneghini, J.R., Saltara, F., de Andrade Fregonesi, R., et al., 2004. Numerical simulations of VIV on long flexible cylinders immersed in complex flow fields. European Journal of Mechanics-B/Fluids. 23(1), 51-63.

[23] Lin, K., Wang, J., 2019. Numerical simulation of vortex-induced vibration of long flexible risers using a SDVM-FEM coupled method. Ocean Engineering. 172, 468-486.

[24] Park, W.C., 1989. Computation of flow past single and multiple bluff bodies by a vortex tracking method [Ph.D. thesis]. Minneapolis: University of Minnesota.

[25] Mackowski, A.W., Williamson, C.H.K., 2015. Direct measurement of thrust and efficiency of an airfoil undergoing pure pitching. Journal of Fluid Mechanics. 765, 524-543.

[26] Qian, L., Vezza, M., 2001. A vorticity-based method for incompressible unsteady viscous flows. Journal of Computational Physics. 172(2), 515-542.

[27] Clarke, N.R., Tutty, O.R., 1994. Construction and validation of a discrete vortex method for the two-dimensional incompressible Navier-Stokes equations. Computers & Fluids. 23(6), 751-783.

[28] Wang, L., Yeung, R.W., 2016. Investigation of full and partial ground effects on a flapping foil hovering above a finite-sized platform. Physics of Fluids. 28(7).

[29] Walther, J.H., 1994. Discrete vortex method for two-dimensional flow past bodies of arbitrary shape undergoing prescribed rotary and translational motion. Den Polytekniske Læreanstalt: Lyngby.

[30] Spalart, P.R., 1983. Numerical simulation of separated flows. Stanford University: Stanford.

[31] Taylor, G.K., Nudds, R.L., Thomas, A.L., 2003. Flying and swimming animals cruise at a Strouhal number tuned for high power efficiency. Nature. 425(6959), 707-711.

[32] Laitone, E.V., 1997. Wind tunnel tests of wings at Reynolds numbers below 70 000. Experiments in Fluids. 23(5), 405-409.

NASS
NAN YANG ACADEMY OF SCIENCES

Tel.:+65 62233839
E-mail:contact@nassg.org
Add.:12 Eu Tong Sen Street #07-169 Singapore 059819

2661-3158
02